SMART NANOCOMPOSITES

Volume 7, Number 1, 2016

TABLE OF CONTENTS

Short Communications

nova publishers
New York

Smart Nanocomposites

This Journal presents new studies in the fast growing area of smart materials, in particular, composite nanostructured materials. It focuses on the physics and physical chemistry of surfaces, interfaces, thin films and coatings, nanoparticles and other nanostructures, as well as on their new and smart applications. Original approaches in fabrication and applications of nanostructured materials will get special attention. Nanostructured ceramics, alloys, various nanocarbon forms (nanotubes, fullerenes, graphene) and their composites used in sensors (including single molecule sensing) and actuators, artificial metabolism, drug delivery, selective membranes, fuel cells, energy storage, and photovoltaics are just a few examples of new classes of materials and applications that are within the scope of the Journal. It features the results of interdisciplinary research from universities, national labs, and privately owned companies.

The Journal is peer-reviewed with the highest standards and quality of publications. The purpose of this Journal is to bring the most up-to-date advances in nanotechnology together, and to give research groups the opportunity to compare their results with other groups' data. To achieve this, the Journal focuses mostly on practical applications of nanodevices, and on proof of the concept publications. Areas of interest include (but not are limited to): sensors, smart membranes, smart coatings for corrosion protection, aspects of significance to nanorobots: power supplies, nanorobot manipulating devices, and microchips for artificial intelligence. The Journal also deals with safety issues: safety of nanotechnology to the environment, controlling the nanodevices, and other aspects.

Smart Nanocomposites
is published in two issues per year by

Nova Science Publishers, Inc.
400 Oser Avenue, Suite 1600
Hauppauge, New York 11788-3619, U.S.A.
E-mail: nova.main@novapublishers.com
Web: www.novapublishers.com

ISSN: 1949-4823

Subscription Rate per Volume
Print: $245 Electronic: $245 Combined Print + Electronic: $367

Additional color graphics might be available in the e-version of this journal.

Smart Nanocomposites
Volume 7, Number 1
ISSN: 1949-4823

MODELING THE BEHAVIOR OF CARBON NANOPARTICLES C_{44} WHEN HEATED IN AN ARGON ATMOSPHERE. COMPUTER EXPERIMENT

Nick M. Barbin[1,2,*], Vasiliy P. Dan[1], Dmitriy I. Terentiev , and Sergey G. Alekseev[1]

[1]The Ural Institute of State Fire Service of Emercom of Russia, Ekaterinburg, Russia
[2]The Ural Agrarian State University, Ekaterinburg, Russia

ABSTRACT

Thermodynamic modeling of the behavior of carbon nanoparticles C_{44} by heating in an argon atmosphere was held, the equilibrium constant for reactions occurring in the system C_{44}-Ar determined. The graphics of the dependences of the compositions of the gas and condensed phases on temperature in the studied system were constructed. Graphics of the dependence of the equilibrium constants of the reactions with increasing temperature were constructed.

Keywords: thermodynamic modeling, the equilibrium constant, carbon nanoparticles, carbon nanotubes, heating

INTRODUCTION

The carbon nanoparticles possess a number of properties, largely depending on their quality, such as conductivity, great tensile strength in combination with high values of elastic deformation, the diamagnetic properties [1]. The presence of these properties is determined by a high strength carbon-carbon bonds, colossal strength packing of atoms, no (negligible or low density) of structural defects [2].

However, thermal properties of carbon nanomaterials are not well understood.

This article studied the behavior of nanocarbon C_{44} heating in an argon atmosphere at a pressure of 10^5 PA. Nanocarbon C_{44} is a molecule, which consists of 44 carbon atoms. The research was carried out by the method of thermodynamic modeling.

* Corresponding autor: Prof. N.M. Barbin, Prof. of Ural Institute of SFSE Russia, Ekaterinburg, Russia, E-mail: nmbarbin@mail.ru.

THE METHOD OF CALCULATION

Thermodynamic modeling is thermodynamic analysis of the equilibrium of system in general (a complete thermodynamic analysis) [3, 4].

One of the most developed and effective programs that implement such thermodynamic calculations, is the complex program TERRA, representing a stage of further development of the software package ASTRA [5].

Thermodynamic modeling has been used successfully in the study of behavior of radioactive graphite by heating in different environmental conditions [6, 7, 8, 9, 10]. We also successfully use thermodynamic modelling in physics and materials science [11, 12]. The calculations of composition of phase and characteristics of the equilibrium are performed using a reference database on properties of chemicals [13, 14].

RESULTS AND DISCUSSION

Computer experiment allows to determine the phase distribution of carbon in the system C_{44}-Ar in all considered temperature range.

The temperature dependence of the composition of the gas phase in the system C_{44}-Ar is presented in Figure 1.

In the temperature range from 2473 K to 4073 K the concentration of C_3 increases sharply and reaches almost $10^{-2,46}$ mole fraction. With further increasing of temperature up 4273 K concentration is reduced to $10^{-2,52}$ mole fraction. In the temperature interval from 2573 K to 4273 K the concentration of the component C increases and reaches $10^{-2,74}$ mole fraction. The concentration of C_2 in a temperature range from 2673 K to 4273 K increases and reaches $10^{-2,94}$ mole fraction. In the temperature interval from 2873 K to 3973 K concentration of component C_5 is rapidly increased to $10^{-3,73}$ mole fraction, if you increase the temperature to 4273 K rapidly decreases up to $10^{-4,06}$ mole fraction. The concentration of component C_4 in the temperature interval from 2973 K to 4073 K increases to $10^{-4,24}$ mole fraction. With increasing of temperature to 4273 K the concentration of the component gradually decreases to $10^{-4,35}$ mole fraction.

The temperature dependence of the condensed phase composition on in the system C_{44}-Ar is presented in Figure 2.

In the temperature range from 473 K to 3973 K we can observe almost linear decrease in the concentration of the component C with $10^{-1,64}$ mole fraction. to $10^{-1,87}$ mole fraction. In the temperature range from 473 K to 3573 K the concentration of the component C_2 increases gradually to $10^{-2,37}$ mole fraction, if you increase the temperature to 3973 K it is linearly decreases to $10^{-2,48}$ mole fraction. In the temperature range from 773 K To 3573 K the concentration of the component C_3 gradually increases up to $10^{-3,00}$ mole fraction. With temperature increasing up to 3773 K the concentration of the component slightly decreases to $10^{-3,06}$ mole fraction, and when the temperature is 3973 K it is $10^{-2,97}$ mole fraction. In the temperature range from 1073 K to 3473 K the concentration of component C_4 gradually increases up to $10^{-3,64}$ mole fraction. With increasing of the temperature from 3473 K to 3973 K the concentration of the component decreases to $10^{-3,80}$ mole fraction. In the temperature range from 1373 K to 3273 K the concentration of C_5 component increases gradually to $10^{-4,38}$ mole fraction. With increasing of the temperature to 3973 K concentration C_5 sharply linearly

increases up to $10^{-3,02}$ mole fraction. In the temperature range from 3373 K to 3573 K a sharp linear increase in the concentration of the component C. Its concentration reaches $10^{-3,42}$ mole fraction. With further increase of temperature up to 3973 K concentration increases less rapidly and reaches $10^{-2,57}$ mole fraction. The concentration of the component C_{84} at a temperature ranging from 3373 K to 3973 K reaches $10^{-3,31}$ mole fraction. The concentration of the component C_{90} at a temperature ranging from 3373 K to 3973 K reaches $10^{-3,47}$ mole fraction. The concentration of the component C_{76} at a temperature ranging from 3373 K to 3973 K reaches $10^{-3,86}$ mole fraction. The concentration of the component C_{70} at a temperature ranging from 3373 K to 3973 K reaches $10^{-4,18}$ mole fraction. In the temperature interval from 3473 K to 3973 K a rapid increase in the concentration of C_{60} component. It is observed reaches $10^{-4,75}$ mole fraction. The concentration of the component C_{56} at a temperature ranging from 3473 K to 3973 K reaches $10^{-4,94}$ mole fraction. The concentration of the component C_{50} in a temperature range from 3473 K to 3973 K reaches $10^{-5,22}$ mole fraction. In the temperature interval from 3473 K to 3973 K the concentration of the component C_{44} reaches $10^{-5,41}$ mole fraction. In the temperature interval from 3473 K to 3973 K the concentration of component C_{32} and C_{28} reaches $10^{-5,62}$ mole fraction.

Descriptions of reactions with distinguishing the temperature intervals are described in graphics, that were discussed earlier (Figure 1-2) to allocate temperature intervals of the reactions. In the system flow physico-chemical processes that can be divided into 4 groups (Table 1).

Table 1. Reactions occurring in the system C_{44}-Ar

No.	The name of the group	Reaction	Temperature range of reaction, K
1	2	3	4
1	Molization reactions occurring in the condensed phase:	$2C_{(s)} = C_{2(s)}$	773 - 3373
		$3C_{(s)} = C_{3(s)}$	1273 - 3373
		$4C_{(s)} = C_{4(s)}$	1973 - 3373
		$3C_{(s)} = C_3$	2673 - 3473
		$76C_{3(s)} = 3C_{76(s)}$	3373 - 3773
		$35C_{2(s)} = C_{70(s)}$	3373 - 3873
		$42C_{2(s)} = C_{84(s)}$	3373 - 3673
		$45C_{2(s)} = C_{90(s)}$	3373 - 3673
2	The thermal dissociation reactions occurring in the condensed phase:	$3C_{94(s)} = 94C_{3(s)}$	3673 - 3973
3	The evaporation reaction of molization:	$5C_{3(s)} = 3C_5$	3373 - 3773
4	The evaporation reaction with thermal dissociation:	$5C_{84(s)} = 84C_5$	3573 - 3773
		$C_{94(s)} = 94C$	3573 - 4273
		$C_{94(s)} = 47C_2$	3373 - 4273

According to these equations, using calculations of concentration (in molar fractions) found in model of components of the condensed and gas phases corresponding equilibrium constants were calculated. For the most important reactions they presented analytical equations:

$$lnK_i = A_i + B_i\,(1/T) \quad (1)$$

Coefficients (A) and (B) reactions calculated by the method of the least squares and are given in Table 2.

Table 2. Coefficients of the constants of reactions

No.	Reaction	ΔT, °K	A	B	R^2
1	2	3	4	5	6
1	$2C_{(s)} = C_{2(s)}$	773 - 3373	-5016,2	-2,2727	0,9983
2	$3C_{(s)} = C_{3(s)}$	1273 - 3373	-10512	-4,4186	0,998
3	$4C_{(s)} = C_{4(s)}$	1973 - 3373	-17081	-6,1806	0,9983
4	$3C_{94(s)} = 94C_{3(s)}$	3673 - 3973	-0,7512	2535,5	0,9384
5	$3C_{(s)} = C_3$	2673 - 3473	-101228	20958	0,9993
6	$5C_{3(s)} = 3C_5$	3373 - 3773	-137111	23,16	0,9823
7	$76C_{3(s)} = 3C_{76(s)}$	3373 - 3773	-7E+06	2180	0,9644
8	$35C_{2(s)} = C_{70(s)}$	3373 - 3873	-3E+06	948,06	0,9769
9	$42C_{2(s)} = C_{84(s)}$	3373 - 3673	-4E+06	1079,3	0,9268
10	$45C_{2(s)} = C_{90(s)}$	3373 - 3673	-4E+06	1154,7	0,9264
11	$5C_{84(s)} = 84C_5$	3573 - 3773	-4E+06	-1324,2	0,9374
12	$C_{94(s)} = 94C$	3573 - 4273	0,5838	-2328,6	0,986
13	$C_{94(s)} = 47C_2$	3373 - 4273	-5E+06	1206,8	0,9762
R – the value of the approximation					

Figure 3-7 show the dependence of the values of the equilibrium constant of the reactions considered above 1/T. For convenience, they were divided into five temperature ranges: the first from 373 to 3373 K; the second from 3673 to 3873 K; the third from 3473 to 3873 K; the fourth from 3473 to 3673 K, the fifth from 3373 to 3973 K (the number of reactions is given in Table.2). The analysis of lines in Figure 3–7 position shows the magnitude and the dependence of the equilibrium constants of reactions on temperature. They presented an analytical equation (1). (A) the factor influencing the position (offset) straight relative to the x-axis. With increasing of this factor, we can see that the line stands higher on the graphic and reaction products produced.

The coefficient (B) indicates the angle between the direct constants of the reaction and the x-axis. The larger this ratio, the stronger the reaction takes place with increasing temperature.

CONCLUSION

Computer modeling of thermodynamic heating carbon nanoparticles C_{44} at atmospheric pressure under inert gas (argon) was conducted. As a result of investigation the processes and temperature ranges reactions were determined. The graphics of the dependences of the compositions of phases on temperature in the studied system are constructed. Constants of reactions and plots of constant values of reaction temperature in the system were calculated.

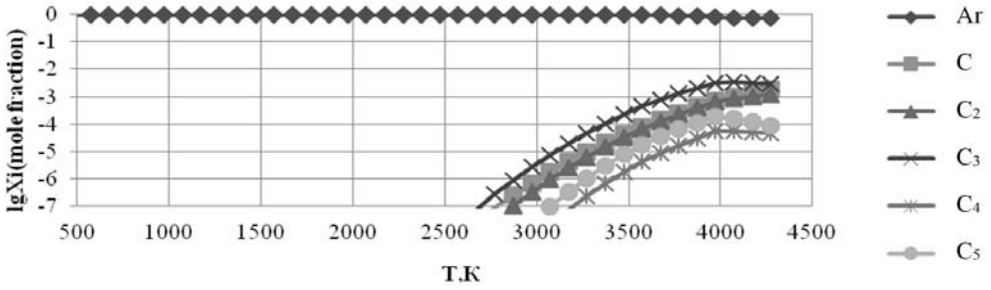

Figure 1. The dependence of the composition of the gas phase temperature in the system C_{44}-Ar at a pressure of 10^5 Pascal.

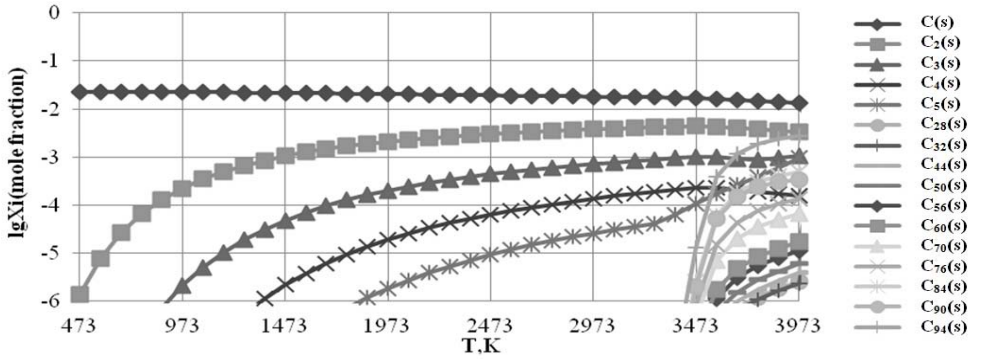

Figure 2. The dependence of the condensed phase composition on temperature in the system C_{44}-Ar at a pressure of 10^5 Pascal.

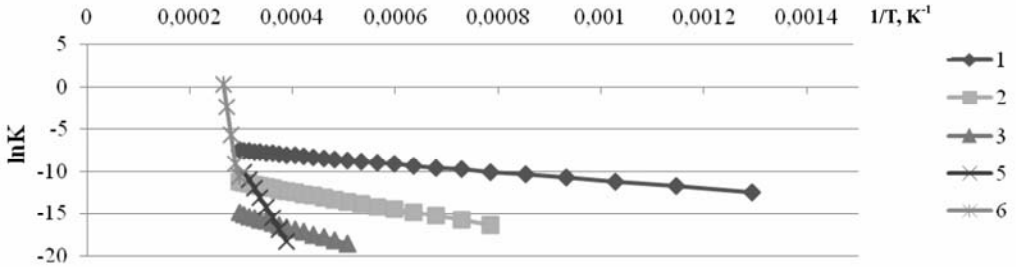

Figure 3. The dependence of the equilibrium constant reactions of 1/T in the temperature interval from 773 to 3373 K.

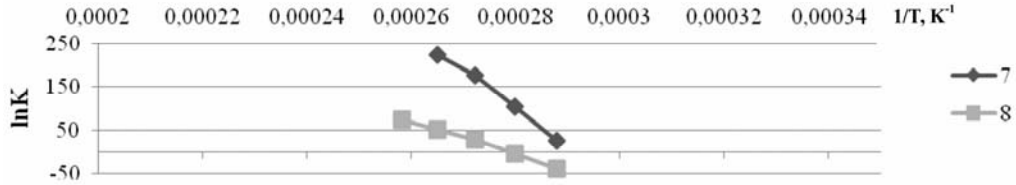

Figure 4. The dependence of the values of the equilibrium constant reactions of 1/T in the temperature interval from 3673 to 3873 K.

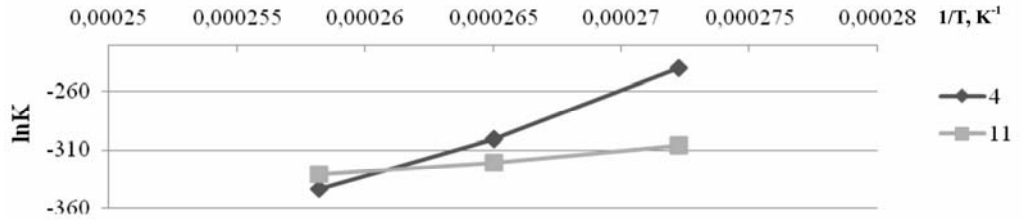

Figure 5. The dependence of the values of the equilibrium constant reactions of 1/T in the temperature interval from 3473 to 3873 K.

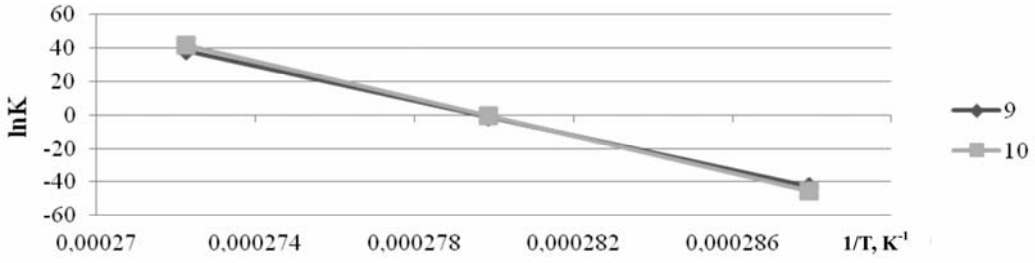

Figure 6. The dependence of the values of the equilibrium constant reactions of 1/T in the temperature interval from 3473 to 3673 K.

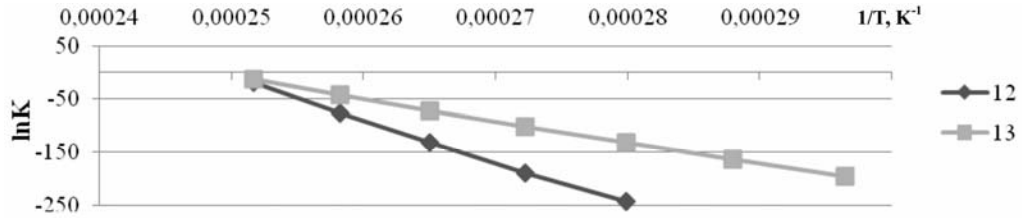

Figure 7. The dependence of the values of the equilibrium constant reactions of 1/T in the temperature interval from 3373 to 39373 K.

REFERENCES

[1] Ubbelode A. R., Lewis F. A. *Graphite and its crystal compounds*/translation from English. E. S. Golovina, O. A. Tsukanova. – M.: Mir, 1965.- 257 p.

[2] Bells S. N. The carbon materials. Properties, technologies, applications: training. POS – Dolgoprudny: Publishing House "Intellect," 2012. - 296 p.

[3] N. M. Barbin, D. I. Terentiev, S. G. Alekseev, Tuktarov M. A., Romenkov A. A. Modeling of radioactive graphite oxidation in molten salts. – Book of abstracts. The 33rd international symposium "Scientific basis for nuclear waste management." – St. Petersburg, 2009, p. 133.

[4] N. M. Barbin, D. I. Terentiev, S. G. Alekseev, Tuktarov M. A., Romenkov A. A. Modeling of radioactive graphite oxidation in molten salts: computer experiment. – *Material research society symposium proceeding*, 2009, 1193, p. 359-366.

[5] Vatolin N. And., Moiseev G. K., Trusov B. G. Thermodynamic modeling in high temperature systems. – M.: *Metallurgy,* 1994.-352 p.

[6] M. Shavaleev, R., Barbin N. M., Dalchow M. P., Terentyev D. I., Alexeev S. G. Thermodynamic modeling of the behavior of americium, caesium and strontium when heated radioactive graphite in nitrogen atmosphere//Technosphere safety: Internet magazine 2014. No. 2 (3). URL: http://www.uigps.ru/content/nauchnyy-zhurnal/.

[7] Barbin N. M. Terentyev D. I., Peshkov A. V., Alexeev S. G. Thermodynamic modeling of radionuclide behavior during heating (burning) of radioactive graphite in air]//*Pozharovzryvobezopasnost'*. 2014. No. 3. From 57 – 65.

[8] Barbin N. M. Kobelev A. M., Terentyev D. I., Alexeev S. G. Thermodynamic modeling of radionuclide behavior during heating (burning) of radioactive graphite in water steam//*Pozharovzryvobezopasnost'*. 2014. No. 10. With 38 – 47.

[9] M. Shavaleev, R., Barbin N. M., Dalchow M. P., Terentyev D. I., Alexeev S. G. thermodynamic Calculation of the properties of radioactive graphite – nitrogen at heating//materials of the XIV Russian conference (with international participation) on thermophysical properties of substances (RTPC-14) T. 2, Kazan: Izd-vo "Fatherland," 2014. P. 206 – 208.

[10] Barbin N. M. Tikina I. V., Terentyev D. I., Alexeev S. G. Thermodynamic modeling of the vapor phase during evaporation of the molten wood's alloy at different pressures// *journal of Applied physics*. 2014. No. 3. From 12 – 16.

[11] Dan V. P., Barbin N. M. Terentyev D. I., Alexeev S. G. Heating nanocarbon particles C at atmospheric pressure in argon. *Technosphere safety*. 2015. No. 1. S. 19-22. URL: http://uigps.ru/content/nauchnyy-zhurnal.

[12] Kolbin T. S., Barbin N. M., LTC D. I., Alekseev S. G. The behavior of Eu, Pu, Am radionuclide at burning radioactive graphite in an oxygen atmosphere. Computer experiment. *EPJ Web of Conferences* 82, 01013 (2015). DOI: 10.1051/ eplconf/20158201013.

[13] Gurevich L. V., Weitz I. V., Medvedev V. A. Thermodynamic properties of individual substances: Ref. ed-e in 4 volumes. – M.: *Nauka,* 1982. -8540 S.

[14] Alemasov V. E., Dregalin A. F., Tishin A. P. *Thermodynamic and thermophysical properties of combustion products: reference book*. In 5 volumes. – M.: VNIITE, 1971. – S. 6350.

Smart Nanocomposites
Volume 7, Number 1
ISSN: 1949-4823

PACK CHROMIZING PROCESS OF STEEL BY MEANS OF IODINE TRANSPORT

S. P. Bogdanov, N. A. Khristyuk*, and M. M. Sychov
St. Petersburg State Technological Institute (Technical University),
Department of Theoretical Foundations of Materials, Russia

ABSTRACT

The paper presents the results of a diffusion chromium plating steel by gas transport iodides. A series of chromium coatings has been done. The regularities of their formation and properties have been investigated. It is shown that iodine can be efficiently transport agent.

Keywords: chrome, diffusion saturation, iodine transport, coating

INTRODUCTION

Chromium coating on steel by diffusion is widely used in modern technology [1-5]. The resulting coatings have excellent corrosion resistance, hardness, wear resistance.

From the literature it is known for a number of substances that can act as a chromium-containing gas phase, from which there is saturation of steel with chromium. There are $CrCl_2$, $CrCl_3$, $CrBr_2$, CrI_2, CrF_2. Gas metallization may be formed by reacting chromium metal activators: NH_4F, NH_4Cl, NH_4Br, NH_4I. Currently, the most widely used method is based on the activation process by using ammonia chloride, NH_4Cl. It is believed that as a source of chromium best results are obtained using, instead of pure chromium ferrochromium [3]. Mixture for chromium plating is 65-70% of chromium powder (or ferrochromium), 25-30% alumina and 0.1-1.5% ammonia chloride. Cementation process is carried out at 950-1150^{0}C [3].

The main requirement for the chemical properties of a gas transport agent is its ability to form gaseous (volatile) compound with the transported metal, which can then be easily decomposed on the steel surface with the release of the parent metal. A convenient and accessible agent satisfied this condition is iodine. Iodine transportation chromium successfully used to produce high purity metal [6]. In [7-9] the iodine used for the production of coatings in a number of inorganic powder materials, however, for diffusion saturation of

* nikolai.hristyuk@mail.ru.

steel has not been used. An advantage of iodine is its high reactivity to a number of metals. Transport of titanium occurs at a temperature 450^0C. It is known that the interaction of metallic chromium with iodine vapors occurs at a temperature 500^0C [6] and leads to the formation of chromium iodide reaction:

$$2Cr + 3I_2 \rightarrow 2CrI_3 \quad (1)$$

Another advantage of the iodine as a transport agent is that the amount of iodine that significantly influences the process is very small. Thus, for an abrupt increase in thickness of the film formed TiC on the graphite at 1000^0C, have sufficient 0.005 wt.% iodine content in a mixture with the Ti [10]. A similar effect was observed in the gas transport of chromium on diamond [7, 8], but the minimum required content of iodine in the reactor was not determined. The aim of this work: to examine the possibility of using iodine as a gas transport agent for diffusion saturation of steel with chromium and assess the quality of the coatings.

EXPERIMENT

As the object of study used carbon steel AISI 1020, the chemical composition is shown in Table 1. Analyses of the chemical elements were carried out by X-ray fluorescence instrument Axios Advanced, the concentration of carbon and sulfur were analyzed on the device Eltra CS - 800.

Table 1. Chemical composition of sample steel

C	Mn	P	S	Cr	Ni	Mo	Si	Cu	N	As
0.18	0.54	0.017	0.015	0.02	0.05	<0.01	0.24	0.04	0.010	0.006

The source of chromium in the chromium metal powder served with a particle size of 3 - 20 microns. It is also used metal iodine mark "h" (pure), alumina qualification "ch.d.a" (pure for analysis particle size of 10-100 microns) and a high purity argon gas. Experiments on diffusion chromium plating using iodine transport involves several steps:

- Production of steel plate size 16 x 13 x 5 mm, grinding it up to surface roughness Ra = 0.10 - 0.15 micron, cleaning and degreasing with acetone;
- Mixture for chrome plating, a powder containing 46% of chromium 47% of aluminum oxide and about 5% iodine metal;
- Loading of the steel plate, and chrome plating mixture in the quartz reactor, reactor degassing, reactor is filled with argon to a pressure of 0.14 - 0.17 MPa;
- Installation of a loaded reactor in a preheated 900°C oven resistance furnace, aging in oven for 3 hours and unloading of the reactor from the oven to cool;
- Unloading of the reactor, cleaning of the surface of the plate from the mixture, analysis of the properties of the coating.

The continuity of the coating was tested with an indicator method using a solution of potassium ferrocyanide, the corrosion resistance was evaluated by the weight loss of the sample per unit of surface area after exposure for 50 minutes in a 25 wt.% H_2SO_4 aqueous solution. The surface roughness measuring device is Mitutoyo SJ - 201 p.

Also, to study the structure of coatings thin sections perpendicular to the plated surface were prepared and examined for metallographic microscope MIM-7 and a scanning electron microscope (SEM) JEOL JSM-35CF with an attachment for energy dispersive electron microprobe (EDEM) analysis Link 860 in order to study the distribution of chemical elements in diffusion layer. Not defined elements: Li, Be, B, C, N, O, F. Phases of the chromized specimens were identified with an X-ray diffraction (XRD) by means DRON – 3 diffractometer.

RESULTS AND DISCUSSION

The surface of the coating (Figure 1) has a fine-grained substrate (dark portions) and large particles having a mean equivalent diameter of 5 microns are arranged therein. According EDEM in dark areas of the surface content of chromium is 90 - 95 wt.%, the rest – the iron, while the larger particles present in the aluminum content at different regions of the surface can vary by several times. This may indicate that the coating is formed by very fine chromium-containing phase and the grains on the surface are caking initial charge. Surface roughness Ra = 3,0 - 3,5 microns. As a result of XRD analysis identified except chromium metal phase and chromium carbides, therefore, it should indicate that the true concentration of chromium in the coating is less than the data obtained from EDEM. The corrosion resistance of the resulting coatings is not inferior to the resistance of stainless steel AISI 304, mass loss after acid treatment is less than 0.5 g / (m 2 h).

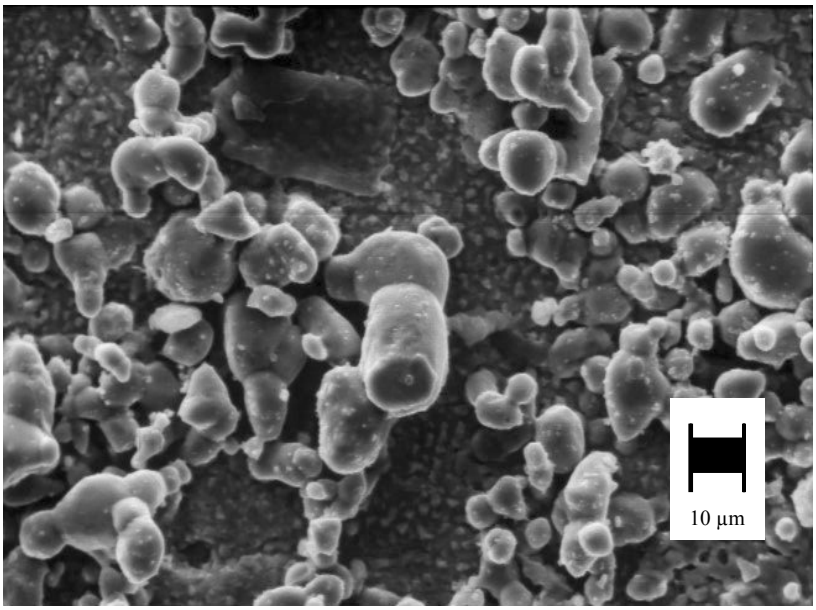

Figure 1. SEM image of the surface chromium coated steel.

The microstructure of the diffusion layer is shown in Figure 2. It can be seen that at the sample surface was formed a glossy coating layer having a thickness of about 4 microns.

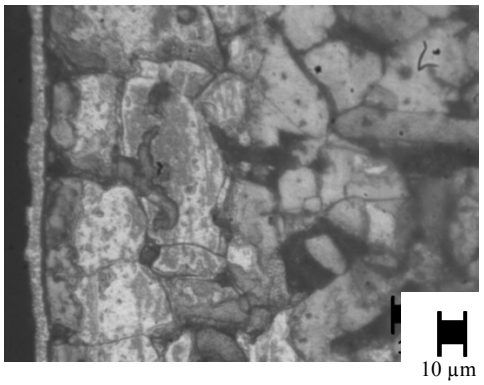

Figure 2. The microstructure of the diffusion layer.

According EDEM surface content of chromium is about 90% (Figure 3).

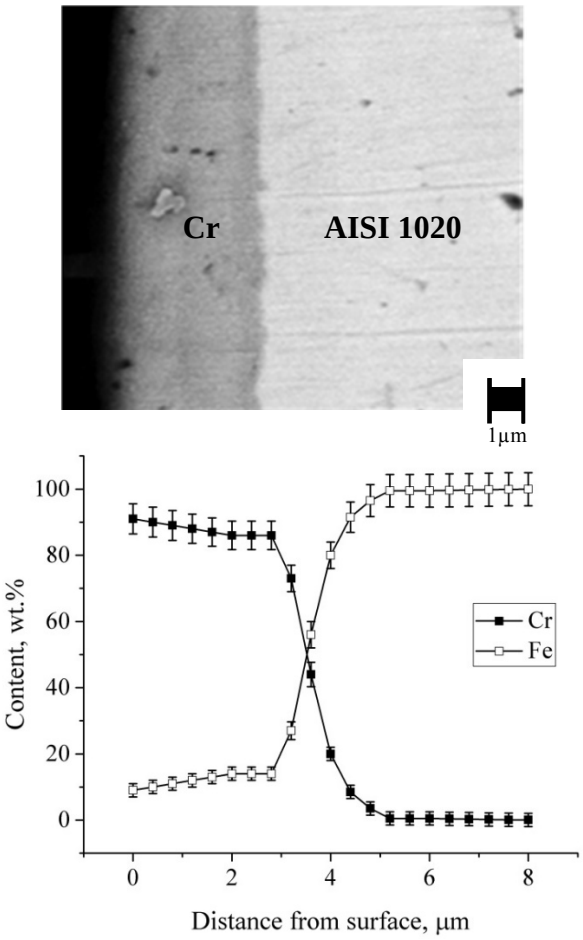

Figure 3. SEM image of a cross-sectional and concentration profiles of Cr and Fe.

CONCLUSION

1. Iodine can be successfully used as a transport agent for obtaining chromium coatings on steel.

2. The coating consists of several layers; Top - nonporous thin layer consisting of chromium and a carbides.

3. The chromium-containing layer formed by the iodine transport, has a high hardness, has no pores and effectively protects against corrosion.

REFERENCES

[1] Filon A. B. Complex diffusive coatings. Moscow, *Mashinostroenie*, 1981. - 136 p. (in Russian).
[2] Loskutov V. F. Diffusive carbide coatings. Kiev, *Technica*, 1991. – 168 p. (in Russian).
[3] Melnik P. I. Technology of diffusion coatings. Kiev, *Technika*, 1978. – 151 p. (in Russian).
[4] Lee. W. Evaluation of microstructures and mechanical properties of chromized steels with different carbon content./W. Lee, J. Duh – *Surface and Coatings Technology* – 2004, V. 177-178, P. 525 – 531.
[5] Meier G. H. Diffusion chromizing of ferrous alloys./G. H. Meier, C. Cheng, R. A. Perkins, W. Barker. – *Surface and Coatings Technology* – 1989, V. 39 – 40, P. 53 – 64.
[6] Rolsten R. F. Iodide Metals and Metal Iodides, New York: Wiley, 1961.
[7] Bogdanov S. P. *Glass Phys. Chem.,* 37, (2), (2011) 172–178.
[8] Bogdanov S. P. Bulletin of the Saint Petersburg State Institute of Technology (Technical University), 16(42), (2012) 24-28 (in Russian).
[9] Bogdanov, S. P. Iodide Transport - Method of Synthesis of Inorganic Materials / S. P. Bogdanov//*Smart Nanocomposites*. – 2014, v. 5, i.1, P.1-8.
[10] Xiaowei Yin, I. Formation of titanium carbide on graphite via powder immersion reaction assisted coating/Yin, I. Xiaowei [etc.]//*Materials Science and Engineering*, A. – 2005, № 396. - P. 107-114.

Smart Nanocomposites
Volume 7, Number 1
ISSN: 1949-4823

STUDY OF LUMINESCENCE AND SURFACE PROPERTIES OF $Y_{1-X}EU_XV_{1-Y}P_YO_4$ PHOSPHORS

L. A. Lebedev*, K. A. Ogurtsov,
S. V. Mjakin, A. A. Nikandrova,
V. V. Bakhmetyev, and M. M. Sychov
Department of Theory of Materials Science,
Saint-Petersburg State Technological Institute (Technical University),
Russia

ABSTRACT

The composition of $Y_{1-x}Eu_xV_{1-y}P_yO_4$ phosphors is optimized to provide the highest luminescence brightness achieved for samples with P and Eu contents 10 and 7 mol. %, respectively. The observed brightness growth prominently correlates with the content of specific centers on the phosphor surface reflecting the formation of species responsible for the luminescence efficiency.

Keywords: luminescence, phosphors, yttrium vanadate, surface functional groups

INTRODUCTION

YVO_4 based phosphors doped with europium (substituting for Y) and phosphorous (substituting for V) are promising as red light emitting components in various light sources of "warmer" white light, in field emission displays and medical applications. The efficiency of these phosphors largely depends on the ratio between their components responsible for the optimal composition, substitution degree and formation of luminescence centers, particularly in the surface layer of the phosphor particles. In our earlier studies [1-3] the content of specific surface centers was found to strongly correlate with the luminescence brightness for ZnS based phosphors with different dopants and activators (Cu, Al, Cl, Mn) that is useful for the prediction of luminescence efficiency for various materials.

* Corresponding author: Lev A. Lebedev, Post-graduate student, Saint-Petersburg State Technological Institute (Technical University), Saint-Petersburg, Russia, Tel. +7 812 4949397, E-mail: 1595lion@gmail.com.

MATERIALS AND METHODS

$Y_{1-x}Eu_xV_{1-y}P_yO_4$ phosphors were prepared by solution-combustion (SC) technique from commercial analytical grade materials without further purification. Y_2O_3 and Eu_2O_3 were dissolved in 35% nitric acid followed by diluting with water, consecutive addition of glycine (upon heating) and a mixed solution of NH_4VO_3, $NH_4H_2PO_4$ and NH_4NO_3, evaporation, heating at 600ºC to initiate the reaction and annealing of the resulting porous material at 800ºC. The prepared phosphors of various composition (1, 7 and 10 mol. % Eu; 0, 10 and 20 mol. % P) were characterized by the study of surface functional groups by adsorption of acid-base indicators with different pKa values according to a procedure described in detail in [4], XRD using a Diffray diffractometer, luminescence spectra analysis using a AvaSpec-3648 spectrometer and measuring the brightness using IL-1700 brightness meter.

RESULTS AND DISCUSSION

According to XRD data, all the prepared samples correspond to YVO_4 structure (Figure 1) [5]. The increase of phosphorous content leads to a certain shift of XRD peaks towards larger angles due to the formation of a solid solution (YPO_4 in YVO_4). Generally, the increase of dopants concentration results in broadening of the peaks that suggests the amorphization of the material due to the decrease of crystallite sizes.

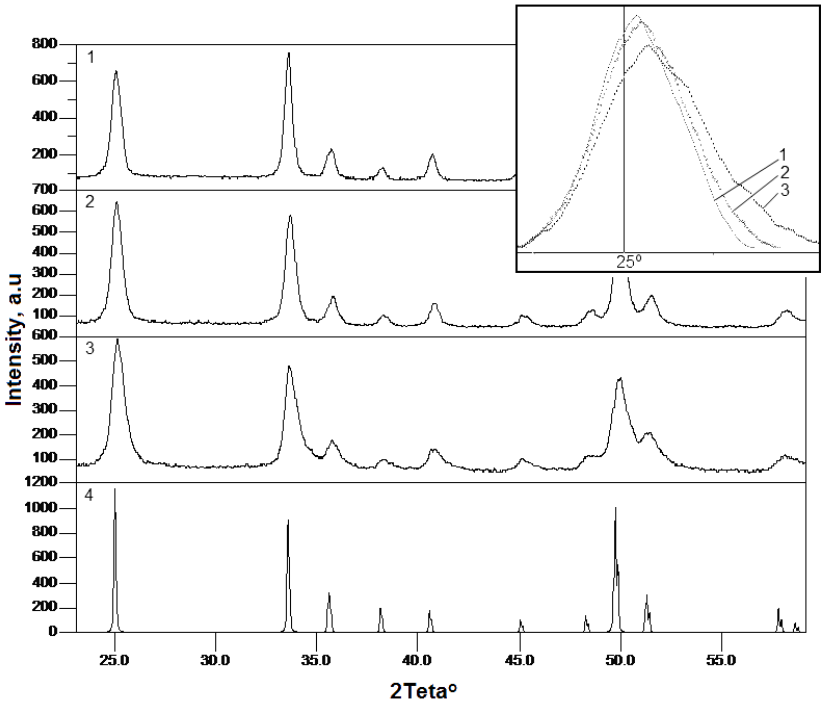

Figure 1. XRD patterns for the samples with phosphorous content 0 (1), 10 (2) and 20 mol.% (3) and pattern for the card № 16-250* ICDD PDF database(4).

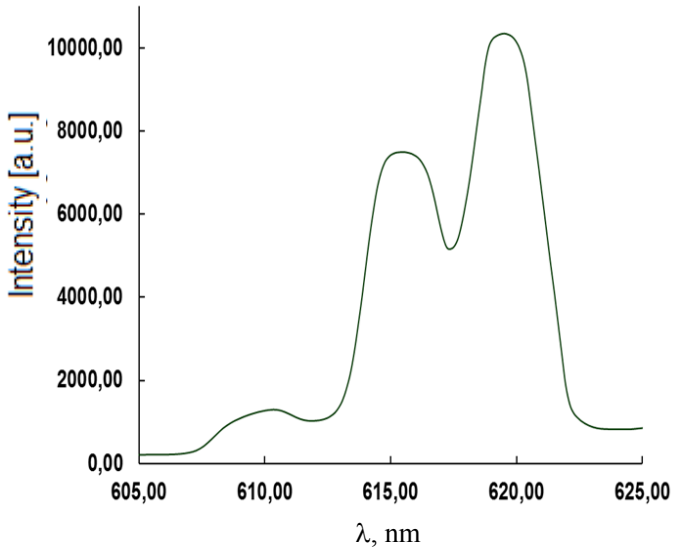

Figure 2. Luminescence spectrum of the synthesized phosphors.

The luminescence spectra of the samples are intrinsic to yttrium vanadate with two prominent peaks at 615 and 619 nm corresponding to $^5D_0 \rightarrow {}^7F_1$ magnetic dipole transition and $^5D_0 \rightarrow {}^7F_2$ electric dipole transition, respectively (Figure 2).

The data on luminescence brightness of the synthesized phosphors summarized in Table 1 indicate that among the considered materials the optimal Eu content is 7 mol.% and the overall highest efficiency is achieved for the sample with 7 mol.% Eu and 10 mol. % P.

The analysis of surface functional composition of the synthesized materials allowed us to reveal the correlations between their composition, content of specific centers on their surface and luminescence efficiency. For phosphorous-free samples the increase of Eu concentration results in a prominent and similar (featuring with equal correlation coefficients 0.85 with Eu content) growth in the content of Broensted acidic centers with pKa 1.3 and 2.5, probably corresponding to OH-groups bonded with Eu atoms in different oxidation states or spatial environment. However, no prominent effects of the surface functionality on the luminance was observed.

Table 1. Luminescence brightness of the synthesized phosphors

P content, mol.%	Eu content, mol.%	Luminescence brightness, a.u.
0	1	14.7
0	7	17.5
0	10	15.8
10	1	11.7
10	7	20.9
10	10	11.5
20	1	11.5
20	7	17.8
20	10	14.2

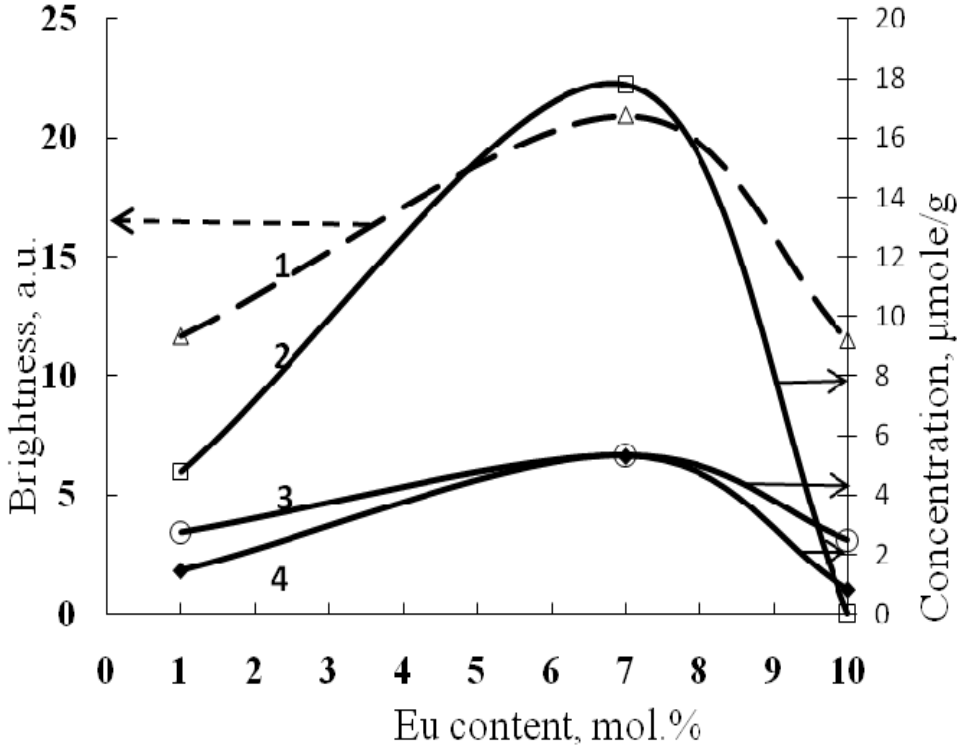

Figure 3. Luminescence brightness (1) of the samples with 10 mol.% P and contents of centers with pKa -4.4 (2), 7.3 (3) and 1.3 (4) on their surface as a function of Eu content.

The samples containing 10% mol. P feature with the most significant correlations between Eu concentration, surface functionality and luminescence brightness. Particularly, for this series of samples the brightness correlates with the contents of centers with pKa 1.3, 7.3 and -4.4 with the correlation coefficients 0.97-0.99 and a prominent maximum at 7 mol.% Eu (Figure 3) corresponding to the highest brightness among all the studied phosphors (Table 1).

Furthermore, the contents of centers with pK_a 1.3 and pK_a 7.3 in this sample (also the highest among the synthesized materials) are equal to each other (5.3 μmole/g as shown in Figure 3) that suggests their interrelated nature, probably reflecting the most efficient P and Eu incorporation into the vanadate structure and formation of both acidic (pK_a 1.3) and neutral (pK_a 7.3) Broensted centers represented by hydroxyls connected with simultaneously displaced V and Y ions, accordingly. Lewis basic centers with pKa -4.4 probably correspond to oxygen atoms connecting ions as bridging groups and stabilizing the desirable surface species responsible for the luminescence efficiency.

A series of samples with phosphorous content 20 mol.% also features with the highest brightness at Eu concentration 7 mol.%, however in this case brightness correlates with the content of centers with pKa 5.0 and 14.2 (Figure 4). This suggests essential changes in the surface functionality, particularly increased content of Lewis acidic centers (pKa 14.2) instead of oxygen atoms due to a high level of P-doping as well as the most effective substitution of target atoms at Eu content 7 mol.% yielding Broensted sites with pKa 5.0 (likely as a result of hydroxylation of disrupted element-oxygen bonds) and additional cationic (Lewis acidic) centers on the surface.

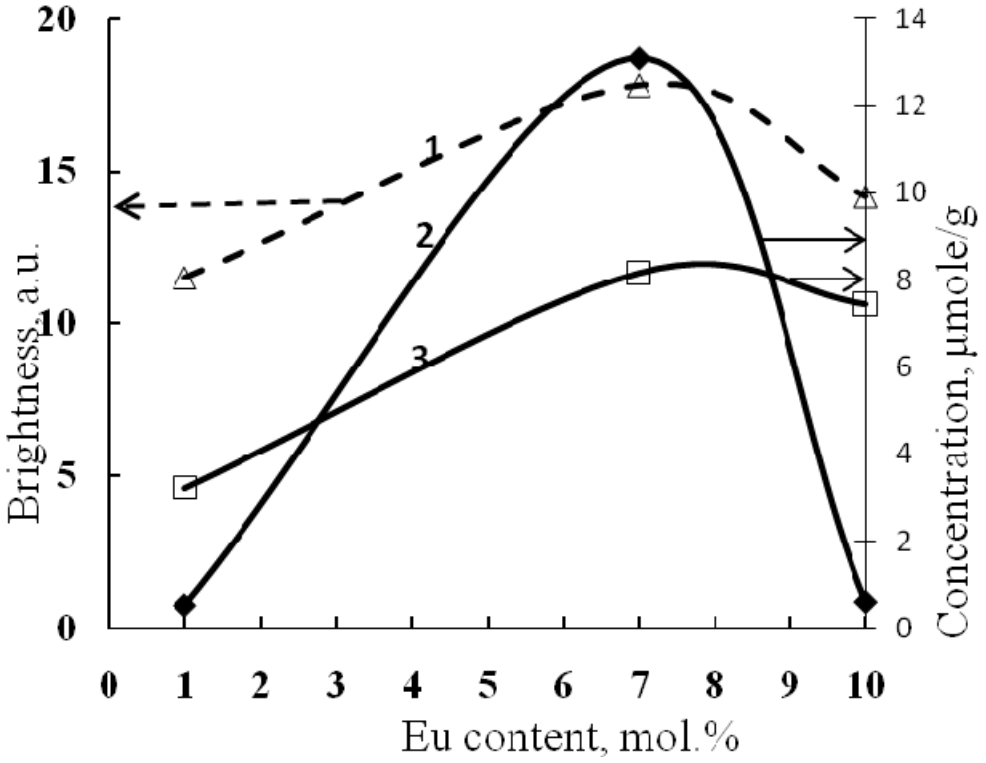

Figure 4. Luminescence brightness (1) of the samples with 20 mol.% P and contents of centers with pKa 5.0 (2) and 14.2 (3).

CONCLUSION

Generally, the obtained results allowed us to determine the optimal composition of $Y_{1-x}Eu_xV_{1-y}P_yO_4$ phosphors providing the highest luminescence brightness at 7mol.% Eu and 10 mol.% P, probably due to the most effective replacement of Y by Eu and V by P with the stabilization of the required surface species. The optimized composition is found to correlate with the surface functionality, particularly with the interrelated increase in the content of specific Broensted acidic centers to equal extreme amounts, probably resulting from the formation of hydroxyls connected with the displaced V and Y atoms. The considered data requiring a more detailed optimization in respect of both doping level of the considered phosphors and their surface analysis are promising for the improvement of target performances for various kinds of phosphors as well as for the development of specific approaches to their synthesis and modification.

ACKNOWLEDGMENTS

The reported study was funded by RFBR according to the research project No. 16-33-00998 мол_ а.

REFERENCES

[1] Sychov M. M., Mjakin S.V., Nakanishi Y., Korsakov V. G., Vasiljeva I. V., Bakhmetjev V.V., Solovjeva O. V., Komarov E. V. *Applied Surface Science,* 244, (1-4) (2005), 461-464.

[2] Bakhmetjev V. V., Sychov M. M., Korsakov V. G., *Russian J. Appl. Chem.*, 83, (11), (2010), 1903-1910.

[3] Bakhmetyev V. V., Mjakin S. V., Korsakov V. G., Abyzov A. M., Sychov M. M, *Glass Physics and Chemistry*, 37, (5), (2011), 549-554.

[4] Vasiljeva I. V., Mjakin S. V., Rylova E. V., Korsakov V. G., *Russian J. Phys. Chem*., 76, (1), (2002), 71-76.

Smart Nanocomposites
Volume 7, Number 1
ISSN: 1949-4823

FRACTAL STRUCTURE AND ELECTRICAL PROPERTIES OF PERCOLATION SENSOR LAYERS

S. S. Nalimova*, A. A. Bobkov, and V. A. Moshnikov
Micro- and Nanoelectronics Department
St. Petersburg Electrotechnical University ″LETI″
St. Petersburg, Russia

ABSTRACT

Binary oxides ZnO and Fe_2O_3, and the ferrite phase $ZnFe_2O_4$ are synthesized by chemical coprecipitation. Gas sensitive properties of the samples are studied by measurements of changes in resistivity and impedance under acetone and ethanol vapors exposure compared to those in air. It was found that the sensitivity of the samples reaches 10^5. The model of gas sensitive layer as percolation cluster near percolation threshold is proposed and discussed. The peculiarities of electrophysical properties are described by the proposed model.

Keywords: gas sensors, metal oxides, chemical coprecipitation, percolation cluster, Mandelbrot-Given fractal, impedance spectroscopy

INTRODUCTION

Metal oxide gas sensors of adsorption type have been widely studied for many decades. Their operating principle is based on the increase in conductivity of sensitive element in the surface region as a result of sorption of the analyzed gas [1-3]. The changes in resistance of semiconductor metal oxides are caused by the variation of electrons concentration in the conduction band (or holes concentration in the valence band) because of the charge exchange with adsorbed gaseous molecules. First, oxygen molecules are adsorbed on the metal oxide surface. Electron transfer from semiconductor volume to adsorbed oxygen molecules leads to band bending in subsurface region. Therefore, intergranular necks (which are electron motion channels) are reduced or covered. When reagent gas interacts with adsorbed oxygen, electron transfers back to the conduction band and reaction products are desorbed in neutral form [4].

A great variety of binary oxides and their composites (SnO_2, ZnO, TiO_2, In_2O_3, WO_3, Fe_2O_3 etc.) have suitable properties (band gap, chemical stability etc.) for their use as

* Corresponding author email: sskarpova@list.ru.

sensitive elements [5-7]. Low sensitivity and selectivity are the significant disadvantages of adsorption sensors. A lot of research and development has been done to improve the sensor properties. The most widely used approach is the formation of nanostructured metal oxides, including nanoparticles, nanorods, nanobelts and hierarchical structures. Sensors based on nanostructured metal oxides should have better characteristics compared to corresponding bulk materials because of two main reasons. The first one is the high surface-to-volume ratio. Second, the radius of nanostructured element is comparable with depletion layer thickness over a wide temperature range that results in a strong dependence of their electronic properties on surface processes [8]. Noble metal addition also lead to the enhancement of sensitivity via spill-over effect [9].

Most of the research on the sensor principle is focusing on the properties of a single grain-grain contact, and it is only recently that also collective, network, or percolation effects have been taken into account [10].

The aim of this study was to investigate the possibility of sensitivity enhancement of metal oxide layers based on percolation effects. Gas sensitive layers with percolation cluster structure near percolation threshold were synthesized. Their sensitivity is higher by several orders of magnitude than the one of most known sensors.

EXPERIMENT

Nanostructured layers of ZnO, Fe_2O_3 and $ZnFe_2O_4$ were prepared via chemical co-precipitation method described in details in [11]. Electrical contacts are formed using contactol (3g SILBERLEITLACK, Art-№.530042). Gas sensitive properties of synthesized metal oxide layers were studied under acetone and ethanol vapors exposure (1000 ppm). Gas sensitivity value was calculated as $S = (R_{air} - R_{gas})/R_{gas}$, where R_{air} – sample resistivity in air, R_{gas} – sample resistivity under reactant gas exposure. Electrophysical properties of the obtained samples are studied by impedance spectroscopy in the frequency range 100 Hz-500 kHz in air atmosphere and under acetone and isopropanol vapors exposure [12]. Time dependence of sample resistivity under acetone and ethanol vapors exposure is simulated within the limits of percolation cluster properties.

RESULTS AND DISCUSSION

Growth processes at co-precipitation lead to the formation of pores with fractal structure of surface. The reason of fractal structure formation is assembly peculiarities at initial stages. Particles move because of Brownian motion in the conditions of diffusion-limited aggregation. At co-precipitation in aqueous solution OH-groups take part in structure formation and then evaporate as a result of drying and annealing that leads to pores formation. This method allows us to obtain the percolation clusters near percolation threshold. It is hardly possible to produce such structures by sol-gel method because of a sharp decrease in entropy of the system when ordering (inorganic polymers growth) at polycondensation. Spinodal decay results in the formation of net-like structures [13], which are far after percolation threshold.

Gas sensitivity measurements show that $ZnFe_2O_4$ sample has the highest sensitivity to both reactant gases [11]. It's sensitivity to ethanol and acetone vapors are 200 and 100000 respectively.

The changes in electrophysical properties of sensor materials are usually interpreted within the limits of model based on Debye screening length and the formation of depleted regions [14]. If gas-sensitive layer consists of grains with size smaller than doubled Debye screening length or intergranular necks are commensurable with this value, then it has high gas sensitivity. But the ratio of resistivities in air and under reactant gas exposure cannot be as high as 10^5.

Two states of percolation cluster with different resistivity values are shown in Figure 1. The state 1 before percolation threshold corresponds to high resistivity of gas-sensitive layer in air atmosphere. When reducing gas molecules appear, transfer through percolation threshold occurs and resistivity decreases, that corresponds to the state 2. The changes in resistivity do not limited by depleted region approach.

Among all models of percolation clusters (Skal-Shklovsky-de Zhen model, drops and bonds model, model based on Serpinsky carpet, hierarchical model) Mandelbrot-Given fractal curve was chosen for explanation of experimental results [15]. This model is the most suitable for description of porous sensor structures. Another peculiarity of this model is Haudorf-Bezikovich fractal dimension that close to the one of infinite cluster in two-dimensional space. In air chemical adsorption of oxygen molecules occurs on the surface of metal oxide layer, leading to the blocking of fractal conductive branches. In this case the structure is in the state before percolation threshold and subsequently it has high resistivity. Reducing gas molecules are adsorbed on the layer surface, interact with oxygen molecules, and reaction products are then desorbed. As a result, current paths become unblocked, leading to the transfer through percolation threshold and a significant decrease in resistivity. The unblocking of conductive branches results in the formation of loops with different sizes. The described processes are illustrated by Figure 2.

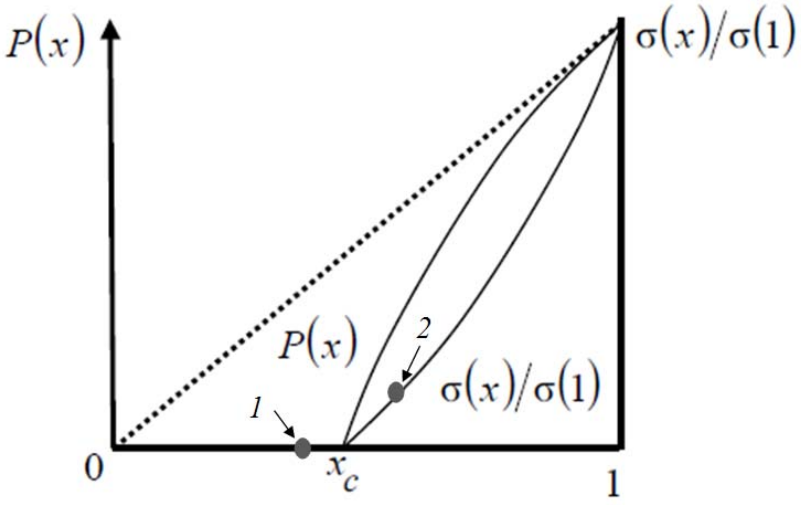

Figure 1. Dependence of power P and normalized conductance $\sigma(x)/\sigma(1)$ of percolation cluster on the part of conductive cells (*1* – in air, *2* – under a reducing gas exposure).

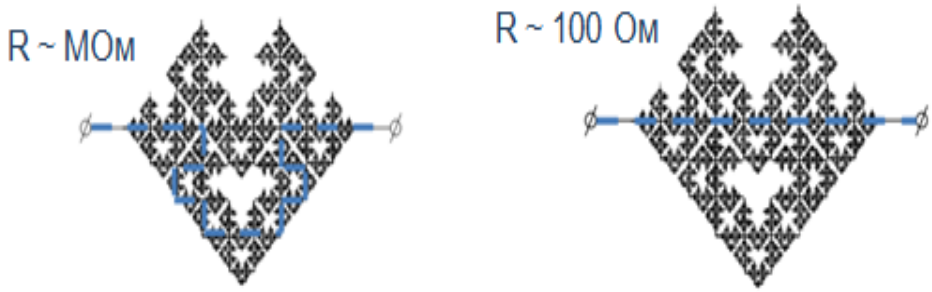

(A) (B)

Figure 2. Current paths in Mandelbrot-Given cluster: a – in air, b – under reducing gas exposure.

It should be noted that in real structures individual grains are percolation clusters and correspond to the described model. The samples have quasi-granular structure, and different grains have different percolation characteristics. The properties of the whole system depend on grains assembly hierarchy.

As an example the results of impedance spectroscopy (Nyquist diagrams) for ZnO layer are shown in Figure 3. It was found that under reducing gases exposure inductive component appears in the low-frequency region of Nyquist diagrams, which affects the impedance hodograph in the IV quarter of the trigonometric circle. According to the model of Mandelbrot-Given, fractal structure contains loops of different diameters near the percolation threshold. At high frequencies the loops do not participate in the transport of charge carriers as equivalent to a certain inductance. At low frequencies, on the contrary, the shunt effect occurs. The transport of charge carriers through loops is more profitable as compared to the capacitance which corresponding a dielectric layer between two conductive semiconductor grains. Thus, inductive characteristics of impedance spectroscopy at low frequencies follow from the described model [16].

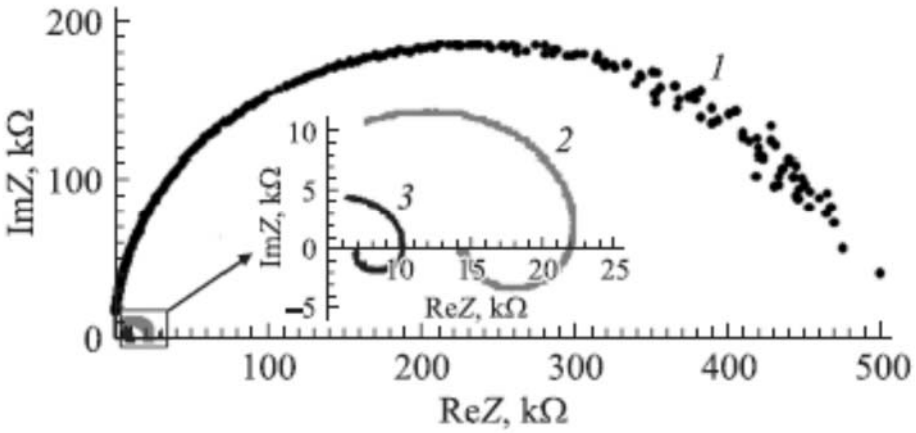

Figure 3. Nyquist diagrams of ZnO layer: *1* – in air, *2* – under isopropanol vapors exposure, *3* – under acetone vapors exposure.

The dependence of percolation cluster resistivity on the part of conductive cells is described by the following equation:

$$R \sim 1 / (x - x_c)^t, \tag{1}$$

where t is the conductivity critical index ($t_2 = 1.3$ for space dimension $d = 2$ and $t_3 = 1.6 – 1.7$ for $d = 3$). Time dependence of the sample resistivity under acetone and ethanol vapors exposure is simulated using the equation (1).

Experimental results are compared to theoretical model (Figure 4). It is assumed that when gas exposure time increases, the part of conductive cells also increases because of the unblocking of adsorption sites. The transfer through percolation threshold under acetone and ethanol vapors exposure occurs after 5 s and 20 s respectively. The values of conductivity critical index are 1.75 and 1.5 under acetone and ethanol vapors exposure respectively.

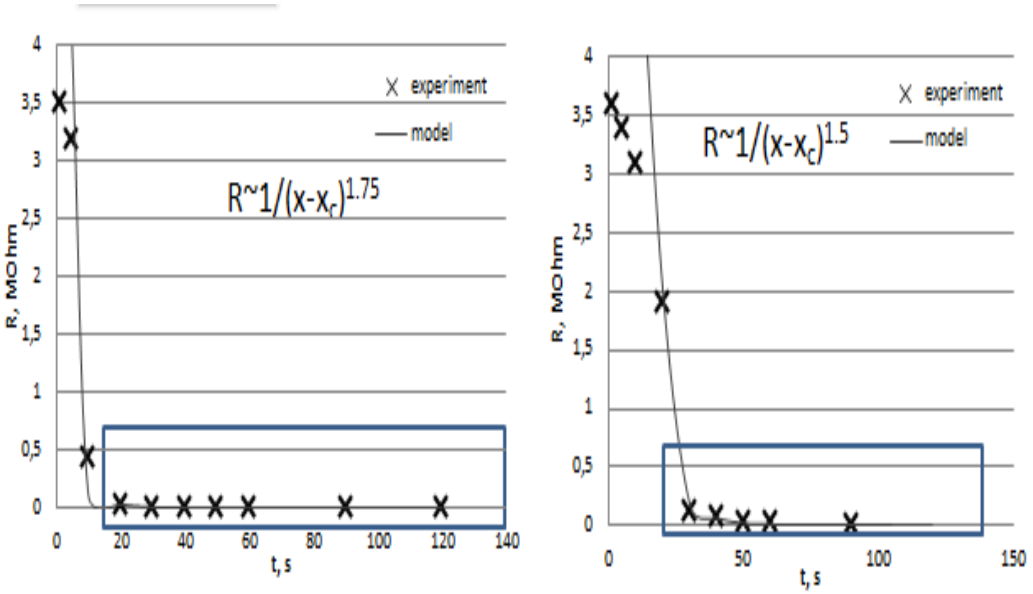

(A) (B)

Figure 4. Time dependence of $ZnFe_2O_4$ resistivity: *a* – under acetone vapours exposure, *b* – under ethanol vapors exposure.

CONCLUSION

Metal oxide layers with fractal structure are described. High values of gas sensitivity are explained with the formation of a percolation cluster near the percolation threshold, which can be qualitatively described by Mandelbrot-Given model. Oxygen chemisorption takes the system to the state before the percolation threshold, characterized by high resistance, and desorption of the products of reaction between oxygen and a reducing gas leads to the transfer through percolation threshold with a substantial decrease in resistance.

ACKNOWLEDGMENTS

The investigation was performed within the project part of the state task №16.2112.2014/K in the scientific research.

REFERENCES

[1] Y.-F. Sun, S.-B. Liu, F.-L. Meng, J.-Y. Liu, Z. Jin, L.-T. Kong, J.-H. Liu, *Sensors,* 2012, 12, 2610-2631.

[2] G. Korotcenkov, M. DiBattista, J. Schwank, V. Brinzari, *Mater. Sci. Eng*., 2000, 77, 33-39.

[3] M. A. Carpenter, S. Mathur, A. Kolmakov, *Metal Oxide Nanomaterials for Chemical Sensors*, Springer Science+Business Media, New York, 2013.

[4] Gaskov A. M., Rumyantseva M. N., Russ. *J. of Appl. Chem*., 2001, 74(3), 440-444.

[5] N. D. Hoa, N. V. Duy, S. A. El-Safty, N. V. Hieu, *J. of Nanomaterials,* 2015, 1, 1-14.

[6] E. Gracheva, V. A. Moshnikov, E. V. Maraeva, S. S. Karpova, O. A. Alexsandrova, N. I. Alekseyev, V. V. Kuznetsov, G. Olchowik, K. N. Semenov, A. V. Startseva, A. V. Sitnikov, J. M. Olchowik, *J. Non-Cryst. Sol*., 2012, 358, 433-439.

[7] E. Comini, *Analytica Chimica Acta*, 2006, 568, 28-40.

[8] T. V. Peshkova, D. Ts. Dimitrov, S. S. Nalimova, I. E. Kononova, N. K. Nikolaev, K. I. Papazova, A. S. Bozhinova, V. A. Moshnikov, E. I. Terukov, *Technical Physics*, 2014, 59(5), 771-776.

[9] M. Hübner, D. Koziej, J.D. Grunwaldt, U. Weimar, N. Barsan, *Phys. Chem. Chem. Phys.,* 2012, 14(38), 13249-54.

[10] Percolation Effects in Metal Oxide Gas Sensors and Related Systems, C.-D. Kohl and T. Wagner (eds.), in Gas Sensing Fundamentals, *Springer Series on Chemical Sensors and Biosensors,* 2014, 15, 247–278.

[11] S. S. Karpova, V. A. Moshnikov, S. V. Mjakin, E. S. Kolovangina, Semiconductors, 2013, 47(3), 369-372.

[12] A.S. Bozhinova, N.V. Kaneva, S.A. Syuleiman, K.I. Papazova, D.T. Dimitrov, I.E. Kononova, S.S. Nalimova, V.A. Moshnikov, E.I. Terukov, *Semiconductors,* 2013, 47(12), 1636-1640.

[13] E. Gracheva, V. A. Moshnikov, S. S. Karpova, E. V. Maraeva, *J. of Physics: Conference Serie*s, 2011, 291, 012017.

[14] N. Barsan, U. Weimar,*J. of Electroceramics*, 2001, 7, 143-167.

[15] B. B. Mandelbrot, J. A. Given, *Phys. Review Lett*., 1984, 52, 1853-1856.

[16] V. A. Moshnikov, S. S. Nalimova, B. I. Seleznev, *Semiconductors,* 2014, 48(11), 1535-1539.

Smart Nanocomposites
Volume 7, Number 1
ISSN: 1949-4823

EVOLUTION OF COPPER(II) OXIDE NANOSTRUCTURES IN POROUS GLASS MATRIX

Vyacheslav N. Pak*, Oleg V. Golov, and Dmitry V. Formus
Herzen State Pedagogical University of Russia,
Saint Petersburg, Russia

ABSTRACT

Copper(II) oxide was introduced in an amount of 3.5–56.4 mass % into a porous glass by repeated cycles of impregnation with an aqueous solution of copper(II) nitrate followed by dehydration and thermal decomposition of the salt. The results of conductivity measurements, in combination with the data on the copper oxide amount and the specific area of the porous carrier, reflect the formation of sequential cupric oxide monolayer on the surface of pore walls. The temperature dependencies of the electric conductivity demonstrate a counteraction of activated and metal-like behavior.

Keywords: porous glass, CuO, monolayer, electrical conductivity

INTRODUCTION

Porous glasses (PG), in which the pore radius can be reliably controlled in the range r = 2–100 nm [1-3] offer wide possibilities for the investigation of substances in the nanodimensional state. It is important that PGs with highly developed pore structure and surface area allow the compounds to be introduced in amounts sufficient for the experimental investigation. The nanoparticles and monolayers of transition metal oxides in PG are promising materials in which dimensional features of the optical and electrical properties are well manifested [1-3]. However, peculiarities of the electric conductivity in such systems with small number of atoms (10^{15}–10^{16} cm^{-2}) of d –elements in the oxides formed at the initial stage of filling of the silica surface remain unstudied.

The results reported in this letter demonstrate a specific stepwise increase and unusual temperature dependencies of the electric conductivity in the course of copper(II) oxide deposition in PG.

* E-mail: pakviacheslav@mail.ru.

EXPERIMENTAL PROCEDURE

The experiments were performed on PG plates prepared using standard methods [4] with dimensions 1·1·0.1 cm, predominant pore radius of r = 70 nm and specific surface area of S = 22 m^2/g. The PG was modified by adding copper(II) oxide through diffusion impregnation of the plates with an aqueous solution of $Cu(NO_3)_2$ with a concentration of 0.15 M, followed by dehydration at 120^0C and thermal decomposition of the intercalated salt by heating in air at 400^0C. Repeated cycles of this treatment allowed the oxide step-by-step growth on the walls of through channels in PG to be performed in a controlled way and reliably monitored by weighing. *X*-ray diffraction measurements confirmed the amorphous nature of all CuO/PG samples examined. The d. c. electric resistance and its temperature dependencies were measured ("Novocontrol Concept 41", Germany) in dry atmosphere across the CuO/PG samples with clamp gold electrodes. The conductivity σ calculated with allowance of a real size of the glass plates had a clear electronic character. In none of the experiments we have observed the emergence of polarization potentials or residual currents after cutting off the external voltage.

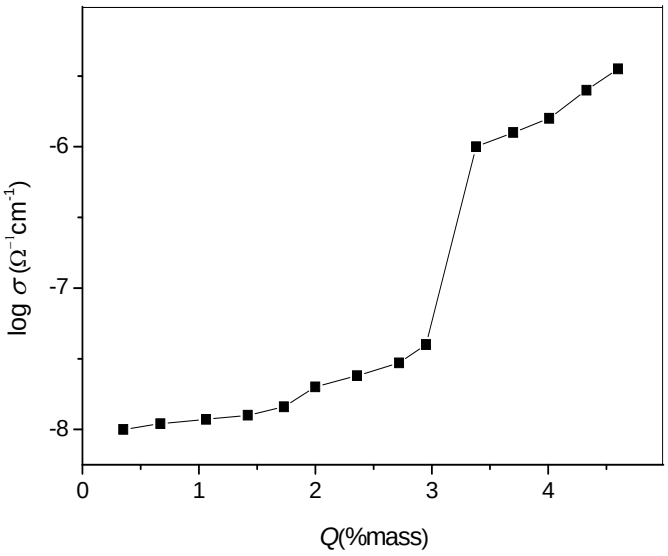

Figure 1. Electrical conductivity dependence on the amount of copper(II) oxide (% mass) in PG.

RESULTS

The conductivity (σ) dependence on the content of CuO (Q) in PG exhibits a monotonic increase at the first steps of oxide deposition followed by a sharp jump in the region of Q = 2.95–3.38% mass (Figure 1) indicating a percolation threshold. The temperature dependencies of σ in the modest range investigated (Figure 2) show a drastic difference between the CuO/PG samples "before" and "after" percolation threshold. The samples *1-9* listed in Table 1 demonstrate unusual change from low-activated to metal-like conductivity

accompanied by gradual shift of smooth maximum to high temperature. Those maxima in turn become less pronounced as the amount of CuO increases. By contrast, the plots of log σ(1/T) in case of samples *10-14* ($Q \geq 3.38$ % mass) turns out to be linear in all temperature range. Attention must be given to the low values of the electrical activation energies (Table 1) calculated from the slopes of log σ(1/T) dependencies *10-14* and from their initial linear parts in case of samples *1-9*.

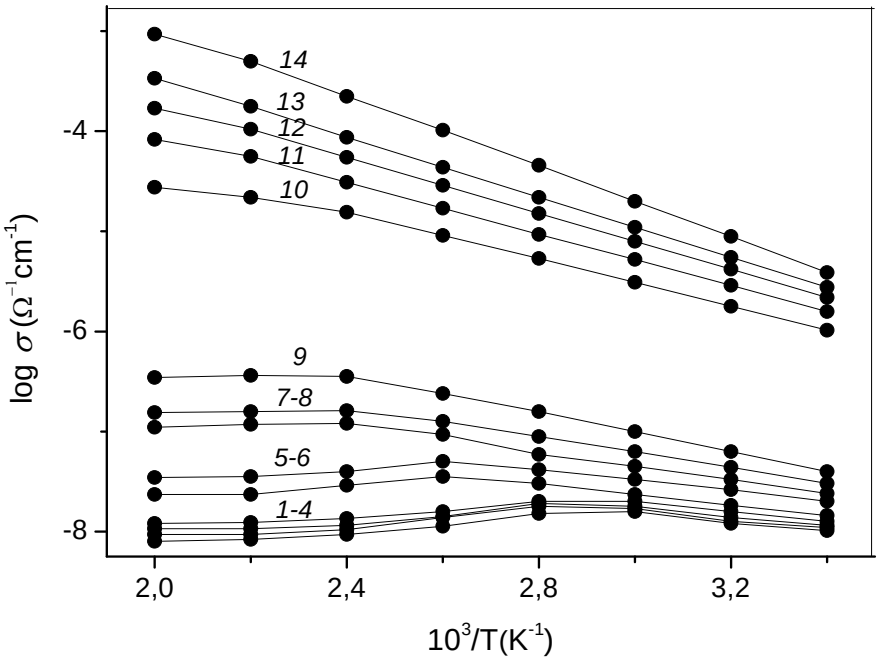

Figure 2. Electrical conductivity as a function of the reciprocal temperature for a series of CuO/PG sample listed in Table 1.

Table 1.

Sample	CuO content (% mass)	σ_{20} (Ω^{-1} cm^{-1})	Activation energy (eV)
1	0.35	$1.1 \cdot 10^{-8}$	0.07
2	0.67	$1.2 \cdot 10^{-8}$	0.07
3	1.06	$1.2 \cdot 10^{-8}$	0.08
4	1.42	$1.3 \cdot 10^{-8}$	0.09
5	1.73	$1.5 \cdot 10^{-8}$	0.10
6	2.00	$2.0 \cdot 10^{-8}$	0.11
7	2.36	$2.4 \cdot 10^{-8}$	0.13
8	2.72	$3.0 \cdot 10^{-8}$	0.15
9	2.95	$4.0 \cdot 10^{-8}$	0.18
10	3.38	$1.3 \cdot 10^{-6}$	0.23
11	3.70	$1.4 \cdot 10^{-6}$	0.25
12	4.01	$2.0 \cdot 10^{-6}$	0.27
13	4.33	$2.5 \cdot 10^{-6}$	0.29
14	4.60	$3.2 \cdot 10^{-6}$	0.33

Based on the results obtained, a probable model of step filling of PG surface may be suggested. As far as PG conductivity is low ($\sigma < 10^{-9}$ Ω^{-1} cm^{-1}) we can assume that values of 10^{-8} Ω^{-1} cm^{-1} obtained at the initial steps of CuO deposition owes to the formation of some percolating chains of conjugated copper oxide polyhedrons. Indeed, being reduced to a specific surface area of S = 22 m^2/g, the oxide content in PG Q ~ 0.35 % mass (sample *1*) corresponds to ~ one CuO formula unit per 10 nm^2. In case of such a small "surface density" the most reasonable way for σ–level explanation implies some conducting chains organization at the first steps of the oxide deposition.

This guess also provides a first explanation for the peculiarities of the electrical T-dependencies (Figure 2). Low values of the activation energies (Table 1) are associated with excitation of the heat oscillations within conducting chains, thus enhancing a $3d_\pi$–$2p_\pi$ conjugation of Cu–O–Cu bonds (and possibly, a direct $3d\cdots3d$ overlap). The increase of the oscillations amplitude can gradually provoke a metal-like conductivity resulting in its inverse T-dependencies (Figure 2, *1-6*). In the course of CuO monotonous growth in PG the lateral Cu–O–Cu bonds are formed and gradually prevail, which adds to the oxide structure rigidity and reduces the oscillations amplitudes. That's why the dependencies log σ(1/T) maxima become smoother and shift to a high temperature (Figure 2, *5-9*) while the activation energy values steadily rise up (Table 1). Thus, T-dependencies of the electric conductivity demonstrate a counteraction of activated and metal-like behavior.

A further development of two-dimensional oxide structures finally results in the intense formation of multiple contacts between them in the percolation region. The close to monolayer state of copper oxide polyhedrons in samples *9-10* relates to the fact that, the percentage content at Q = 2.95–3.38 % mass closely corresponds to ~10^{15} of oxide formula units per cm^2. A nonplanar distribution seems not to be probable: in such a case, we have to explain why rather distant three-dimensional oxide islands on reaching that Q suddenly "spread" over the surface to merge and provide for the observed jump in the conductivity.

Thus, there is ground to believe that the monotonous increase in the mass fraction of the copper(II) oxide proceeds under the conditions of a strong interaction with the carrier surface preventing coalescence of the deposit. The oxide polyhedra fixed on the walls of through channels of PG by Si–O–Cu bonds actually may be looked at as a surface copper(II) silicate. This makes possible "grafting" of a numerous percolating chains with specific T-dependencies of conductivity followed by their steady two-dimensional reorganization and finally the monolayer formation.

CONCLUSION

Progressive increase in the copper(II) oxide content in porous glass is accompanied by a monotonic increase in electrical conductivity, which subsequently exhibits an abrupt jump within a narrow composition range corresponding to monolayer coverage of the support surface. Based on the results obtained, a model was proposed which states that the porous glass surface is covered in a stepwise manner, via predominant formation of extended copper(II)-oxygen chains as the first step and subsequent change to 2D structures, eventually leading to oxide monolayer.

ACKNOWLEDGMENTS

This work was supported by the Ministry of Education and Science of Russia within the base part of the Government Instruction.

REFERENCES

[1] Pak V. N., Gavronskaya Yu. Yu., Burkat T. M. Porous glass and nanostructured materials. N.Y.: Nova Science Publishers (2015).

[2] Pak V. N., Gavronskaya Yu. Yu., Shilov S. M. Optical and electrical properties of low dimensional forms of substances in porous glass//*Glass Phys. Chem.* 41(1), (2015), 68–72.

[3] Enke D., Janovski F., Schwieger W. Porous glass in the 21st century – a short review//*Micropor. Mesopor. Mater*. 60(1), (2003), 19-30.

[4] Lyubavin M. V., Burkat T. M., Pak V. N. Fabrication of silica structures with controlled pore structure//*Inorganic Materials*, 44(2), (2008), 203-206.

Smart Nanocomposites
Volume 7, Number 1
ISSN: 1949-4823

EFFECT OF THE SYNTHESIS METHODS ON THE CRYSTAL STRUCTURE AND LUMINESCENCE OF $ZnAl_2O_4:Eu^{3+}$ PHOSPHORS

N. S. Podsypanina*, L. A. Lebedev, and M. M. Sychov
Saint Petersburg State Technological Institute, Technical University, Russia

ABSTRACT

$ZnAl_2O_4:Eu^{3+}$ phosphors powders were synthesized with different concentration of activator ions by using sol-gel (SG) method and solution combustion (SC) technique. The effect of the method of synthesis and concentration of Eu^{3+} ions on the structure and luminescence properties of zinc aluminate phosphor were investigated. X-ray diffraction pattern confirmed that the fibers were composed of the cubic $ZnAl_2O_4$ phase. The calculation of the crystallite size according to Scherrer formula and the maximum were for obtained 0.12% of Eu^{3+} ions by using SG and for samples prepared by SC was 0.15%. Luminescence spectra shown peaks at 612 and 618 nm. The intensity of all the emission bands reached at 0.12% and 0.24% depending on activator concentration by using SG and SC techniques, respectively. So the crystallinity, luminescence spectrum profiles and luminescence of phosphors can be effectively adjusted by the variation of method and dopant (activator) concentration.

Keywords: zinc aluminate phosphor, zinc aluminate spinel, phosphor, XRD, luminescence

INTRODUCTION

Field emission displays (FED) is an advanced direction in display technologies providing flat screens with large diagonal size. In contrast to cathode ray technology (CRT) also based on electron beam impact to excite a phosphor layer on the screen, FED are more compact because they do not require a huge deflection yoke for electron beam control. Furthermore, advantageous features of such screens also include low power consumption, wide viewing angle, high image quality and small response time [1]. FED display consists of two glass panels. The first panel is coated with electron emitters on the other one with phosphor layer similar to that used in conventional CRT. Unlike conventional CRT, each pixel involves three electron emitters corresponding to red, green and blue colors [2].

* podsypaninanataly@gmail.com,

Spinel $ZnAl_2O_4$ is a direct semiconductor with a bandgap 3,6-3,9 eV. $ZnAl_2O_4$ has the symmetry of cubic, with a space group Fd3m [3]. The unit cell contains 32 oxygen anions, which forms a dense cubic packing. There is 64 tetrahedral and 32 octahedral cavities. By the nature of the distribution of cations at the tetrahedral positions spinel's are divided: normal spinel (8 tetrahedral occupied by cations Zn^{2+}, 16 octahedral - cations Al^{3+}) and outstanding spinel(8 tetrahedral occupied by Al^{3+}, 16 octahedron - 8 Zn^{2+} and 8 Al^{3+} 8 and the cations Zn^{2+} and Al^{3+} in the octahedral voids can be distributed statistically and orderly)[4].

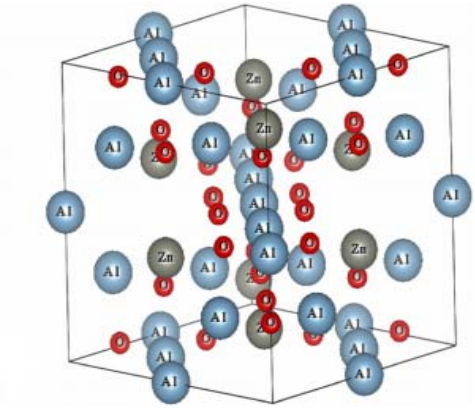

Figure 1. Schematic of crystal structure of $ZnAl_2O_4$.

$ZnAl_2O_4$ has good chemical and thermal stability. $ZnAl_2O_4$ phosphors activated by rare earth metals are studying because they have the unique luminescence properties.

Various preparation methods have been proposed in the literature such as sol–gel, solid-state reaction, hydrothermal synthesis and combustion process etc. [5]. In this, work $ZnAl_2O_4$: Eu^{3+} phosphors were synthesized as a red emitting component of pixel. Two series of samples prepared using sol-gel (SG) and solution combustion (SC) methods.

EXPERIMENT

Preparation of $ZnAl_2O_4$: Eu^{3+}

The sol-gel technique involves the following steps: preparing of precursor solution in distilled water, neutralizing of solution by NH_4OH with precipitate formation, precipitate filtration on Buchner funnel, drying in vacuum cabinet and annealing at 800°C for two hours [6].

SC technique involves evaporation of the reaction mixture including zinc nitrate, aluminum nitrate and urea as a fuel, introducing the prepared viscous solution in a muffle furnace preheated to 600°C to initiate the reaction, yielding large amount of gases and forming white voluminous product that was annealed at 800°C for two hours. The theoretical equation used for synthesis of $ZnAl_2O_4$: Eu^{3+} nanophosphors were given below:

$$Zn(NO_3)_2+2Al(NO_3)_3+(NH_2)_2CO \rightarrow ZnAl_2O_4+4N_2+6CO_2+1/2O_2+5H_2O$$

Characterization

The crystal structure and phase composition of the samples were characterized by powder X-ray powder diffraction (XRD) measurements were carried out on a diffractometer Difray 100μ with Cu radiation (λ= 0.15405 nm). The photoluminescence measurements were performed on Avaspect spectrophotometer equipped with a UV lamp as the excitation source. All the measurements were performed at room temperature (RT).

RESULT AND DISCUSSION

Crystal Properties

The crystal structure and phase composition of the samples were characterized by powder X-ray diffraction (XRD) analysis (Figure 2) of prepared samples showed that the samples of both series contain zinc aluminate spinel phase. The samples synthesized via sol-gel method have amorphous structure indicated by XRD peaks broadening with the increase of dopant concentration [7]. However, samples obtained by SC route are featured with higher crystallinity as shown by narrow peaks in XRD spectra, but it contains an admixture of $AlEuO_3$ phase, which content grows with the increase of Eu^{3+} concentration up to 22-mol %. The samples with Eu content higher than 22-mol % are featured with similar XRD profiles with those prepared using SG technique but do not contain the admixture phases.

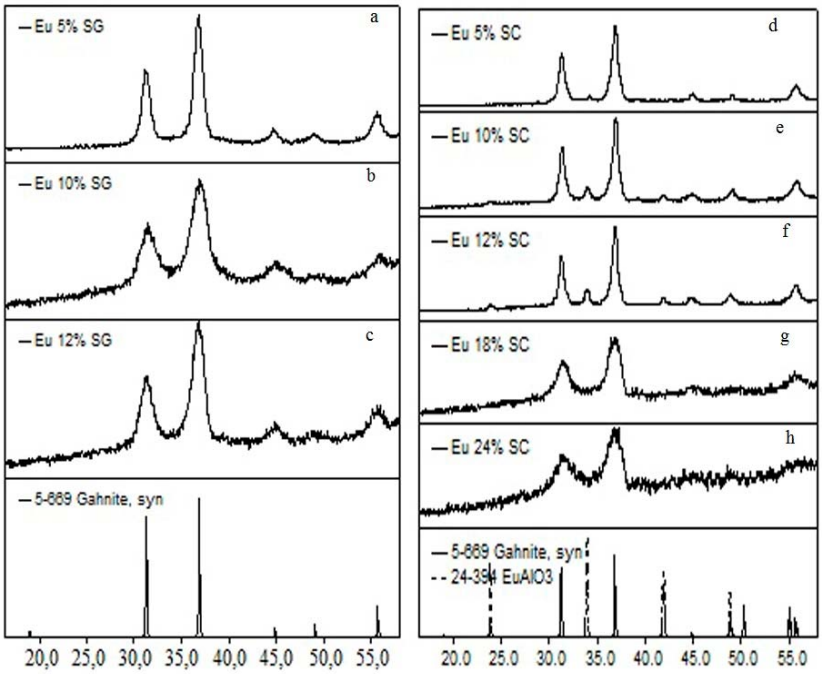

Figure 2. XRD patterns of $ZnAl_2O_4:Eu^{3+}$ phosphor prepared by SG (a, b, c) and SC (d, e, f, g, h).

Table 1. Crystal properties of $ZnAl_2O_4$ phosphors

	Eu 5%	Eu 10%	Eu 12%	Eu 15%	Eu 18%	Eu 24%
SG	12.2 nm	13.3 nm	6,2 nm	6 nm	-	-
SC	9.0 nm	14.9 nm	15,5 nm	15 nm	14,4 nm	6,9 nm

The calculation of the crystallite size according to Scherrer formula from the obtained XRD data [Table 1] indicates that the increase of the dopant concentration results in decrease of crystallite size for samples prepared by SG method, while for samples synthesized using a SC technique an opposite trend is observed and the crystallite size grows with the dopant content [8].

Photoluminescence Properties

The photoluminescence spectra of the studied samples (Figure 3) are found to strongly depend on both Eu^{3+} ions concentration and synthesis method. The luminescence peaks at 612 and 618 nm corresponds to $^5D_0 \rightarrow {}^7F_1$ magnetic dipole transition and $^5D_0 \rightarrow {}^7F_2$ electric dipole transition, respectively. The magnetic dipole transition is permitted for all the considered conditions, while the electric dipole transition highly sensitive to local symmetry is allowed only in the case Eu^{3+} occupies sites free of inversion centers. Subsequently, when Eu^{3+} ions occupy inversion center sites, the $^5D_0 \rightarrow {}^7F_1$ transition should be relatively strong, whereas the $^5D_0 \rightarrow {}^7F_2$ transition should be relatively weak [9]. The samples prepared by SG method are featured with much higher intensity of the peak at $\lambda = 618$ nm compared with that at 612 nm suggesting that Eu^{3+} ions get into sites with low symmetry because this synthetic procedure yields samples with a significantly amorphous structure. On the contrary, for the phosphors obtained using SC technique the intensities of both bands are comparable and the band at $\lambda = 612$ nm becomes narrower with the increase of Eu concentration indicating the improved crystallinity of these samples.

However, the samples prepared using sol-gel method provide a higher luminescence brightness compared with those obtained by SC technique. This is probably determined by the formation of additional $AlEuO_3$ phase in the phosphors prepared by SC synthesis instead of Eu incorporation into the target sites. Nevertheless, the content of this phase decrease with the increase of Eu concentration likely due to a more efficient distribution of Eu in the matrix and decomposition of this undesirable phase.

Brightness Properties

The brightest examples are the samples with concentrations of 12 and 18% received by SG and SC methods, respectively. With increasing concentration, quenching of concentration occurs (Figure 4).

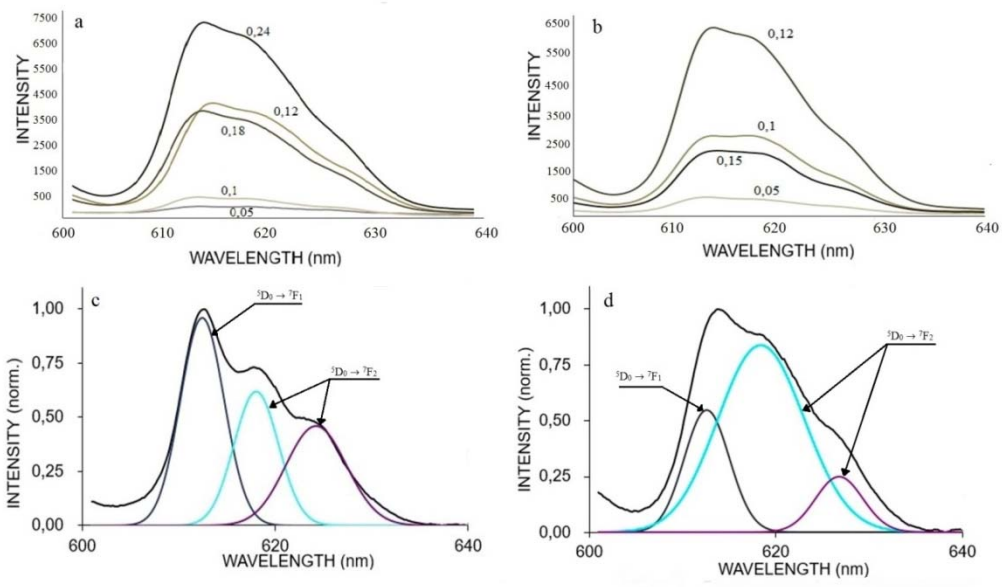

Figure 3. Photoluminescence spectra (a, b) and their deconvolution into separate bands (c, d) for $ZnAl_2O_4$ based phosphors prepared by SC (a, c) and SG (b, d).

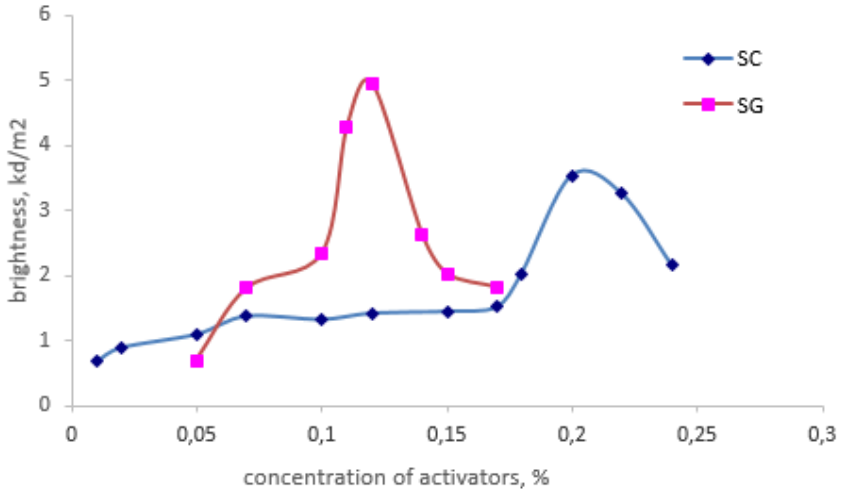

Figure 4. Brightness properties of $ZnAl_2O_4:Eu^{3+}$ phosphors.

To evaluate the material performance on color luminescent emission, CIE chromaticity coordinates were evaluated dopting standard procedures for the system. In general, the color of any light source can be represented as an (x, y) coordinate in this color space. The chromatic coordinates (x, y) can be calculated for the brightest samples as follows:

$$x = \frac{X}{X+Y+Z} \text{ и } y = \frac{Y}{X+Y+Z}$$

The values of x and y coordinates of the system were calculated in Table 2.

Table 2. The value of the chromaticity coordinates

	x	y
SG	0,597	0,344
SC	0,588	0,344

This is pictorially represented in Figure 5 by the points. As evident from the numbers and Figure 5, the CIE index for the phosphor system is very close to the 'Red' line. Thus, it can be inferred that, the particular $ZnAl_2O_4:Eu^{3+}$ phosphor system can be potential 'Red 'emitting phosphor material.

However, the samples obtained SG has more brightness and color purity, than the samples produced SC. This may be due to the formation of impurity phase in the samples synthesized by SC.

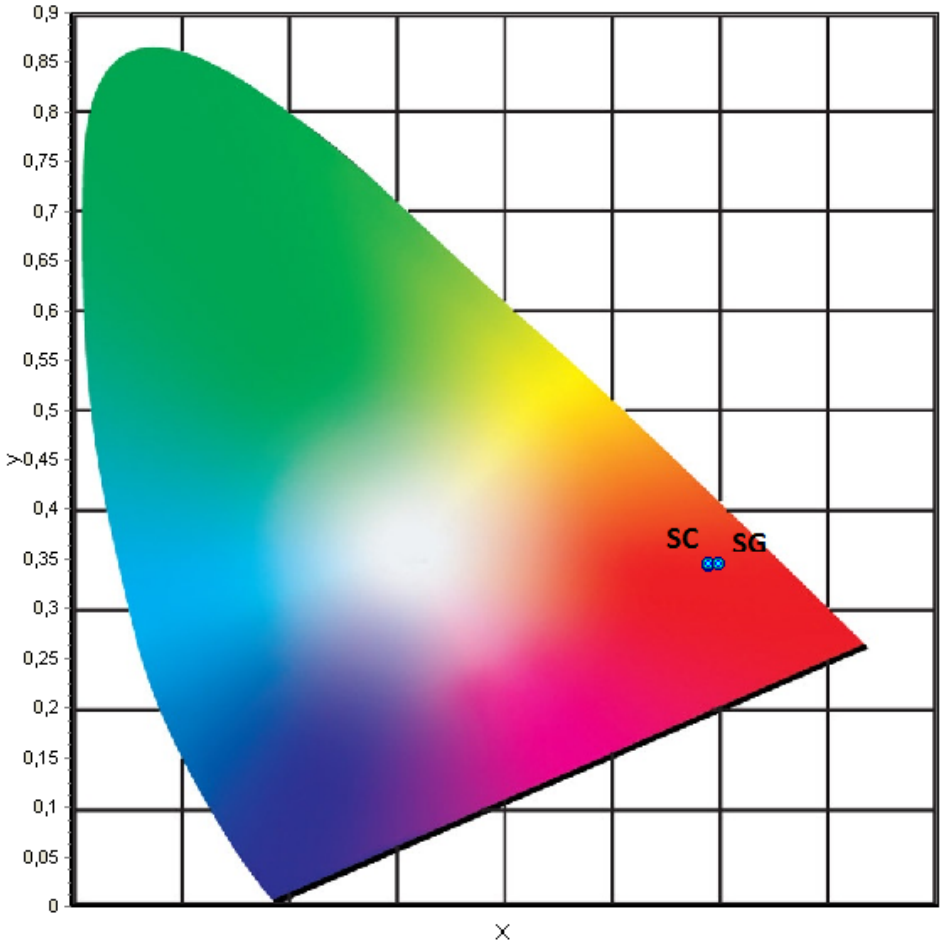

Figure 5. CIE chromaticity diagram for Eu^{3+}-doped $ZnAl_2O_4$ phosphor.

CONCLUSION

Generally, it can be concluded that the synthesis of $ZnAl_2O_4:Eu^{3+}$ phosphors using a solution-combustion method provides samples advantageously featuring with a high crystallinity but containing an admixture phase reducing the luminescence brightness, especially at relatively low Eu contents. The preparation of similar phosphors according to a sol-gel procedure yields samples with more amorphous structure resulting in the decrease of luminance at 612 nm due to the suppression of $^5D_0 \rightarrow {}^7F_1$ electric dipole transition highly sensitive to local symmetry. Thus, the crystallinity, luminescence spectrum profiles and luminescence brightness of the considered phosphors can be effectively adjusted by the variation of both synthetic procedure and dopant (activator) concentration.

ACKNOWLEDGMENTS

This work was supported by Ministry of Education and Science of the Russian Federation (Agreement 14.574.21.0002, identifier RFMEFI57414X0002).

REFERENCES

[1] Chong Peng, Guogang Li, Dongling Geng, Mengmeng Shang, Zhiyao Hou, Jun Lin, *Materials Research Bulletin*, Vol 47, I 11, November 2012, Pages 3592–3599.

[2] Mithlesh Kumar, T. K. Seshagiri n , M. Mohapatra, V. Natarajan, S.V. Godbole, *Journal of Luminescence* 132 (2012) 2810–2816.

[3] Z. Lou, J. Hao, *Appl. Phys. A: Mater. Sci. Proc.* 80 (2005) 151–154.

[4] Mountain Encyclopedia, vol. 5, Moscow, 1991, p. 435.

[5] Xiang Ying Chen, *Chao Ma, Optical Materials* 32 (2010) 415–421.

[6] V. L. Volkov, *Methods for producing nanoscale materials*, 2007, 79.

[7] V.V. Bakhmetyev, L. A. Lebedev, N. S Podsypanina, M. M. Sychov, V. V. Malygin, Effect of Composition and Synthesis Route on Structure and Luminescence of $NaBaPO_4:Eu^{2+}$ and $ZnAl_2O_4:Eu^{3+}$, 2015.

[8] S. V. Motloung, F. B. Dejene, R. E. Kroon, H. C. Swart, O. M. Ntwaeaborwa, *Physica B*, vol 11, I 20, November 2015, pages 468-469.

[9] Fernández-Osorio, C. E. Rivera, J. Chávez*, Proceedings of the World Congress on New Technologies* (NewTech 2015), p-p 360.

Smart Nanocomposites
Volume 7, Number 1
ISSN: 1949-4823

RESEARCH OF THE LASER TREATMENT OF ZINC OXIDE

D. N. Redka*
Saint Petersburg Electrotechnical University "LETI"
Saint Petersburg, Russia

ABSTRACT

Large size (~1,4м^2) silicon-based thin-film solar module (SM) consists of elements connected between each other in a way to get the maximum efficient solar energy conversion in the output. In solar modules production the technological process of separating elements is realized using laser scribing. As a result, the SM area will consist of «active area», where the photoeffect occurs, providing the current constituent part of the converted energy, and «dead zone», which does not participate in photo-electric current generation, but it is a required element for effective separate elements commutation.

The research includes analysis of possibility to decrease the «dead zone» and to increase the parameters of electrical energy output. This can be achieved both by decreasing the width of scribes and by optimizing the commutative connections of SM elements. In terms of precision and quality of manufacture the shape and type of the scribes depend on laser irradiance parameters used in technological process of division of SM into separate elements.

Recently, much work has been done to improve the optical and electrical properties of ZnO films. A comprehensive study of optical (transmittance, scattering) and electrical properties (carrier mobility, carrier concentration, conductivity, resistance) as well as surface topography allows to give recommendations for optimizing the process of obtaining layers with the parameters enabling their use in thin-film solar modules.

Parameters of the conductive layers can be changed by the method of doping with boron zinc oxide films, ion etching and laser annealing.

Keywords: ablation, laser ablation, scribe, transparent conductive thin films of zinc oxide (ZnO), "dead zone," shunting effect, laser beam energy, scribe profile

* dnredka@gmail.com.

INTRODUCTION

Thin-film solar module (TFSM) of large square (~ 1.4 m^2) based on silicon consists of separate elements interconnected in a certain way to ensure the most efficient conversion of solar energy into electrical energy. In the production process TFSM separation into individual components is carried out using laser scribing techniques [1].

This technology is described in detail in [2], where the laser scribing advantages are established and evidence given that use of this method of TFSM switching elements based on a-Si (amorphous silicon) can increase power output of the product by 20% as compared to mask using method [3]. Process flow throughout the manufacturing cycle of TFSM includes several stages of scribing, called Pattern (iterative design template). The aim of our work is to study the possibility of improving the electrical characteristics TFSM by increasing the area not occupied by laser marking. One way of solving this problem is to improve the quality of cuts, in particular in case Pattern1 (P1) - segmentation of the front contact from zinc oxide (ZnO), deposited on glass is performed.

Zinc oxide film is used as a conductive transparent electrodes for current collection of solar cells [9, 10]. They are a good substitute for expensive transparent electrodes on the basis of ITO (Indium tin oxide). Zinc oxide has electronic conductivity due to the large number of intrinsic defects such as interstitial zinc or oxygen vacancies [11]. If you produce ZnO films with a certain morphology of the structure, they are able to act as a light diffuser. When passing through a layer of this material solar radiation quantum changes its trajectory, so dispersion of radiation occurs, this leads to an increase in the optical path of the particle in the photoactive structure. Thereby conversion of solar energy becomes more convenient and short circuit current increases (Figure 1).

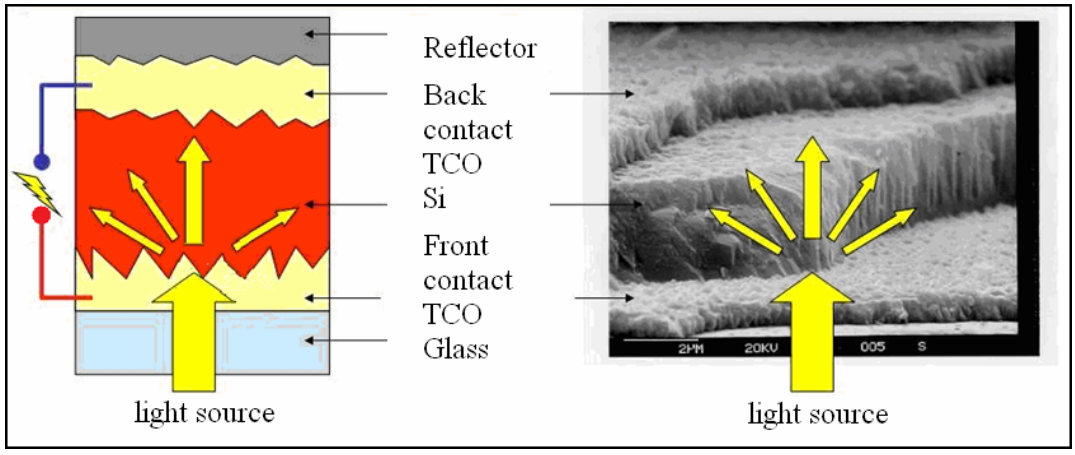

Figure 1. The diffusion of light on ZnO.

The degree of dispersion (Haze-factor) determines the amount of the scattered light relative to the light transmitted through the TCO layer:

$$Haze(\lambda) = \frac{T_{diff}(\lambda)}{T_{full}(\lambda)} \cdot 100\%$$

ZnO main characteristics are presented in Table 1. The main requirements to the transparent electrodes are high optical transparency T ≥ 93% in the range 400-1100 nm, electric conductivity Rsqr <10 Ohm • square and good throwing power (at 600 nm ≈ 25%).

Recently, much work has been done to improve the optical and electrical properties of ZnO films. In this paper we investigate the effect of laser annealing on the electrical and optical properties of ZnO films, obtained by plasma-chemical vapor deposition under low pressure (LPCVD).

Table 1. ZnO main characteristics

	Bandgap (eV)	Conductivity ($S\ cm^{-1}$)	Electron concentration (cm^{-3})	Mobility ($cm^2V^{-1}c^{-1}$)
ZnO	3.35	8000	> 1021	20

MATERIALS AND METHODS

The glass film with deposited thereon zinc oxide was used as an experimental sample. Processing of the sample was performed by laser radiation with a wavelength of 355 nm, the laser pulse energy ranged from 14 mJ to 21 mJ (± 0.05 mJ). There were seven groups for different cuts of focus distance that vary in increments in 0.1 mm. Each group included five consecutive scribes obtained with the power of laser pulses of 14 mJ, 16 mJ, 18 mJ, 20 mJ, 21 mJ, respectively. Pulse repetition rate was 60 kHz and a pulse duration was 30 ns.

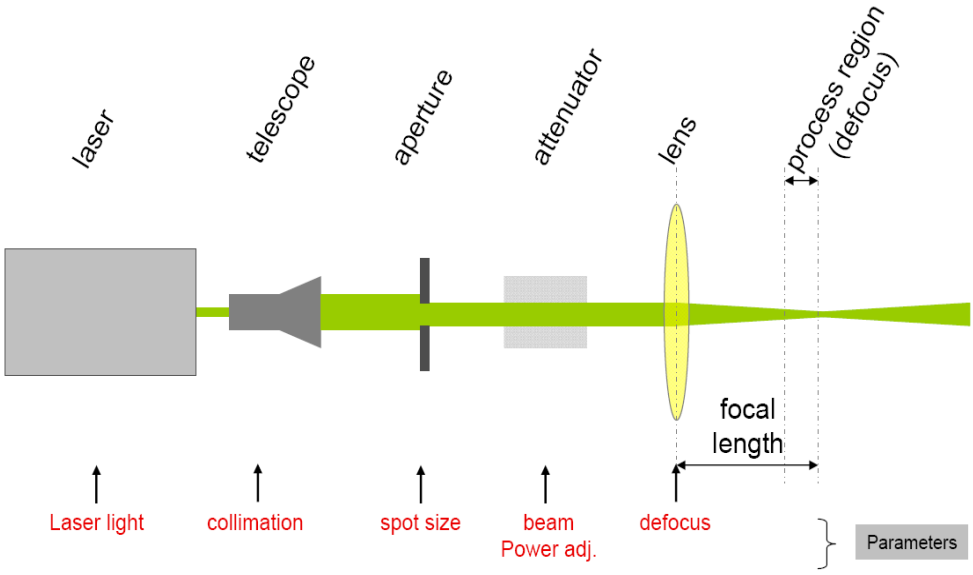

Figure 2. The experimental scheme.

The intensity of the laser pulse has a shape close to a Gaussian distribution with a maximum at the center of focus of the beam. Data matrix was obtained during the experiment. Scribe control was performed using optical microscopy. Photographing of groups

of scribes was conducted in different coordinates of the sample. There was detected scribe, which has the following characteristics: a minimum width on the surface of 27 ± 0,5 μm scribe, scribe at the bottom (on the side of the glass substrate), the width is 25 ± 0,5 μm; width of cut on the surface and at the bottom is constant in different coordinates of the cutting length; minimum number of chips and no shunt elements. This scribe was obtained by defocusing value (the distance from the focus to the treated surface) of the laser beam by 1.5 mm and a laser pulse energy of 20 mJ. When passing by through the glass beam was focused to the treated layer ZnO.

APPARATUS

Experiment of laser-annealed film of zinc oxide ZnO was conducted at the setup Laser Scribing System LSS1200 by Oerlikon® (TEL Solar®). The sample is a glass substrate size 1300 × 1100 mm^2 coated with a layer of zinc oxide ZnO. Preliminary study of the sample parameters (such as thickness in different areas, surface resistance, transmittance and Haze-factor) was conducted by using a spectrophotometer Carry 5000. The areas of the sample for laser annealing were selected so that the average thickness of the material was 1700 ± 20 nm.

These samples were examined by optical (Nikon Eclipse LV100D), atomic force microscopy (Nanoman V) and Raman spectroscopy (LabRam HR800).

RESULTS AND DISCUSSION

During the experiments it was found that at low energies of the laser pulse (less than 3 mJ) it is impossible to obtain uninterrupted scribe, as a result there are shunts because is not enough energy to remove material by laser ablation. The value of the width of the resulting "track" is an important factor. Increasing the width of cut reduces the active area of the solar module, as a consequence, the decrease of the photocurrent values of the solar module (photocurrent depends on the "active area" involved in the generation of charge carriers) [1]. At this stage, the problem is the need to reduce the area of "dead zone."

One way to reduce the area of "dead zone" is to reduce the width of the scribe. In [5, 6, 7] scribe P1 width is more than 40 microns. For a given scribe width the "dead zone" increases, which is undesirable. In [8] width scribe is 25-27 microns, the measurement has been carried out in a single coordinate system, in the area of the module, where the thickness of the front contact does not differ. In case of measuring the width scribe in other areas, where the thickness of ZnO may take other values, the width scribe will vary.

The power of the laser radiation used in the processing has a direct influence on the cutting depth (scribe). Scribe depth determined by the equation:

$$h \approx Pt / \left(\pi r_0^2 L_u \right) \tag{1}$$

where P-power of laser beam, t- duration of the laser pulse, r_0 - the radius of the laser spot on the surface to be treated, L_u - hide heat of vaporization.

Laser spot size will also affect the width scribe. The dependence of the width of the scribe on the laser spot size is described by equation:

$$l \approx 2\left(r_0 + P\mathrm{tg}\gamma / \pi r_0 L_u\right) \tag{2}$$

If using equation (1) we determine r_0 and put the value obtained in the equation 2, we obtain the following relation:

$$l \approx 2(\sqrt{Pt / h\,\pi L_u} + P\mathrm{tg}\gamma / \pi r_0 L_u) \tag{3}$$

where l - scribe width - half angle of the focused beam impinges on the sample, h- thickness of ZnO layer in place of the laser beam, γ - angle incidence of the beam.

Knowing what values of laser power remove the needed material, scribe depth can be correlated with the film thickness. Thus, the equation (3) determines scribe width dependent on the following variable parameters of the laser radiation: P and t. In this paper, the laser pulse duration t remained constant, only the focal length of the optical system and the power of the laser beam changed.

It should be noted that the scribe widths are also effected by the unevenness of thickness of the substrate (glass). Film ZnO that is processed is deposited directly on the glass. When processing laser beam must be focused on the film itself. When scanning the surface with a laser beam because of the uneven thickness of the glass, the film may periodically fall in defocus area therefore the size of the laser beam in the treated area will vary. When the film is in focus the laser beam, spot size is minimum. However, the treatment by focused beam scribe brings more melts and spray the material at the edges. These defects afterwards, with high probability, may become shunt elements that will increase the number of defective SM at this stage of production. The appearance of melts using the laser beam of the minimum radius can be explained by the fact that as a result of focusing of the laser beam at the processing spot film of the beam power density per unit area (W/m^2) increases sharply. These adverse effects can be avoided, on the one hand, by reducing the power laser with an attenuator to energy levels that do not appear melting ZnO. However, this option is not acceptable in view of the fact that the treatment area where it is necessary to ensure the minimum radius of the laser beam oscillates strongly due to variations in thickness of the glass. This in turn leads to oscillation of the beam power density per unit area. This means that the processing with focused on the film the laser beam quality ZnO scribing occurs only at a fixed thickness over the entire area of the glass but, as the glass has a non-uniform thickness (±0,06 mm), a laser beam is at different moments focused either in the glass or above film ZnO. As a result, for a given processing mode we obtain unsatisfactory results of treatment, since it does not provide the required level of the laser power, sufficient for removing the material. Based on the foregoing, it is expedient to proceed in the region where the oscillation power of the laser beam per unit area (W/m2) is minimal. This area is the defocusing area where r_0 is more than the minimum. Switching to defocusing provides better and more uniform treatment, but automatically leads to an increase in the width of the scribe l.

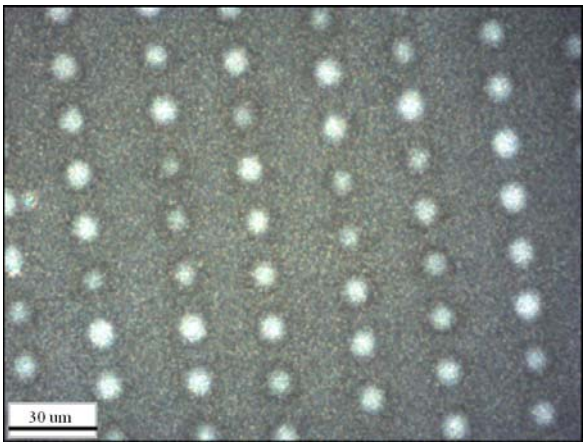

Figure 3. Annealed sample surface image obtained by an optical microscope Nikon Eclipse LV100, P = 0.201 W/cm2 (the distance between the points is around 30 microns).

The best results for laser treatment have been achieved by annealing the films of zinc oxide ZnO with a laser beam at power density ranging 0.163 ÷ 0.260 W/cm^2. Laser radiation with the power density less than 0.163 W/cm^2 causes almost no change, and when the power density was over 0.260 W/cm^2, sections with significant areas of melting and cracking of the film were obtained, which is a negative factor in the production of thin film solar modules. Moreover it should be noted here that due to the energy distribution in the laser beam Gaussian surface annealed films unevenly and a large enough portion of the film was hardly processed (Figure 3).

After the first step of laser annealing was performed, areas listed in Figure 3 were studied using a spectrophotometer. The results are shown in Table 2. For further study sample was cut into samples measuring 1.5 × 1.5 cm^2.

Table 2. Results of the first step of laser annealing

№	P, mW	X mm	Y mm	d, nm	H, %	r, Omh/sq	T, %	R, %
1	93	650	550	1685.483	29.09	11.351	78.1095	3.5107
2	115	559.57	626.14	1683.746	29.43	11.101	78.1231	3.4669
3	136	559.57	473.86	1696.019	29.79	11.019	77.9709	3.4025
4	163	559.57	321.57	1678.137	27.29	12.813	78.551	3.6832
5	192	378.71	473.86	1697.838	30.23	10.454	77.6962	3.2258
6	221	740.43	169.29	1699.518	24.08	14.147	79.148	3.8722
7	253	740.43	321.57	1707.21	28.2	12.234	78.3283	3.3454
8	287	740.43	626.14	1706.202	30.66	10.904	77.6934	3.0879
9	324	740.43	778.43	1686.05	30.55	13.564	77.3872	3.0889
10	364	1102.143	169.29	1877.535	32.83	22.239	73.9872	2.4377
11	405	1102.143	321.57	1701.538	37.34	31.105	73.8088	2.9263
12	445	1283	169.29	3500	2.87	140.632996	89.1787	7.6261

In the second phase of the experiment a laser annealing was carried out in the range of power densities of 0.163 ÷ 0.260 W/cm^2, and the following results were obtained:

- when exposed to a laser beam with a power density of 0.127 W/cm^2 the transmittance of the ZnO film increases by 0.216%;
- a value of the power density of 0.188 W/cm^2 leads to reduction of the surface resistance by 6.749%;
- a value of the power density of 0,201 W/cm^2 leads to increase of the Haze-factor by 2.61%, and leads to reflection reduction from the surface of the film by 12.85%.

The correlation of the film properties with laser power is shown in Figure 4-7.

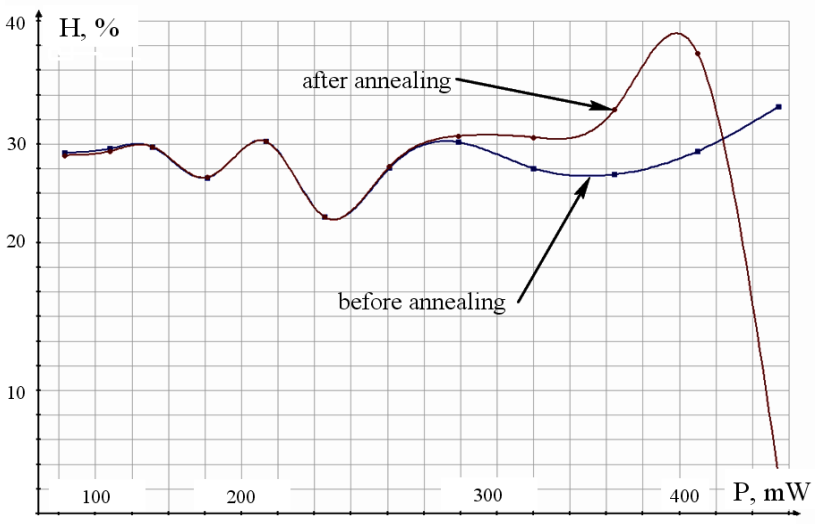

Figure 4. Haze-factor correlation with radiation power in the laser annealing.

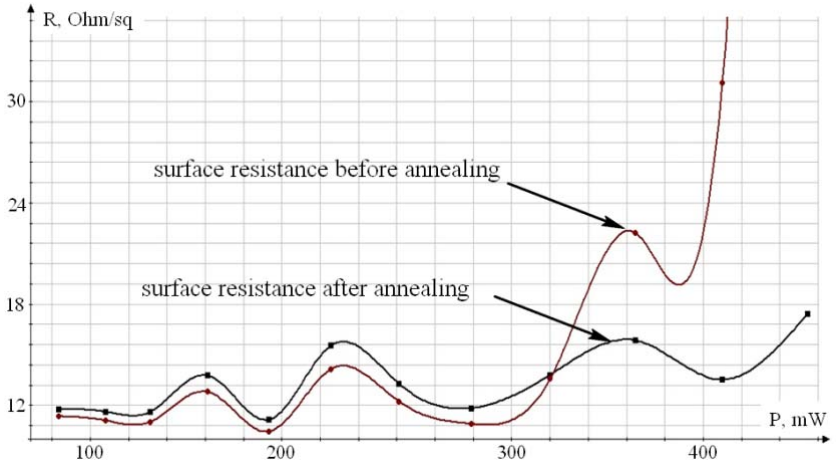

Figure 5. The correlation of surface resistance with radiation power in the laser annealing.

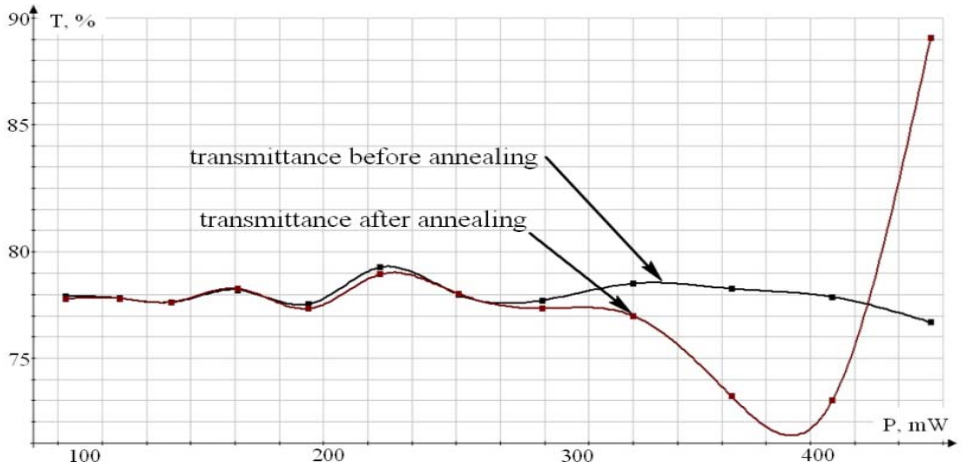

Figure 6. The correlation of transmission coefficient with radiation power in the laser annealing.

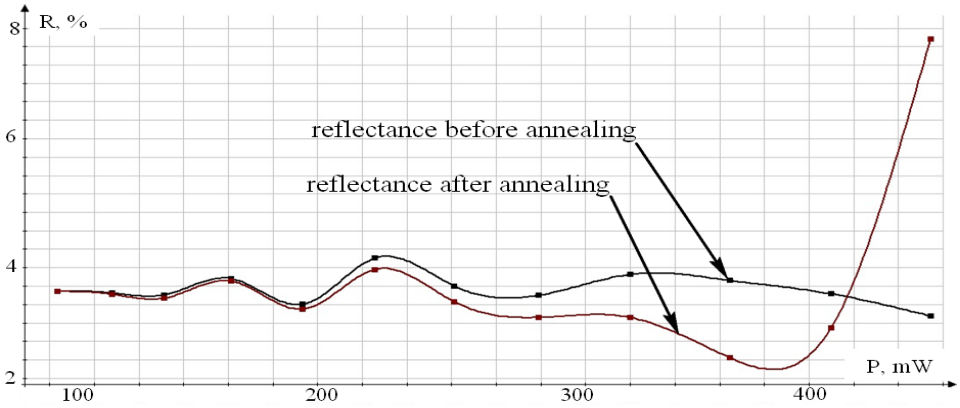

Figure 7. The correlation of reflectance with radiation power in the laser annealing.

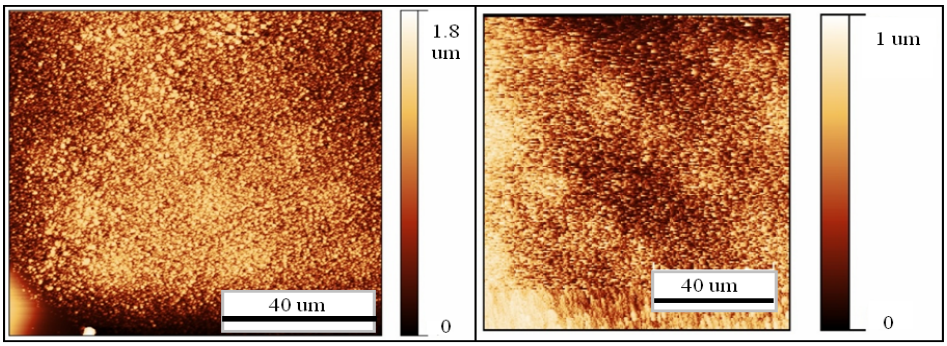

Figure 8. The image surfaces of the samples number 11 (left) and 12 (right) obtained by an atomic force microscope.

Study of the sample's micro relief was conducted using atomic force microscope Ntegra Therma (NT-MDT). The results are shown in Figure 8, 9. It is revealed that with an increase in power incident on the sample the surface roughness increases and this leads to an increase

in Haze-factor (samples № 7-11). With further increase in capacity the size of irregularities decreases (sample № 12) and the diffusion of radiation reduces.

To investigate the influence of changes in electrical and optical properties of ZnO films on the output characteristics of the solar module, original sample was divided into mini-module sizes 40 × 50 mm^2. Also mini-modules were produced without annealing to compare their output parameters of mini-modules with front TCO layer processed. Average values of output parameters for each of the samples are presented in Table 3.

Despite the fact that the effect of laser annealing on parameters of ZnO films changes were found in electrical and optical properties during the study of the influence of these parameters on the output characteristics, no noticeable effect of changes was found regarding the properties of ZnO films on the output characteristics of the modules. This may be caused by the fact that annealing of the film is fairly irregular around the area as a result of the power distribution in the Gaussian beam (Figure 3).

Further work was aimed to implement a laser annealing ZnO with a more regular radiation intensity distribution on the cross beam section, as well as to investigate possible structural changes of the material during annealing not only on the surface but also in depth.

The films were treated by radiation with a wavelength of 355 nm. The structure of the films was examined by Raman spectroscopy (Figure 9). To study the vibrational properties of ZnO crystal lattice the Raman spectroscopy was used. Raman spectra were recorded in the reverse scatter geometry at room temperature with a spectrometer LabRam HR800, combined with a confocal microscope (manufactured by Jobin-Yvon Horiba). As the excitation source was used second harmonic of Nd: YAG-laser (wavelength 532 nm). The laser beam is focused to a spot with a diameter of ~ 1-2 μm on the sample surface.

In the hexagonal symmetrical structures C46v, such as ZnO, there are six branches of optical phonons at Γ (the center of the Brillouin zone) Γ = A1 + E1 + 2B1 + 2E2 [12-15]. Phonon modes of symmetry A1 and E1 are polar at the point Γ and split into longitudinal and transverse optical vibrations (LO and TO, respectively). Non-polar phonon modes symmetry E2 shares two frequencies: E2(high) related to the vibrations of the atoms of oxygen and E2(low) related to the vibrations of the atoms of zinc. [16] Mode B1 is «silent mode» and does not appear in the optical spectra of [15, 17].

Fig. 9 shows Raman spectra of a polycrystalline ZnO film prior to (curve 1) and after (curve 2) laser modification. Considering Fig. 9 it may be noted that in the spectrum of ZnO samples before modification there are narrow lines typical for crystalline phase of ZnO: E2low intense line with the position of the maximum of ~ 98.5 cm^{-1}; a broad band of weak intensity E2(high)–E2(low) refers to the scattering involving several phonons; E2(high) to the maximum position ~ 438 cm^{-1} and A1 (LO) ~ 580 cm^{-1}. Wide band with a maximum near 195 cm^{-1} and 420 cm^{-1} can be attributed to fluctuations in the second-order modes E2 [18-22]. Also, the spectrum contains broad bands associated with phonon density of states of ZnO amorphous, in the range from 300 cm^{-1} to 600 cm^{-1}. Thus, the original film is polycrystalline ZnO. The spectra obtained from the edges of the spot were also examined for the characteristic lines of the crystalline ZnO, but band intensity A1 (LO) significantly increased which may indicate that disordering of the crystal lattice and an increase in structural defects [23]. The Raman spectrum obtained from the center of the spot (line 2) is the phonon density of states of the crystalline ZnO, shows that is a highly disordered structure.

Table 3. Average values of output parameters for minimodules

№	W, мВт	P,Вт/см 2	Voc [V]	Isc [mA]	Jsc [mA/cm²]	FF [%]	Eta [%]	Rs [Ω]	Rp [kΩ]	Vmpp [V]	Impp [mA]	Pmpp [mW]
1(2)	0.88	0.125	1.27	9.94	9.94	72.04	9.12	14.13	7.58	1.02	8.98	9.13
2(8)	0.131	0.185	1.27	9.55	9.55	72.51	8.8	14.99	185.88	1.01	8.69	8.81
3(9)	0.139	0.197	1.25	9.81	9.81	70.87	8.69	14.9	12.67	0.99	8.8	8.69
1'(0)	0.00	0	1.29	10.02	10.02	72	9.31	13.92	8.96	1.03	9.03	9.31

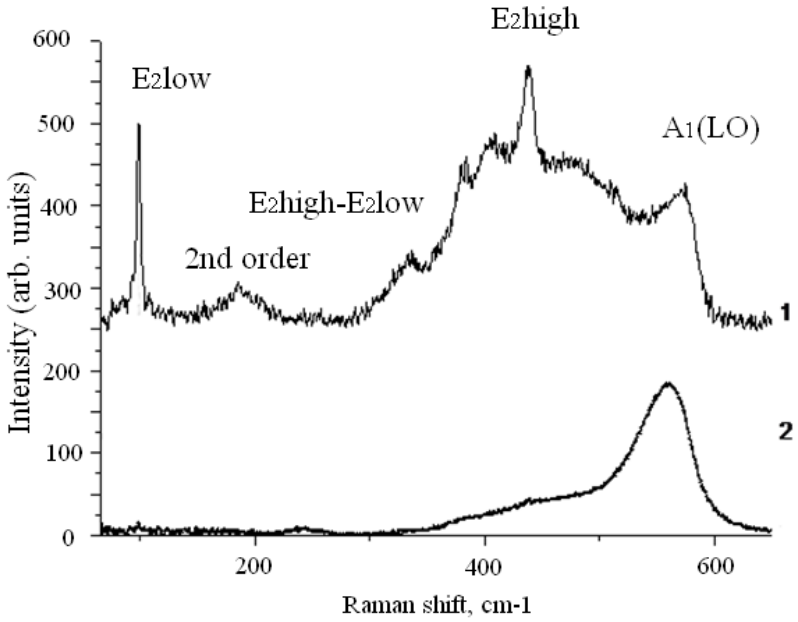

Figure 9. The Raman spectra of the film ZnO: 1 - before modification; 2 - after modification.

CONCLUSION

Processing with of optimum focus settings allows to obtain correct geometrical form of cuts, the width of which is almost independent on the ZnO film thickness unevenness (in the case cutting width variations differ in less than 0.5 microns), with a minimum number of chips and absence of the shunt elements. Implementation of the results achieved in the TFSM production technology will increase the output current about 2-5% by reducing the area of laser micromachining (compared with typical TFSM produced by this technology).

Summing up the results of the analysis, it can be concluded that the polycrystalline ZnO structure is destroyed by modifying laser radiation, while in the center of the spot amorphous zinc oxide is formed. The results can be used to create thin-film solar modules of a large size.

ACKNOWLEDGMENT

The study was supported by the grant of Russian Science Foundation (project № 14-12-00327).

REFERENCES

[1] Shah Arvind. Thin-film silicon solar cells. Lausanne: EPFL Press, 2010.S. 331-336.

[2] Kuwano Y. et al.: Amorphous Silicon Integrated Cell Modules (I)/1st Photovoltaic Sci. & Engg. Conf. in Japan, (1979) 55.

[3] Kiyama S., Matsuoka T., Hirono Y.et al. Laser Patterning of Integrated-type a-Si Solar Cell Submodules/*Journal of the Japan Society for Precision Engineering*. 1990. № 11, PAGE.2069-2074.

[4] Haas S., Ku V., SchopeG.et al. Patterning of thin-film silicon modules using laser with tailored beam shapes and different wavelengths/23th European Photovoltaic Solar Energy Conference Valencia, Spain, 2008. Pages 2383-2387.

[5] Schoonderbeek A., Schuts V., Haupt Oliver, and Stute U .. Laser Processing of Thin Films for Photovoltaic Applications//JLMN Vol. 5, No.3, 2010.Pages 248-254.

[6] Buzas A., Geretovsky Zs., NemethA. et al. Selective cutting of ZnO: Al contact layers/24th European Photovoltaic *Solar Energy Conference*. 2009 Pages 3004-3006.

[7] Canteil D., Fernandez S., Molpeceres C. et al. Nanosecond laser ablation processes in aluminum-doped zinc-oxide for photovoltaic devices/*Applied Surface Science*15 September 2012, Pages 9447–9451.

[8] Booth H. Laser Processing in Industrial Solar Module Manufacturing//*JLMN* Vol. 5, No. 3, 2010.

[9] V. P. Afanasiev, E.I. Terukov, A.A. Sherchenkov, Thin-films solar cells based on silicon. 2nd ed. SPb .: Publishing House of the ETU "LETI," 2011. 168 pp.

[10] Fan Yang, Large Area a-Si/μc-Si *Thin Film Solar Cells, Solar Sells thin-film technologies,* 2011, pp. 335-359.

[11] Zhang, SB; Wei, S-H; Zunger, Alex; ,Intrinsic n-type versus p-type doping asymmetry and the defect physics of ZnO,*Physical Review B,*63, 7, 075205, 2001, APS.

[12] Singh, S., Srinivasa, R. S., & Major, S. S. (2007). Effect of substrate temperature on the structure and optical properties of ZnO thin films deposited by reactive rf magnetron sputtering. *Thin Solid Films*, 515, 8718–8722.

[13] Song D, Effects of rf power on surface-morphological, structural and electrical properties of aluminium doped zinc oxide films by magnetron sputtering *Appl. Surface Sci.,* 254, 4171 (2008).

[14] H. Morkoëc, ËU. ËOzgËur, Zinc Oxide, Fundamentals,Materials and Device Technology (Wiley VCH, Verlag GmbH & Co. KGaA, 2009).

[15] C. Charpentier, P. Prod'homme, I. Maurin, M. Chaigneau and P. Roca i Cabarrocas, X-Ray diffraction and Raman spectroscopy for a better understanding of ZnO:Al growth process, *EPJ Photovoltaics 2*, 25002 (2011).

[16] Khan A. Alim, Vladimir A. Fonoberov, Manu Shamsa, and Alexander A. Balandin, Micro-Raman Investigation of Optical Phonons in ZnO Nanocrystals. *J. Appl. Phys*. 97, 124313 (2005).

[17] V. V. Strelchuk, E.A. Avramenko, A.S. Romaniuk, L.V. Zavyalov, G.S. Svechnikov, V. S. Khomchenko, N.N. Roshchin, V.N. Tkach. Structural and optical properties of ZnO films, prepared without vacuum chemical method, *Semiconductors,* 2014, Volume 48, no. 9, pp.1176-1181.

[18] Umar, S.H. Kim, Y.–.S. Lee, K.S. Nahm, Y.B. Hahn, Catalyst-free large-quantity synthesis of ZnO nanorods by a vapor–solid growth mechanism: Structural and optical properties, *J. Cryst. Growth* 282, pp. 131-136, (2005).

[19] Chih-Hung Hsu, Lung-Chien Chen and Xiuyu Zhang. Effect of the Cu Source on Optical Properties of CuZnO Films Deposited by Ultrasonic Spraying, *Materials* 2014, 7(2), pp.1261-1270.

[20] T. C. Damen,; S. P. S. Porto, & B. Tell, Raman Effect in Zinc Oxide, *Phys. Rev*. 1996, 142, pp. 570–574.

[21] M. Tzolov, U.N. Tzenov, D. Dimova-Malinovska, M. Kalitzova, C. Pizzuto, G. Vitali, G. Zollo, I. Ivanov, Vibrational properties and structure of undoped and Al-doped ZnO films deposited by RF magnetron sputtering, *Thin Solid Films 2000*, 379, pp. 28–36.

[22] V. A. Nikitenko, V. G. Plekhanov, S.V. Mukhin, M.V. Tkachev, Raman spectra of oxide zinc powders and single crystals, *Journal of Applied Spectroscopy*, Volume 63, Issue 2, pp.290-292.

[23] Mahmoud Zolfaghari, Hamdallah Puladiana, Forogh Abazaria. Raman Study of Mn-doped ZnO nanoparticle, *Proceedings of the 4th International Conference on Nanostructures (ICNS4)* 12-14 March, 2012, Kish Island, I. R. Iran. pp.396-397.

Smart Nanocomposites
Volume 7, Number 1
ISSN: 1949-4823

STRUCTURAL TRANSFORMATIONS IN IRON THIN FILMS ON A SILICON SUBSTRATE

S. N. Saltykov[1,*] and A. M. Khoviv[2]
[1]Lipetsk State Technical University (LSTU), Russia
[2]Voronezh State University (VSU), Russia

ABSTRACT

During annealing of iron films (20-270 nm) on silicon substrate phase-formation process consists of two stages. Under temperature less than 130^0C the increasing of iron lattice parameter from 2.8663 (traditional bcc lattice) A up to 2.8737 A is observed and solid solution Fe(Si) is formed. The width of transition region (Fe/Si) is increasing up to 30 nm. Under temperature 180^0C the phase Fe_5Si_3 which is an ordered solid solution and which exists under 800^0C only is formed and stabilized in thin film state. The forming of Fe(Si)-phase is initiated by polygonization process of iron structure. Recrystallization process of iron structure is observed only at film thickness more than 100 nm.

Keywords: iron film, structural transformation, polygonization, recrystallization

INTRODUCTION

Thin-film metallic materials are unique objects that have broad application prospects in various fields of modern science and technology due to their unique physical and chemical properties. A great amount of papers [1-6] are devoted to the study of the structure and properties of iron thin films. This is due to the fact that the iron film is an individual object that has a wide application in microelectronics. In this aspect, the various properties of the films are important, depending on the phase composition of the film and its structure. Additionally, dual- and multicomponent iron-based films are of special interest. Thus, the Fe-Cu system in the bulk state is quite simple thermodynamically, but becomes ever more relevant in the form of thin films as the object of research, which is due to several reasons. In two- and multilayer Fe-Cu films, the giant magnetoresistance effect is discovered [7, 8], which is fundamental for the operation of magnetic recording devices (i). According to [9,10], in thin Fe-Cu films, Hall and Kondo effects occur, which stipulate the application of such films in sensors for electric and magnetic fields (ii). Areas (i) and (ii) have been researched

* saltsn@mail.ru.

for quite a long time. However, another area of studying Fe-Cu is relatively new and is related to the search for ways of improving corrosion and mechanical properties of steel (iii). The addition of copper to low-carbonaceous steel instead of the triad of expensive alloying elements (Nb, Ti, V) with subsequent heat treatment leads to improved mechanical and corrosion characteristics [11, 12]. The reason for this is nanoscale precipitates [11] – particles of a saturated solid solution of copper in iron with the copper concentration of more than 1%, which is significantly higher than in the equilibrium "bulk" state (0.38%). The first reports about the possibility of forming Fe(Cu) solid solution with high copper concentrations are presented in [13], and a number of papers have been devoted to the study of its composition and structure. However, the conditions for the formation of Fe(Cu) precipitates are still poorly studied. When a thin layer containing Fe(Cu) precipitates is formed on the steel surface, it is particularly interesting in the applied aspect. In surface alloying, the most important step is heat treatment leading to the formation of the required structure of the material, and on the basis of [13-16] it can be expected that the structure and phase composition of the surface layer play an important role in Fe(Cu) precipitates formation mechanism. Thus, we regard as relevant the systematic study of the structure and composition of iron, copper, double-layer Fe-Cu films, as well as the interconnection between the transformations of film structure and their phase composition. It is a multi-step research, the first stage of which is to study the structure of iron thin films and the effect of temperature on its transformations and phase composition. A huge amount of papers are devoted to the research of iron film structures studying the formation of iron films on various substrates. The purpose of this paper is to explore the possibilities and conditions for the formation of nanoscale Fe(Cu) precipitates in thin-film systems. The formation of thin films involves the use of substrates of specific chemical nature and structure having a significant impact on the composition and structure of the film. Considering the key element of modern microelectronics to be silicon, it is advisable to use a silicon substrate. This will make it possible to significantly extend the application scope of the obtained results to areas (i) and (ii) without being confined to surface alloying of steel.

Several studies have shown that during the first stage of the film formation iron has a fcc lattice, which in its bulk state exists only at temperatures above 911^0C in the γ-Fe form [1,2]. The authors of [11] proved the existence of a "critical" thickness of the film (about 1.5 nm), the value of which corresponds to the $\gamma \rightarrow \alpha$ phase transition with the fcc→bcc lattice transformation and the change of the lattice parameter. However, according to [17], the "critical" thickness of an iron film is significantly higher (10 nm). The stabilization of the γ-Fe phase is determined by the cooling rate and the temperature of the substrate [17]. In [18] it is shown that the iron film has crystals of the δ-Fe phase which in its bulk state exists only at the temperature above 1400^0C. The stabilization of γ-Fe and δ-Fe phases in an iron film depends on the crystallographic orientation of the silicon substrate [18].

In [3-5] the surface morphology of iron films was researched. The authors [3,4] showed that in the interval of thickness between 6 and 350 nm, the film structure contains clusters of non-isometric rounded shape and single "crystal-like" formations. Thus, a linear dependence of the cluster size on the film thickness is found [4,5], with the threshold thickness value of 40 nm [3] or 30 nm [4]. When the film thickness is more than 100 nm [3], the cluster size becomes constant and independent of thickness.

A significant feature of using the silicon substrate for iron films is the possibility of forming iron silicide as a part of the film. Typically, the silicon surface is covered by a natural

oxide layer. The opinions of various authors about the possibility of iron and silicon diffusion through the silicon oxide layer diverge significantly. In accordance with [6,19], iron atoms can diffuse through the silicon oxide layer to form a solid solution. In contrast, the authors [20] showed that at room temperature the silicon oxide layer is a single crystal barrier for iron atoms. The diffusion of atoms occurs only at elevated temperatures over defects of silicon oxide. A similar result was obtained in [21], where the possibility is shown of mutual diffusion of silicon and iron only under heat. With regard to the products of the silicide forming process in an iron film, the results obtained by different authors are extraordinarily diverse. In an iron film the formation of the FeSi [22], Fe_5Si_3 [23], γ-$FeSi_2$ [24], α-$FeSi_2$ [22], β-FeSi2 [25] phases was observed. Significantly different also are views on the film thickness at which iron silicide begins to form. According to [24, 22], the interaction between iron and silicon begins at a film thickness of a few monolayers when a solid solution is formed [23]. When the temperature is changing, the mutual conversion of iron silicide phases occurs [26].

A large number of papers are devoted to the study of electrical and magnetic properties of iron films. In [3] it is shown that there are three thickness ranges in which conductivity varies differently. When the thickness is less than 40 nm, the film conductivity is constant, with the thickness range between 40 and 70 nm a sharp increase of conductivity is observed, while at the thickness of more than 70 nm, the electrical conductivity is linearly dependent on the thickness. However, the data obtained by the authors [3] is associated only with the transfer from an island film to a continuous film through coalescence. In [4] the electron free path in the film depending on the thickness was estimated.

Thus, a lot of various data on the phase composition of iron films, products of silicidation, changes in the surface morphology and the structure of iron films when heated is presented in research literature. However, the mechanism of the formation of each phase is associated mainly with the formation of a specific Fe/Si interface, in which the mixing process develops at the atomic level [22, 27, 28]. The intensity of this process significantly depends on the temperature. On the other hand, it is known that the heating of the metal material is always accompanied by structural changes such as the “structure recovery” (annihilation of point defects), polygonization (emergence of new borders due to the movement of dislocations) and recrystallization (nucleation of new grains). Moreover, each of these transformations is implemented in a certain temperature range. Accordingly, when explaining the phase composition of films, it is necessary to take into account possible transformations of the structure and their potential impact on the mechanism of the phase formation process. However, with respect to thin films, transformation processes are understudied, and there is practically no data on their effects on the phase formation process in iron films.

EXPERIMENTAL

Iron films were obtained on a single crystal silicon substrate (100) by magnetron sputtering (with the voltage of 500 V, the discharge current of 0.5 A). The content of impurity atoms in the target is not more than 0.01 at %. The film structure was studied by scanning electron microscopy (device JSM-6380LV, EDX) and atomic force microscopy (device Solver P47Pro). In some experiments, before atomic force studies, short-term chemical etching of the film surface in nitric acid ethylene solution was used. Changes of the film

structure during heating and cooling, were studied in-situ by high-temperature X-ray diffraction (device ARL X'TRA, λCu = 1,5405Å, Bragg-Brentano geometry, thermal vacuum chamber NTK-1200N, database ICDD-2007). The estimation of the average size of the film's coherent area reflection was based on the Scherrer ratio, and the determination of the lattice parameter distortion was based on the Vegard ratio. In order to obtain concentration depth profiles of chemical elements, the method of Rutherford backscattering was used. The dependencies of film resistivity on temperature were measured by the four-probe standard method. All temperature measurements (XRD, film resistivity) were carried out in the temperature range from the room one to up to 500^0C.

Table 1. Characteristics of iron films

№	h, nm	$2\Theta_{(110)}$,^{0}	d_{110}, Å	d_{table}, nm	Δ,^{0}	d, nm	D, nm
1	24	44.66	2.0283	2.0268	0.88	9.8	41.7
2	45	44.65	2.0288		0.56	15.3	48.7
3	62	44.67	2.0279		0.50	17.2	65,0
4	100	44.67	2.0279		0.51	16.8	82,0
5	150	44.66	2.0284		0.46	18.7	98.3
6	173	44.66	2.0284		0.50	17.2	92.7
7	208	44.66	2.0284		0.47	18.1	78,0
8	270	44.66	2.0284		0.52	16.5	70,0

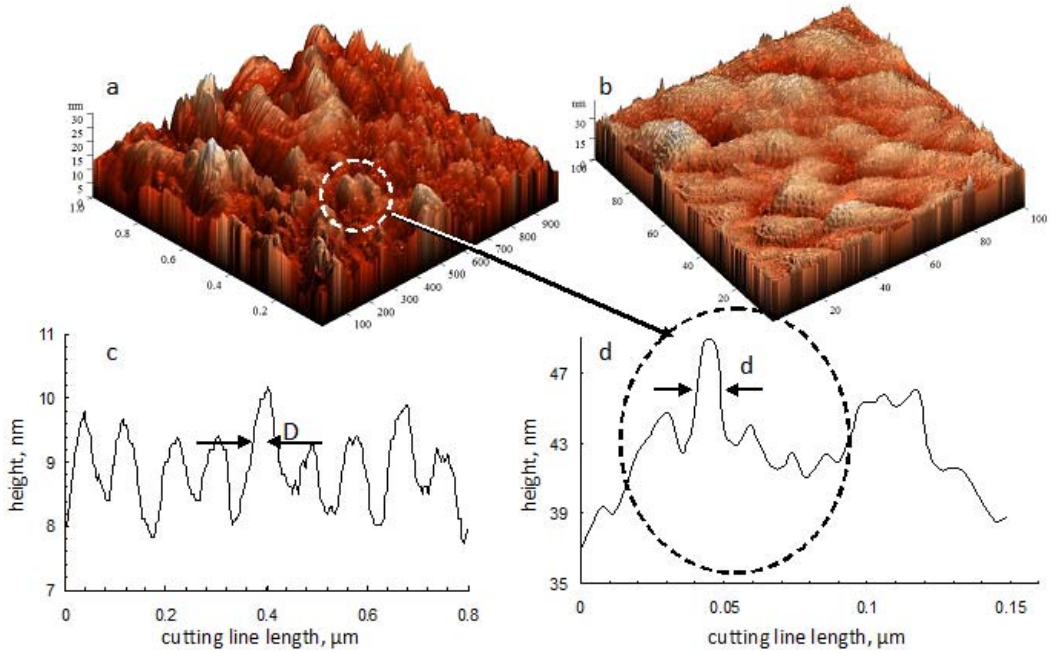

Figure 1. AFM-images (a, b) and profiles of surface iron films (c, d) in initial state (a, c) and after chemical etching (b, d).

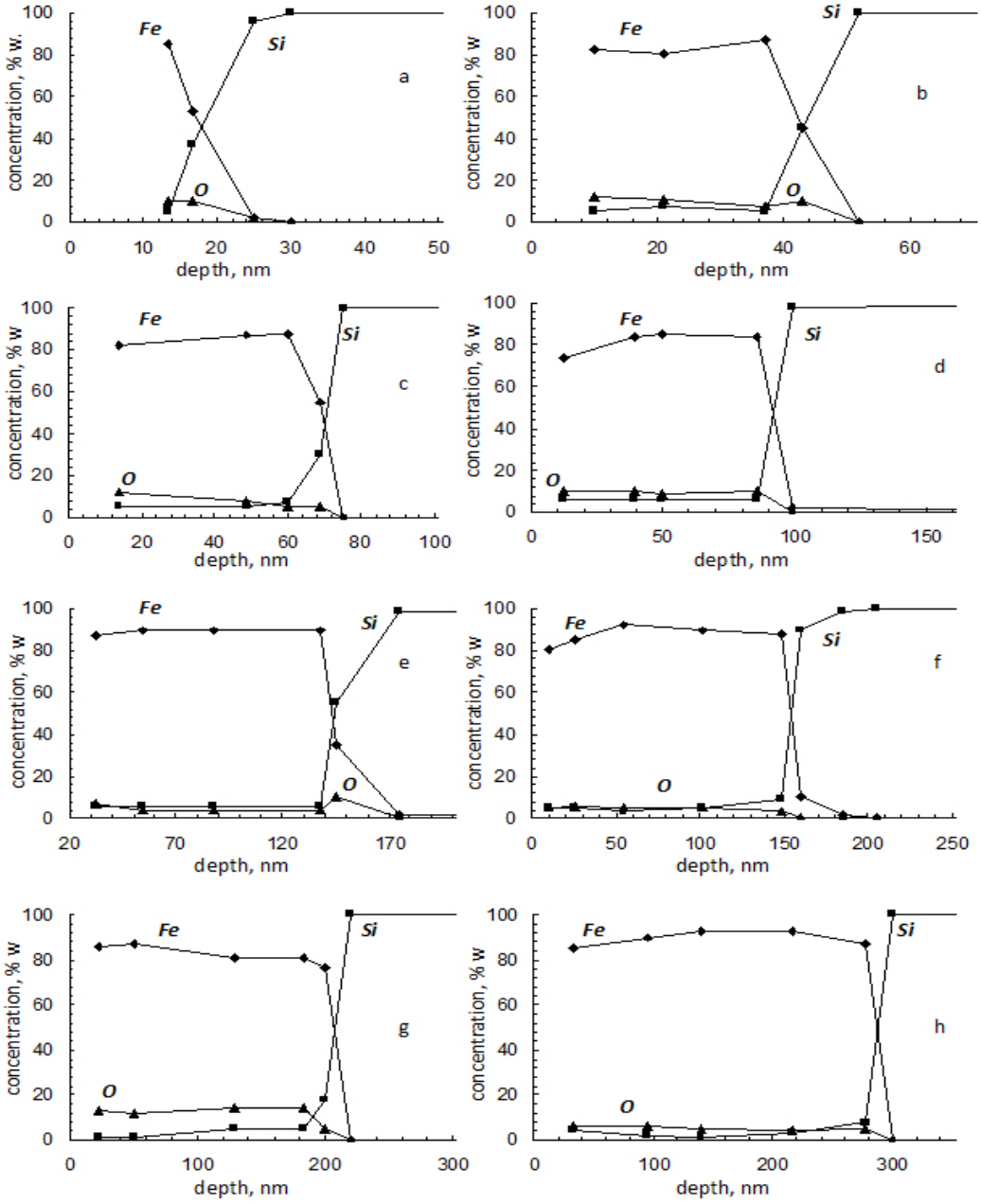

Figure 2. Concentration profiles on depth for iron films with thickness: 24 (a), 45 (b), 62 (c), 100 (d), 150 (e), 173 (f), 208 (g) и 270 (h) in initial state.

Iron films were obtained in the range of thickness (h) from 24 to 270 nm. XRD results showed that the films are formed in their low-temperature α-Fe modification with the bcc lattice. Any other phases in the film are absent. Values of the average grain diameter (d) calculated by the broadening of the main reflection (110) are in the range of 9 to 20 nm (Table 1). The AFM-surface studies showed that the films have a distinct globular structure (Figure 1) with an average globule size (D) (Table 1). The data (Table 1) showed that the

globule size 3-6 times exceeds the grain size. The value D found from the AFM results is frequently equated with the average grain size [29, 30]. Our data shows that it is not quite correct. After chemical etching of the film surface, the AFM results showed (Figure 1 b, d) that grain boundaries are etched on the surface. The size of the etched grains is close to the value found according to the XRD data. It confirms the fact that the globule inside is permeated by intergrain boundaries and is in fact a conglomeration of grains. The globule may include grains with different crystallographic orientation. Therefore, unlike the grain, the globule is not an area of coherent scattering and is not detected by XRD. The concentration depth profiles of elements (Figure 2) indicate that in some cases the oxygen content reaches 10%. Since the maximum solubility of oxygen in the equilibrium iron lattice does not exceed 0.1% and oxidic phases are not detected in the film, the oxygen detected by RBS is adsorption oxygen located on the intergrain boundaries and belongs to the layer of natural oxide on the silicon surface. The Fe/Si transition region (Figure 2) is narrow and does not exceed 10 nm, which proves the absence of the mutual diffusion of iron and silicon and confirms the position of the authors [6, 19].

When iron films are heated, the following changes in their structure occur. When the temperature reaches 130^0C (Figure 3), there is a distortion of the iron lattice (the main reflex (100) is shifted towards lower angles) with the increase of its parameter up to 2.8737Å (in the initial state of the film, this value is 2.8663Å). The concentration profiles of the elements after heating and cooling (Figure 4) are different from the initial ones (Figure 2): the width of the transition Fe/Si area considerably increases, and intermediate points appear in it. It indirectly proves that at the temperature of 130^0C the mutual diffusion of iron and silicon evolves, the possibility of which at increased temperatures was noted before in [20, 21]. However, the value of the lattice distortion is estimated for the first time. The collection of the BFS and XRF data leads to the conclusion of a solid solution forming in the transition Fe/Si area. The same process was also observed in [23], but the question about the basic lattice in the solid solution remained open for discussion. The results we obtained in the present study suggest that the observed solid solution is formed on the basis of the distorted α-Fe lattice.

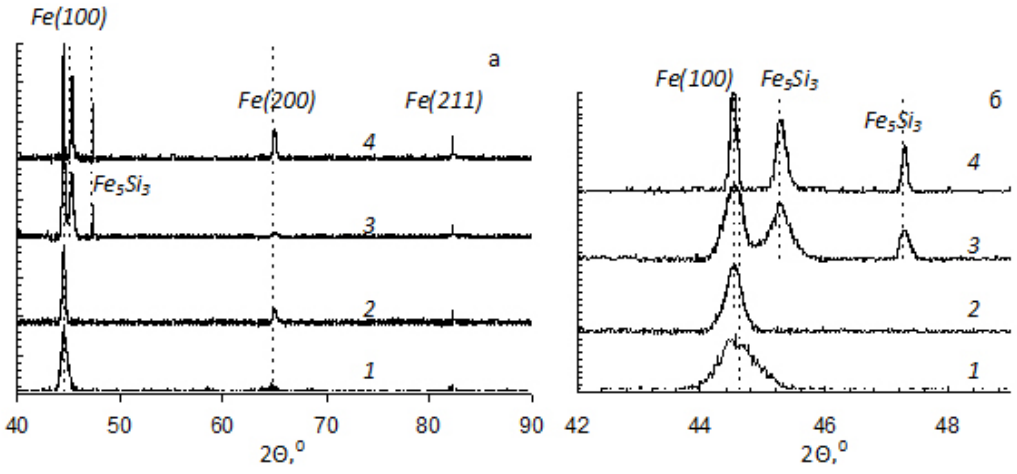

Figure 3. The results of high-temperature XRD (a) and fragment of diffraction-curves (b) in initial state (line 1) and under temperatures: 130 (line 2), 180 (line 3) and 300 (line 4) ^{0}C.

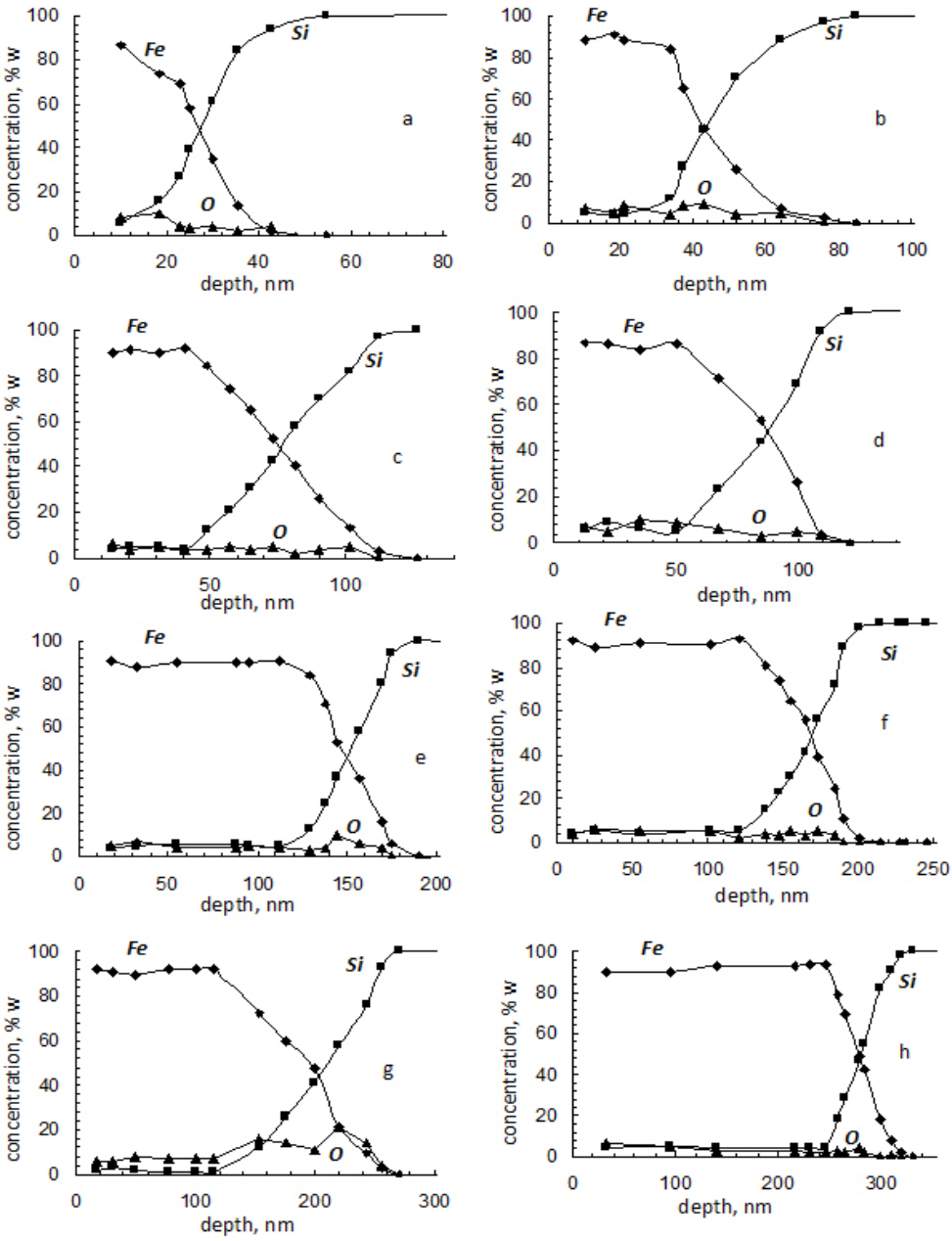

Figure 4. Concentration profiles on depth for iron films with thickness: 24 (a), 45 (b), 62 (c), 100 (d), 150 (e), 173 (f), 208 (g) и 270 (h) nm after heating and cooling.

The increase of temperature up to 180^0C leads to the formation of the Fe_5Si_3 phase, in which the silicon content is not less than 38%. In previous researches the formation of such a phase was observed only at the initial stage of a monolayer iron film forming on the silicon surface. The phase is unstable and is transformed into other silicides [23]. It is known that the Fe_5Si_3 silicide phase in the bulk state is an ordered solid solution (η-phase) existing only at temperatures above 825^0C. It was noticed for the first time that on the Si (100) surface in an

iron film not only Fe_5Si_3 silicide is formed at a lower temperature but that it stabilizes at room temperature. It was also stated that after the formation of the Fe_5Si_3 phase the iron lattice deformation up to 2.8737Å, observed at 130^0C, remains (Figure 3). In other words, at the temperature of 180^0C both the solid solution phase and the Fe_5Si_3 phase are found in the film. It means that the specified silicide is formed without a solid solution decomposition. In the bulk state of the Fe-Si system at room temperature only the ε-phase is stable, which was not detected in our films. The ε-phase in an iron film was previously observed in [22], its formation, however, was caused not by the direct interaction of iron and silicon but by the transformation of the Fe_3Si phase [24], which first transforms into the ε-FeSi (with temperature less than 250^0C), then into the γ- $FeSi_2$ phase (350^0C), and then β-$FeSi_2$ is formed (the temperature is above 500^0C) [26]. However, in our experiments the direct formation of the Fe_5Si_3 phase is observed, and any other phases including Fe_3Si [24] which is prior to the formation of Fe_5Si_3 were not detected, and further heating of the films up to 500^0C does not lead to any changes (Figure 3). In addition, the formation of Fe_5Si_3 develops at a considerably lower temperature. To clarify the reasons, one should take into account the differing views of different authors on the minimum thickness of the film when the Fe_3Si phase can be formed. Thus, according to [24], it is observed at the film thickness of 5-6 monolayers, while but in accordance with [22] - at a thickness of not less than 10 monolayers. It can be concluded that the direct formation of the Fe_5Si_3 phase detected in our experiments is due to a significantly higher film thickness. However, film thickness in itself cannot be a physic-chemical factor determining the film phase composition. We can conclude that the film structure, at which processes like polygonisation and recrystallization become probable during heating, may be such a factor. Their development in thin films previously remained understudied.

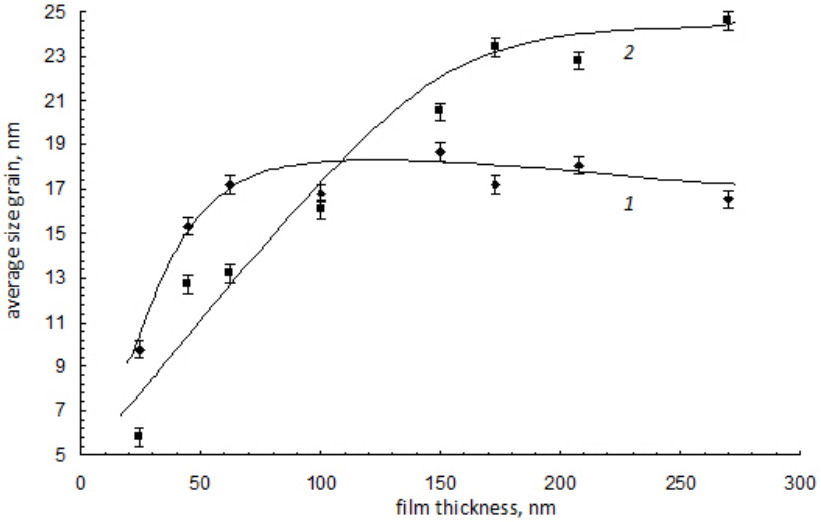

Figure 5. The dependence of average size grain of iron films in initial state (line1) and after heating-cooling (line 2) on thickness.

A direct characteristic of the film structure is its average grain size. Its dependence on film thickness in the initial state (Figure 5, curve 1) and after heating and cooling (Figure 5, curve 2) is interesting. It is clear that the general trend of the curves lies in the increase of the grain size together with the increase of film thickness. However, it is possible to distinguish a

"critical" thickness value of 100 nm on these curves. At h < 100 nm the initial grain is bigger than after heating, and at h > 100 nm it is other way round. It is obvious that the appearance of the "critical" thickness value is the "size-effect" displayed. To clarify the "size-effect" nature it is necessary to analyze the changes in the structure and composition of iron films. Informative methods of researching such structural changes are high-temperature XRD performed in-situ and the measurement of temperature dependencies on resistivity (RT-curves plotting).

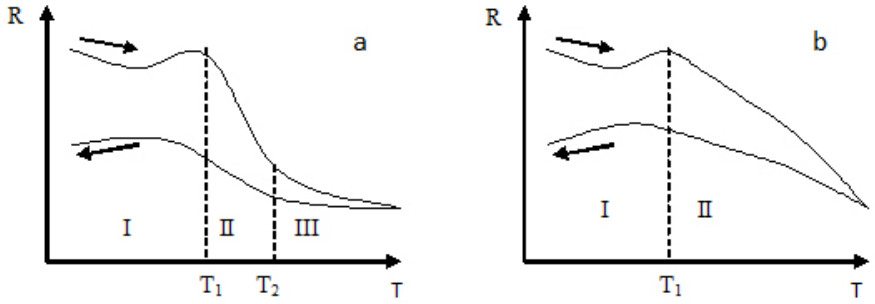

Figure 6. R-T-dependences of iron films with thickness less (a) and more (b) 100 nm.

The results showed that all the RT-curves can be divided into two groups (Figure 6) depending on film thickness. As before, the "critical" value of film thickness at which the RT-curves of one group move to the other is about 100 nm. This thickness value correlates well with the one that was found in the dependency of the grain size on film thickness. The RT- dependencies of the first group (h < 100nm) comprise three areas (Figure 6): at $T < T_1$ film resistance is practically unchanged (area I), in the temperature range between T_1 and T_2 a sharp decrease of resistance is observed (area II), at $T > T_2$ there is a slight increase in resistance (area III). RT-dependencies of the second group (h> 100nm) are characterized by the absence of the thermal point T_2 (Figure 6b). The numerical values of the temperature points T_1 and T_2 are shown in Table 2. In order to interpret the obtained RT-dependencies, we will consider them together with the results of high-temperature XRD. The grain sizes of each film observed in different temperature ranges are shown in Figure 7. The data indicates that at $T < T_1$ the grain size is almost constant, in the range of $T_1 < T < T_2$ the grain size decreases by more than 25%, at $T > T_2$ the grain size remains constant. It is known that while temperature is increasing the resistance of the metal should grow, whereas in our RT-curves its decrease is observed. To explain this fact, it should be taken into account that the film resistance in the initial state is substantially higher than the value calculated for the bulk state (Table 2). For example, according to [31], the difference may reach 55%. The reason for this is a structure containing defects which are the centers of charge scattering. For example, papers [3,28] describe a sharp increase of conductivity with the increase of film thickness, which is caused by the change of the number of structural defects. The reduction of film resistance at the increase of temperature observed in our RT-curves is, in fact, stipulated by the decrease of the concentration of charge scattering centers and by the structure reaching the equilibrium state. The resistance is closer to the calculated value. Both some decrease of resistance at $T < T_1$ and the constancy of the average grain size may indicate the development of the "structure recovery" process consisting in reducing the concentration of point defects due to their

annihilation. Typically, the second stage of structure transformation is the polygonization of grains which developes by the movement of dislocations and the formation of dislocation-free crystal regions. The decrease observed in resistance and grain size in the range of $T_1 < T < T_2$ are proof of polygonisation developing in iron film grains. The third stage of structure transformation is the recrystallization of grains which occurs at $T > T_2$. However, the recrystallization initiation temperature is not constant and depends on the concentration of defects. With the increase of film thickness, the number of defects decreases, which leads to an increase in the recrystallization start temperature. This explains the disappearance of the point T_2 on the RT-dependencies of the second group of films (h > 100 nm).

Table 2. Resistance of iron films and temperature points of R-T-dependences

№	h, nm	R_{init}, Ohm	R_{col}, Ohm	R_{calc}, Ohm	T_1, °C	T_2, °C
1	24	185.0	67.0	27.4	240	440
2	45	80.0	28.0	14.6	250	400
3	62	42.0	20.6	10.6	300	420
4	100	50.0	8.6	6.6	365	-
5	150	16.1	7.5	4.4	385	-
6	173	22.0	4.7	3.8	380	-
7	208	19.4	5.4	3.2	360	-
8	270	6.9	2.4	2.4	320	-

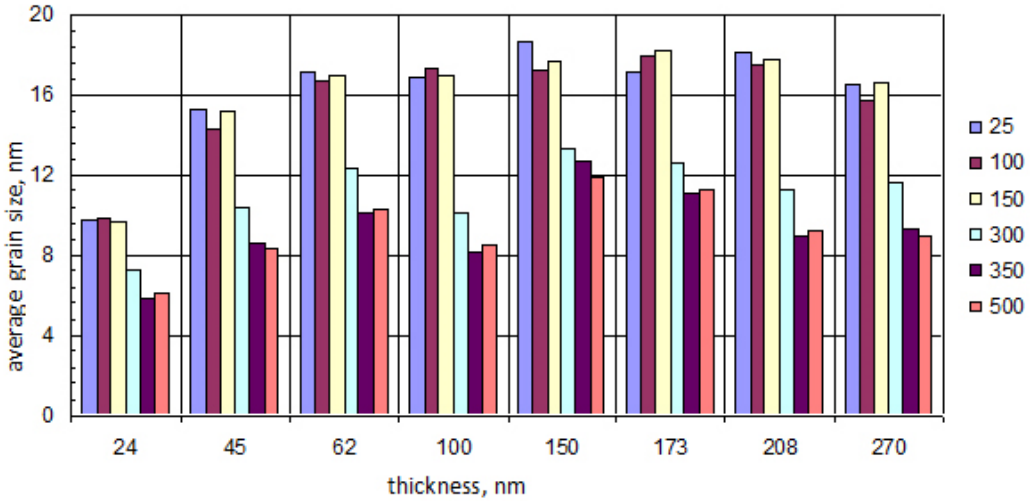

Figure 7. The distribution of average grain size of iron thin films under various of temperature (shown on the right).

Thus, the appearance of the “critical” value of iron film thickness of 100 nm is stipulated by the peculiarities of structure transformation during the increase of temperature. At h < 100 nm transformations occur: “structure recovery,” polygonization, recrystallization, and at h > 100 nm the recrystallization stage does not exist. It should also be noted that solid solution in the Fe/Si transition area forms in the temperature range of the “structure recovery,” and the appearance of the Fe_5Si_3 phase may be due to the development of polygonization. The

findings are evidence of the relationship between the phase formation processes and the structure transformation of the film, which requires further research.

CONCLUSION

1. In iron films obtained by magnetron sputtering on a single crystal silicon substrate, the existence of globules is stated, the average size of which according to AFM data is 3-6 times larger than the grain size according to XRD data. It is proved that the globules are a conglomeration of grains with different crystallographic orientation.
2. Phase transformation stages occurring in the iron film are stated. At a temperature of 130^0C Fe (Si) solid solution is formed which is accompanied by the expansion of the iron lattice and the increase of its parameter. At a temperature of 180^0C Fe_5Si_3iron silicide is formed, for which the stabilization at room temperature with the film thickness of 20 nm is first detected. The formation of Fe_5Si_3 silicide occurs without the decomposition of the solid solution.
3. The "critical" value of iron film thickness (100 nm) is found, the appearance of which is caused by the difference in structure transformation processes during the heating of the film. When the thickness is less than 100 nm, "structure recovery," polygonization and recrystallization occur. When the thickness is more than 100 nm, the recrystallization process does not occur, which is due to the decrease of the film defect with the increase of thickness.
4. The formation of Fe(Si) solid solution occurs in the temperature range of "structure recovery" (annihilation of point defects) which may cause the subsequent formation of Fe_5Si_3 silicide.

REFERENCES

[1] Hathaway K. B., Cheng S. F., Mansour A. N. "Structure and magnetism of sputtered Fe/Cu multilayers." *J. Magn. Mater* 126: 79.

[2] Kummerle W., Gradmann U. 1977. "Ferromagnetism in γ-iron." *Solid State Commun.* 24: 33.

[3] Gubiotti G., Albini L., Tacchi S., Carlotti G., Gunnella R., Crescenzi M.De. 1999 "Structural and magnetic properties of epitaxial Cu/Fe/Cu/Si(111) ultrathin films" *Phys. Rev.* 60:17150.

[4] Antonets I.V., Kotov L. N., Nekipelov S. V., Golubev. Ye. A. 2004. "Nanostructure and conductivity of thin metal films" *Technical Physics* 49:306.

[5] Antonets I. V., Kotov L. N., Nekipelov S. V., Karpushov E. N. 2004. "Conducting and reflecting properties of thin metal films" *Technical Physics* 49:1496.

[6] Gomoyunova M. V., Voistrik T. E.. Pronin I. I.2009. "Interaction of cobalt atoms with an oxidized Si(111)7 × 7 surface" *Technical Physics* 54:753.

[7] Sadashivaiah P.J., Sankarappa T., Sujatha T., Santoshkumar R. 2010. "Structural, magnetic and electrical properties of Fe/Cu/Fe films" *Vacuum* 85:466.

[8] Tacchi S., Bruno F., Carlotti G., Cvetko D., Floreano L., Gubbiotti G., Madami M., Morgante A., Verdini A. 2002. "Structure and magnetism of Fe/Cu(110) thin films" *Surface Science* 507:324.

[9] Xu W. J., Zhang B., Wang Z., Chu S.S., Li W. 2008. "Scaling law of anomalous Hall effect in Fe/Cu bilayers" *Eur. Phys. J. B.* 65: 233.

[10] Bergmann G. 2006. "Analysis of the anomalous Hall effect in a double layer of a ferromagnetic and a normal metal" *Eur. Phys. J.* 54: 19.

[11] Deschamps A., Militzer M., Poole W. J. 2001. "Transformations and Microstructures - Comparison of precipitation kinetics and strengthening in an Fe-0.8% Cu alloy and a 0.8% Cu-containing low-carbon steel" *ISIJ Int.* 41:196.

[12] Fine M.E., Liu J. Z., Asta M. D. 2007. "An unsolved mystery: The composition of bcc Cu alloy precipitates in bcc Fe and steels" *Materials Science and Engineering A.* 463:271.

[13] Hornbogen E. 1962. "The role of strain energy during precipitation of copper and gold from alpha iron" *Acta Metall.* 10:525.

[14] Othen P. J., Jenkins M. L., Smith G. D. W., Phytian W. J. 1991. "Transmission electron microscope investigations of the structure of copper precipitates in thermally-aged Fe–Cu and Fe–Cu-Ni" *Philos. Mag.Lett.* 64: 383.

[15] Pareige P., Russell K. F., Miller M. K. 1996. "APFIM studies of the phase transformations in thermally aged ferritic FeCuNi alloys: comparison with aging under neutron irradiation" *Appl. Surf. Sci.* 94-95:362.

[16] Goodman S.R., Brenner S., Low J.R. 1973. "An FIM-atom probe study of the precipitation of copper from lron-1.4 at. pct copper. Part I: Field-ion microscopy" *Metallurgical and Materials Transactions B.* 4: 2363.

[17] Gubbiotti G., Albini L., Carlotti G., Loreti S., Minarini C., Crescenzi M. De. 1999. "Fcc-bcc phase transition of epitaxial (111)-Fe films: a structural and magnetic study" *Surface Sci.* 680: 433.

[18] Saltykov S. N., Khoviv A. M., Maksimenko A. A. 2011. "Polymorphic modification of iron it the thin film state." *Russian Journal of Inorganic Chemistry* 56: 331.

[19] Gomoyunova M. V., Malygin D. E., Pronin I. I. 2006. "Interaction of iron atoms with the oxidized silicon surface" *Technical Physics.* 51:1243.

[20] Garnier M. G., Arcos T., Boundaden J. 2003. "Photoemission study of the iron-induced chemical reduction of silicon native oxide" *Surf. Sci.* 536:130.

[21] Saltykov S. N., Khoviv A.M. 2010. "Vzaimoproniknovenie zheleza i medi v tonkih plenkah i ih fazovyj analiz" *Kondensirovannye sredy i mezhfaznye granitsy.* 12: 5.

[22] Alvarez J., Hinarejos J. J., Michel E.G. 1992. "Electronic structure of iron silicides grown on Si(100) determined by photoelectron spectroscopies" *Phys. Rev. B.* 45:14042.

[23] Hasegama M., Kaboyeshi N., Hayashi N. 1996. "Reactions of monolayer Fe with Si(001) -dihydride and -2x1 surfaces" *Surf. Sci.* 357-358: 931.

[24] Gallego J. M., Miranda R. 1991. "The Fe/Si(100) interface" *J. Appl. Phys.* 69:1377.

[25] Bertoncini P., Wetzel P., Berling D. 1997. "Epitaxial growth of Fe(001) on CoSi2(001)/Si(001) Structural and electronic properties" *Phys. Rev. B.* 60:11123.

[26] Arzt E. 1998. "Size effects in materials due to microstructural and dimensional constraints: a comparative review" *Acta Mater.* 16:5611.

[27] Kataoka K., Hattori K., Miyatake Y., Daimon H. 2006. “Iron silicides grown by solid phase epitaxy on a Si(111) surface: Schematic phase diagram.” *Phys. Rev. B.* 74:155406.

[28] Alvarez J., Parga A. L., Hinarejios J. J., Figuera J. 1993. “Initial stages of the growth of Fe on Si(l 11)7x7” *Phys. Rev. B.* 47:16048.

[29] Tsushima R., Michishita Y., Fujii S., Okado H, Umezawa K. 2005. “Growth Process and Structure of Fe/Si(111) Ultrathin Film: Transition from Single-Domain Fe(111)/Si(111) to β-$FeSi_2$” *Surf. Sci.* 73:579.

[30] Ou M. N., Yang T. J., Harutyunyan S.R., Chen C.D. 2008. “Electrical and thermal transport in single nickel nanowire” *Appl. Phys. Letts.* 92:063101.

[31] Gusev A. I. 1998 “Effects of the nanocrystalline state in solids” *Phys. Usp.* 41:49.

Smart Nanocomposites
Volume 7, Number 1
ISSN: 1949-4823

MOTT-PEIERLS PHASE TRANSITION IN VO_2 FILMS

A. V. Ilinskiy[1], O. E. Kvashenkina[2], and E. B. Shadrin[1,*]
[1]Ioffe Physical Technical Institute of the Russian Academy of Sciences, Russia
[2] St. Petersburg State Polytechnical University, Russia

ABSTRACT

It is shown that the phase transition consists of two inherently different transitions, i.e., electronic and structural ones. A continuous electronic Mott-transition occurs in the range 0–140°C; in the range 20–80°C, a series of discontinuous structural phase transformations (Peierls-transitions) occurs in film nanocrystallites at various fixed temperatures. The temperatures of the structural transformations are related to nanocrystallite sizes. An essentially new form of the elementary hysteresis loop of an individual nanocrystallite is constructed. Based on these results, the electronic component of the semiconductor–metal phase transition in VO_2 films is identified and studied.

Keywords: vanadium dioxide, phase transition, strong correlations

INTRODUCTION

Vanadium dioxide is a model object for studying electron–electron correlations in solids, which exhibits a number of unique physical properties due to such correlations. VO_2 is both an insulator Mott and an insulator Peierls.

In [1, 2], the idea was experimentally validated, according to which the Mott electronic transition continuous in temperature occurs as the temperature of crystalline VO_2 increases in the range from room temperature to the critical temperature T_c = 67°C (the monoclinic and tetragonal_phase equilibrium temperature). This transition initiates the structural phase transition (PT) in the macroscopic VO_2 crystal at $T = T_c$ = 67°C. At this temperature, the lattice symmetry in the macroscopic single crystal abruptly changes from the monoclinic (M_phase) to the tetragonal, rutile phase (R_phase). The material conductivity also abruptly increases by several orders of magnitude, since the monoclinic phase is a semiconductor, while the tetragonal phase is a metal.

Figure 1 shows the published experimental data on the study of the temperature dependences of VO_2 conductivity [3, 4], analysis of which makes it possible to justify the

* jenjasha@yandex.ru.

proposed new shape of the elementary hysteresis loop of the reflectance of an individual nanocrystallite.

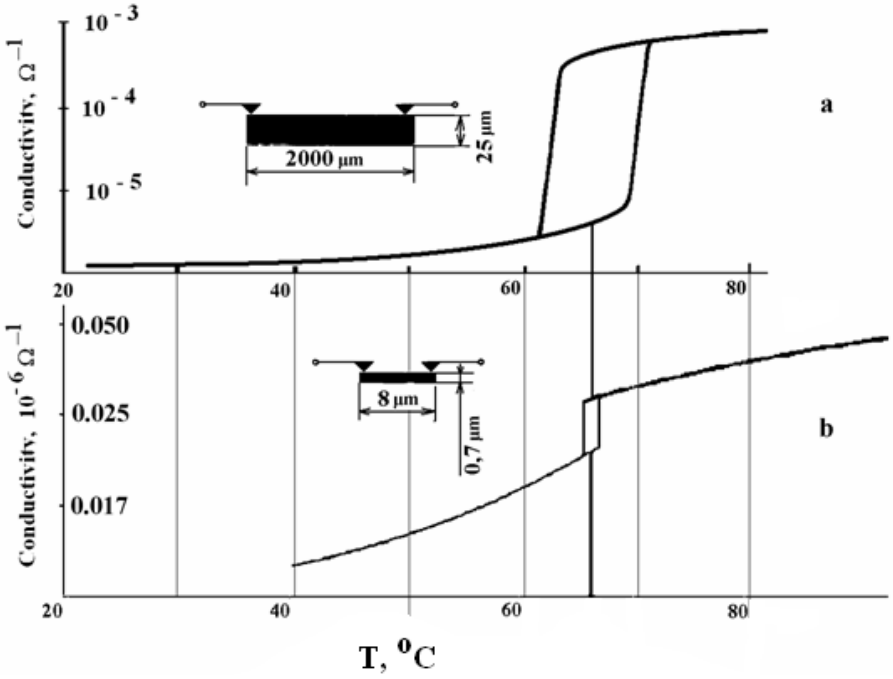

Figure 1. Temperature dependences of the vanadium dioxide (a) microcrystallite conductivity [3], (b) nanocrystallite conductivity [4].

The energy gap between the bands is 0.7 eV at room temperature. At such a gap, the concentration of equilibrium carriers of both signs is very low. As the temperature increases from room temperature to 58°C, the carrier concentration increases though still remaining low. This increase can be detected only using a sensitive experimental technique, e.g., by precision measurements of the sample's conductivity. The experimental results [3, 4] shown in Figure 1 point to the low conductivity of VO_2 single crystals and its very weak increase in the indicated temperature range.

As the temperature increases, the number of such broken σ bonds of V–V dimmers increases, bringing the system as a whole toward the structural PT due to a decrease in the dominant role of dimer σ bonds. The structural PT to the tetragonal phase corresponds to a transition to a state where all ions of the V lattice are arranged at the centers of oxygen octahedron bases, to which they are moved by the forces of V–oxygen ion σ bonds, which are dominant from the instant of PT completion. These forces form undistorted octahedra of the tetragonal phase, which follows from X-ray diffraction data. The critical electron fraction is reached at $T = T_c + \Delta T$.

We note that the mere fact of the beginning of the enhanced breaking of σ bonds of V–V dimers (at T near T_c) does not corresponds to the moment of structural PT completion. The point is that the increase in the lattice symmetry from monoclinic to tetragonal is additionally prevented by elastic forces induced by the surface tension of the outer crystallite boundary and forces of the interaction of the crystallite with the substrate onto which it is deposited.

Therefore, the structural PT requires the breakage of a certain number of dimer σ bonds in addition to the equilibrium number; this additional number should increase with elastic force. This circumstance requires additional heating of the crystal by ΔT which turns out to depend on the crystallite size and degree of its adhesion to the substrate.

As the temperature of the tetragonal phase further increases, after the structural PT, the gradual increase in the conductivity continues.

Figure 2 shows the result of the construction of an elementary loop, i.e., the temperature dependence of the variation in the reflectance ΔR (*T*) of an individual nanocrystallite.

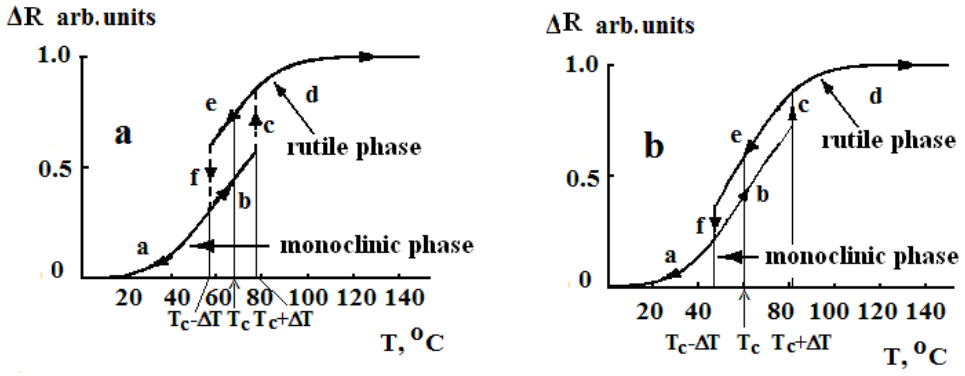

Figure 2. Elementary hysteresis loops of an individual nanocrystallite: a - large grain, b - fine grain.

This change reflects the purely Mott electronic transition in this range. In Figure 2, this process of an accelerated increase in the reflectance corresponds to the portion b in the dependence ΔR(T). The reflectance increase results from the thermal transfer of electrons from the lower 3d|| subband to the descending π* band (Figure 3).

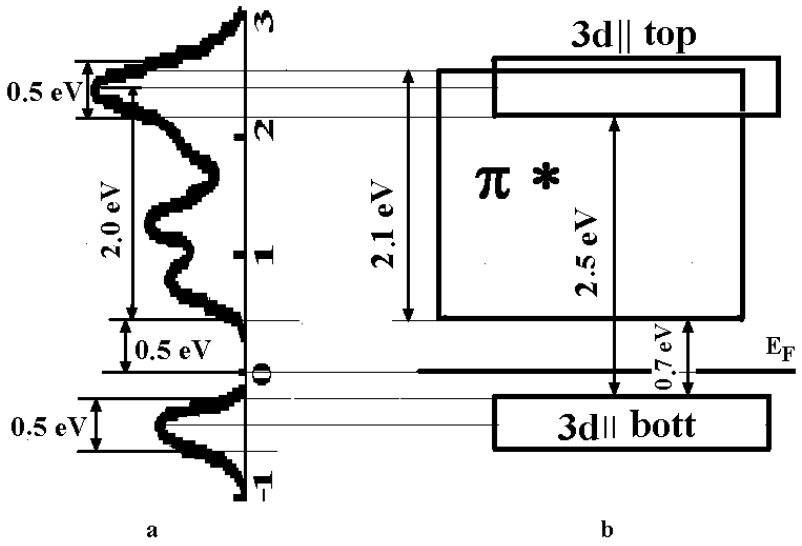

Figure 3. Comparison of (a) the results of calculations [5] with (b) the energy band diagram for VO_2 in the monoclinic semiconductor phase at 300 K.

According to [6], the portion b corresponds to a 4% increase in the reflectance (Figure 2d). It follows from the above that the electronic PT component initiates the structural PT. Thus, the described set of abrupt changes in the band positions at T = Tc + ΔT causes an abrupt jump (upward in temperature) in the electron concentration in the π* band, hence, in the sample reflectance, which is indicated by segment *c*. In the case of the reverse process of decreasing the sample temperature, all described PT stages exactly reproduce each other. The decrease in the tetragonal rutile (R) phase reflectance is described by curves d and e in Figure 2, which correspond to a decrease in the electron concentration in the π* band and, accordingly, an increase in the concentration of dimer σ bonds due to newly restored ones. As the critical concentration of dimers σ bonds is reached at T = Tc – ΔT, the reverse abrupt structural PT from the tetragonal phase to the monoclinic phase, i.e., the reverse Peierls transition, occurs. Simultaneously, an abrupt decrease in the electron concentration in the π* band, initiated by this PT, and an abrupt decrease in the reflectance (vertical segment f) occur. Finally, a further temperature decrease causes a further decrease in the crystal's reflectance in the monoclinic phase, which is also described by curve a in Figure 2. Within the proposed model, the electronic PT component in VO_2 is anhysteretic, and the structure component in the VO_2 microcrystal exhibits thermal hysteresis with an elementary loop width of 2ΔT.

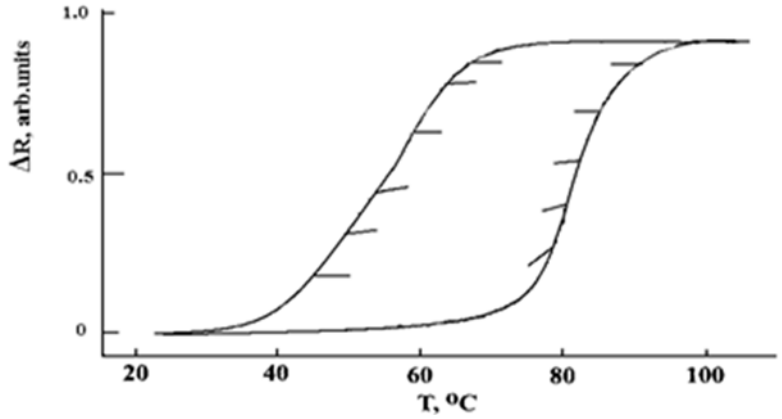

Figure 4. Anhysteretic changes in the VO_2 film reflectance (short segments), resulting from a slight deviation in temperature (from the heating and cooling branches of the major thermal hysteresis loop).

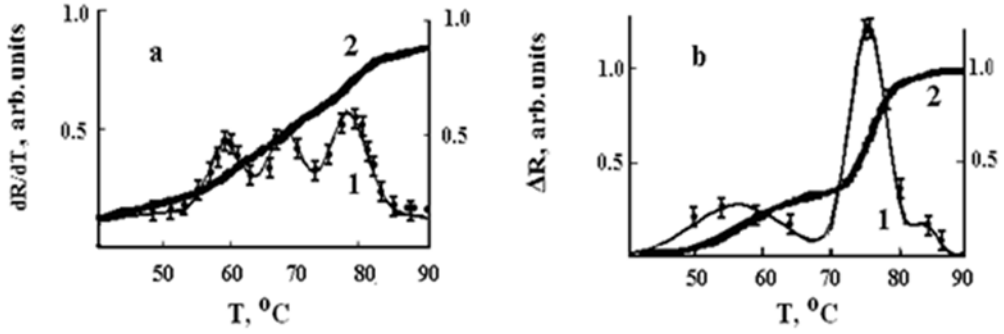

Figure 5. Temperature distributions dR/dT (curve 1) and $\Delta R(T) = \int_{-\infty}^{T} dr$ (curve 2), constructed by the experimental data of Figure 3 for two films a, b.

The procedure of experimental separation of the electronic component of the thermal PT in its pure form is based on the following circumstance. By moving along the heating branch along the major loop to a certain temperature T_k we go back to cooling direction of sample in the range of 2-3^{o}C (Figure 4). In this case the reflectance decrease in according to the behavior of the purely Mott electronic transition without interaction for the structural transition.

For the heating branch of the major loop, monotonic heating by 5–6°C was performed, then heating was terminated $T = T_k$, after which the temperature was reversed followed by cooling by 2–3°C, and heating by 5–6°C was per formed again, and the entire cycle was repeated. In the cooling branch of the major loop, the temperature was gradually decreased followed by a "stop" at $T = T_k$, then the temperature run was reversed as heating by 2–3°C followed by cooling by 5–6°C and repetition of the entire cycle. As a result of such a "multistage" procedure, the obtained major thermal hysteresis loop $\Delta R(T)$ contained a number of anhysteretic segments in the heating and cooling branches (Figure 3). To interpret the obtained experimental data, we constructed a mathematical model of the formation of only the temperature dependence of the reflectance of an individual film microcrystal, but also that of a set of VO_2 crystallites, which determines the experimentally observed total reflectance of the VO_2 film.

When constructing the major hysteresis loop of the film, we assume that the total change in the reflectance $\Delta R(T)$ of the film is defined by the arithmetic sum of contributions to this change by thermal changes in the reflectance ΔR_i of individual film nanocrystallites. Summation considers the difference in the contributions of grains of different sizes to the reflectance, the size distribution of the numbers of grains and the related width and height distribution of the numbers of elementary loops.

In undoped VO_2 films, the electronic PT without hysteresis begins close to room temperature. It high increases the film reflectance by increasing of temperature, yielding the anhysteretic curve $\Delta R(T)$ (curve 2 in Figure 5). At temperatures $T_i = T_c + \Delta T_i$ differented from one another for each i-th group of grains with equalized size, the electronic transition initiates the structural PT in each of such group. In both tetragonal and monoclinic phases the electronic PT without hyseresis continues in all groups of grains above this temperature, (as in that have made fase transition, and that have not made). The anhysteretic electronic transition is ended, reaching saturation at temperature of ~140°C. By summarizing the above, we can conclude that the nature of the electronic component of the thermal PT in crystalline VO_2 films consists of the formation of a decreasing of the energy of many particle electronic states and the gradual disappearance of the gap in the electronic spectrum because of occurrence of free electrons in the empty allowed bands of a strongly correlated material. Free electrons appear in empty allowed bands during the thermal breakage of σ bonds of V–V dimers of the monoclinic phase. This breakage is strongly enhanced by the correlation electron–electron interaction.

REFERENCES

[1] V. Il'inskii, O. E. Kvashenkina, and E. B. Shadrin, *Semiconductors* **45**, 1153 (2011).
[2] V. Il'inskii, O. E. Kvashenkina, and E. B. Shadrin, *Semiconductors* **46**, 422 (2012).

[3] O. P. Vinogradova, A. I. Sidorov, V. A. Klimov, E. B. Shadrin, A. V. Nashchekin, S. D. Khanin, and V. Yu. Lyubimov, *Phys. Solid State* **50**, 1227 (2008).
[4] J. Wei, Z. Wang, W. Chen, and D. H. Cobden, *Nature Nanotechnol*. **4**, 420 (2009).
[5] H. Jiang, R.I. Gomez-Abal, P. Rinke, and M. Scheffler. *Phys. Rev. B.* **82**, 045108-1 - 045108-16 (2010).
[6] W. T. Liu, J. Cao, W. Fan, Z. Hao, M. C. Martin, Y. R. Shen, J. Wu, and F. Wang, *Nano Lett.* **11**, 466 (2011).

Smart Nanocomposites
Volume 7, Number 1
ISSN: 1949-4823

NANO - AND THE MICRODIMENSIONAL COATS POLYCRYSTAL TITANIUM-CONTAINING THE BASES A METHOD OF ELECTROCHEMICAL BORONIZING

E. S. Gorlanov[1,*] and V. Yu. Bazhin[2]
[1]Expert-Al Ltd., Saint Petersburg, Russia
[2]Gorniy University, Saint Petersburg, Russia

ABSTRACT

The technology for the production of wettable aluminium coating was implemented using the method of electro-chemical borating of the carbon-titanium cathode directly at the electrolytic reduction of cryolite-alumina melts in laboratory conditions.

TiC and TiB_2, responsible for the wetting effect, were detected by X-ray phase analysis of cathode surface layer. The mechanism of electro-chemical and chemical processes of Ti-B-C compound formation in the subsurface cathode volume is proposed for the discussion.

Keywords: electro-chemical deposition, borating, carbon-titanium cathode, wettable coating

INTRODUCTION

Electrochemical methods of creating coats are most expedient on items which are used in extreme aggressive conditions of electrolysis processes of the fused salts. In particular, such tryings were most often undertaken on graphitized carbon items, is more exact on a surface of cathode blocks in the conditions of an electrolysis a cryolite-alumina melts [1–9]. The reason for these efforts – presence a wetted aluminum protective coating on the cathode surface uncloses possibility to come nearer to theoretically possible power consumption for obtaining 1 kg of aluminum – 11 kWh.

But, the commercial continuation of these attempts in all cases was absent. And because, as shown in paper [10], by methods of electrodeposition it is extremely difficult or even impossible to create conditions for the synthesis of uniform wettable coating on the whole surface of real cathode materials. From the physical, hence, energetic and electro-chemical point of view the non-uniform surface of composite materials represents a main restriction for the creation of coherent layer of double and triple compounds in the system Ti–B–C.

* gorlanove@yandex.ru.

The possibility to avoid this restriction and chances for the formation of even and uniform wettable coat in the subsurface layer of the cathode appear when reduced elements (i.e., boron) interact not only with cathode material but with its specially inserted impurities as well (with titanium, in our case). Thus, the essence of the proposed method consists in the electrochemical borating of carbon-titanium cathode.

EXPERIMENT

Production of Titanium-Containing Samples

The preparation of material and grain size compositions of the charge, the dosing of carbon components and titanium metal, the agitation and the extrusion of specimens were carried out in accordance with the carbon blocks production technology in laboratory conditions at the carbon plant.

The content of titanium in initial "green" charge specimens made up from 8 to 15% wt. After baking the specimens in the industrial furnace over the period of 23 days the surface of titanium metal grains was successively transformed into interstitial phases of $Ti_6O \rightarrow Ti_3O \rightarrow Ti_2O$ and, to a little extent, into semi-conductor phase of TiO (data of XRD analysis).

Conditions of the Electrolysis Experiments

For experiments were used carbon-titanium specimens size Ø = 30 and h = 50 mm. The basis of the initial melt was applied cryolite technical purity with CR=1.78 or sodium and aluminium fluorides the chemical purity. As additives were used alumina and boron-containing components chemical purity in an amount of 3÷5 wt.%. All experiments were performed at 970 ÷ 990°C in an electrolyte with CR = 2.5 at the electrolysis plant, the diagram of which is shown in Figure 1. In studies, the electrolysis voltage was recorded automatically during the whole period of the process.

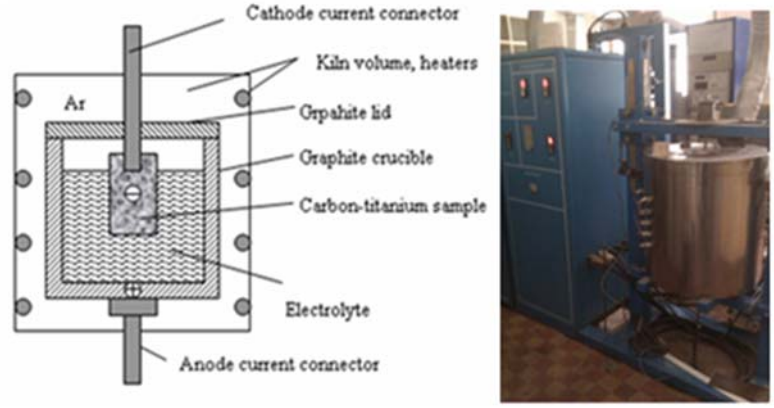

Figure 1. Electrolysis unit.

The installation was connected to the electrolysis with a constant purging of the cell atmosphere with argon. Intrinsically the joint electrical deposition of aluminium and boron onto cathode took place in galvanostatic conditions. It was assumed that boron being deposed onto the cathode would take part in the synthesis of Ti-B-C system compounds, and aluminium on the cathode or its drops on the bottom of the crucible would serve as indirect preliminary indicator of Ti-B-C layer presence or absence.

After their removal from the melt the pictures of the specimen were taken, then the specimen were mechanically treated against electrolyte to be sampled for the X-ray phase analysis and for the preparation of metallographic sections to be used in the electronic microscopy.

RESULTS OF THE EXPERIMENTS AND THEIR DISCUSSION

In this paper we discuss the results of some from more than 30 experiments that were obtained at the current densities of 0.4–1.3 A/cm^2. Also used an extensive database on the decomposition voltage of the compounds obtained in the paper [10].

The article /10/ we calculated decomposition voltage ($E°_p$) of various compounds of boron, titanium and aluminum, which allowed for the analysis of electrolysis processes at a fixed voltage dynamics of the experiment. This used the well-known equation voltage at the electrolysis unit: $U = E_p + [\eta_c + \eta_a + I \cdot R]$. Assumed that the amount of cathode η_c, an anode η_a of the overvoltage at the electrodes and the voltage due to the ohmic resistance of the cell $I \cdot R$ during the experiment does not change. To extend the analysis, in the first approximation considered, this condition holds for different experiments in the same conditions. Then the difference between the two levels (platforms) of the experiment voltage will be characterized by the difference between the voltage of electrochemical decomposition process:

$\Delta U_{exper.} = |U_2 - U_1| = |E^2_p - E^1_p| = \Delta E^0_p$. These simple arithmetic considerations on the one hand, allow us to estimate the decomposition voltage of an unknown process. For example, $E^2_p = E^1_p + \Delta U$ (if known E^1_p). On the other hand, equality $\Delta U_{exper.} \approx \Delta E^0_p$ can serve as a confirmation of the alleged cathodic process. This allowed us to determine ΔU_{exper} many cathodic processes, the values of which we use in this work.

In experiments DT11 and DT14 at the cathode current density of 0.7 A/cm^2 the respective concentration of boron- and aluminium bearing components in electrolyte was selected; this concentration allowed reducing or eliminating the deposition in the cell and on the cathode.

However, the dynamics of the voltage at the beginning of experiment DT14 shows the extremely high initial concentration of oxides in the melt and, consequently this is evidence of intensive formation of the complexes, having a low solubility in electrolyte. These complexes are being dissolved as the melt is being depleted with electrically active components. During first nine hours the successive reduction of boron from the compounds having lowest decomposition potentials took place.

№	Initial electrolyte composition, % wt.				Additives during the exper., % wt.				Parameters of experiment		
	substrate	C.R.	Al_2O_3	$Na_2B_4O_7$	Al_2O_3	$Na_2B_4O_7$	AlF_3	t,hour	τ,hour.	J,A/cm^2	T,°C
DT11	Cryolite	2,5	4	3	0,35	0,75	-	3	42	0,7	990
DT14	Cryolite	2,5	4	3	0,4	0,75	0,5	3	45	0,7	990

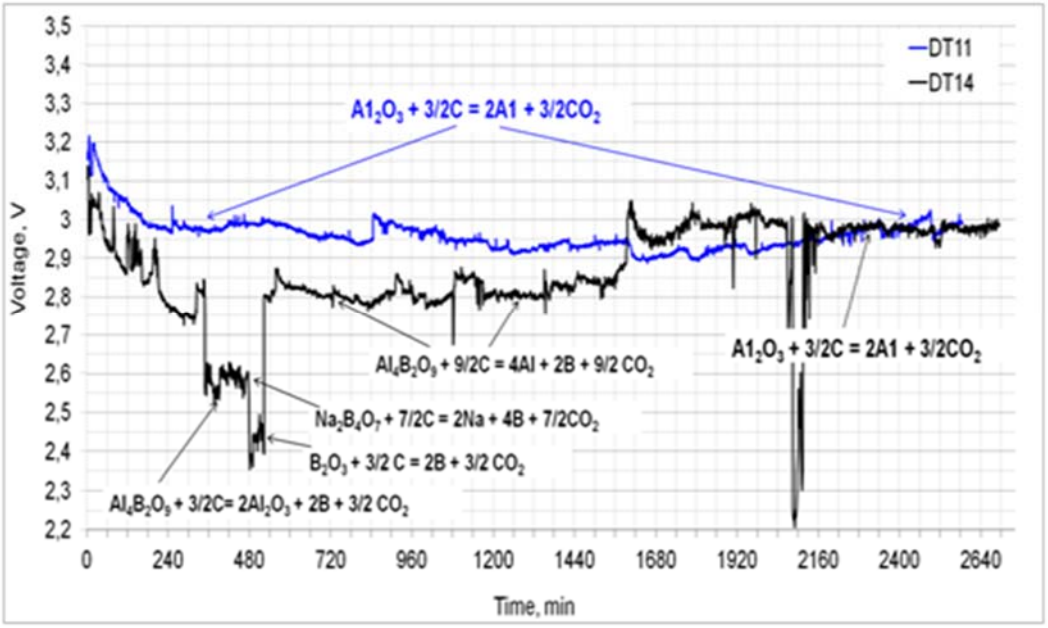

Figure 2. Voltage dynamics in DT11 and DT14.

Current voltage DC consistently varies depending on the presence in the melt of certain complexes, bound or free ions of primary and secondary ions.

Reactions	$\|E^0_p\|$, V	$U_{exp.}$, V	$\|E^0_p\|$, V	$U_{exp.}$, V	$\|E^0_p\|$, V	$U_{exp.}$, V	$\|E^0_p\|$, V	$U_{exp.}$, V
$A1_2O_3 + 3/2C = 2A1 + 3/2CO_2$	1.154	2.980*	1.154	2.980*	1.154	2,980*	1.154	2.980*
$Al_4B_2O_9+3/2C=2Al_2O_3+2B+3/2CO_2$	0.724	2.550	-	-	-	-	-	-
$Na_2B_4O_7+7/2C=2Na+4B+7/2CO_2$	-	-	0.783	2.600	-	-	-	-
$B_2O_3 + 3/2\ C = 2B + 3/2CO_2$	-	-	-	-	0.626	2,445*	-	-
$Al_4B_2O_9 + 9/2C = 4Al+2B+9/2CO_2$	-	-	-	-	-	-	1.011	2.810
Difference of potentials	0.430	0.430	0.371	0.380	0.528	0,535	0.143	0.170
*- defined in /10/								

When 9 hours of reduced dosing of aluminium and boron oxides into electrolyte expired, the quantity of electrically positive ions in the melt finished, and the voltage drastically increased to the potentials of class $Al_4B_2O_9$ –2.810 V. Under this mode of complex boron reduction onto the carbon-titanium cathode this process continued over the period of 17 hours, accompanied with reactions of boron interaction with components of substrate:

$4B + C = B_4C$	ΔG^0_R = -58.10 kJ
$Ti + 2B = TiB_2$	ΔG^0_R = -303.00 kJ
$3Ti + B_4C = 2TiB_2 + TiC$	$\Delta G_R°$ = -557.50 kJ

In addition, as during this 9-hour period the access of electrolyte with boron oxide, dissolved in it, was free, following reactions are quite possible here:

$B_2O_3 + Ti + 3/2C \rightarrow TiB_2 + 3/2CO_2$	$\Delta G_{1300K} = -322.20$ kJ
$B_2O_3 + TiO_2 + 5/2C \rightarrow TiB_2 + 5/2CO_2$	$\Delta G_{1300K} = -365.97$ kJ

After the depletion of boron ions the electrolytic process continued at the voltage of 2.980 V by electrical reduction of $Al^{3+}+3e \rightarrow Al$ to aluminium metal on the Ti-B-C surface.

Contrary to DT14, after the removal of overvoltage of 200 mV, caused by desorption of oxygen, adsorbed by crucible-anode, the voltage of DT11 indicated approximately 2.980 V and the process of electrolysis continued over the 9-hour period.

This initial 9-hour period could be interpreted as joint discharge of boron $B^{3+} + 3e \rightarrow B$ and aluminium $Al^{3+} + 3e \rightarrow Al$ ions on the cathode surface.

These processes prepared the conditions for the interaction of $Ti+2B = TiB_2$ and for the production of cathode surface wettable with aluminium which layer started to be formed on it.

The final period of the experiment continued in the mode of limiting current which resulted in the return of the voltage to the level of 2.980 V with seldom depolarization effects within 0.070 V. These small voltage spikes are probably due to the formation of aluminium borides.

The layer of aluminium 3-5 mm thick was formed with good adhesion to carbon material on the cathode surface, immersed into electrolyte.

The wetting properties of substrate provided the availability of aluminium layer on the surface of cathode. The good adhesion of the metal to the cathode did not allow sampling from the surface for the XRD analysis.

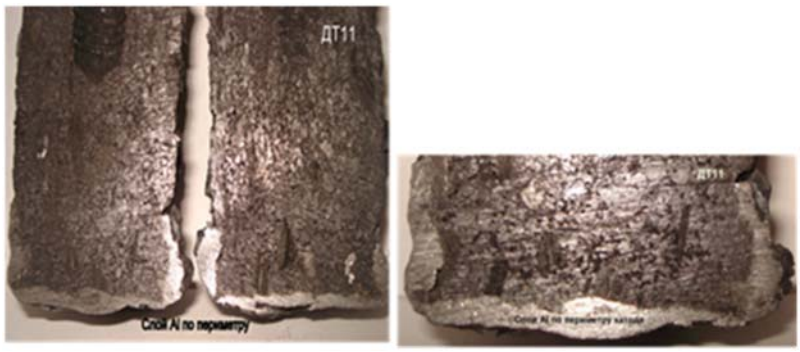

Figure 3. Longitudinal section of DT11 specimens.

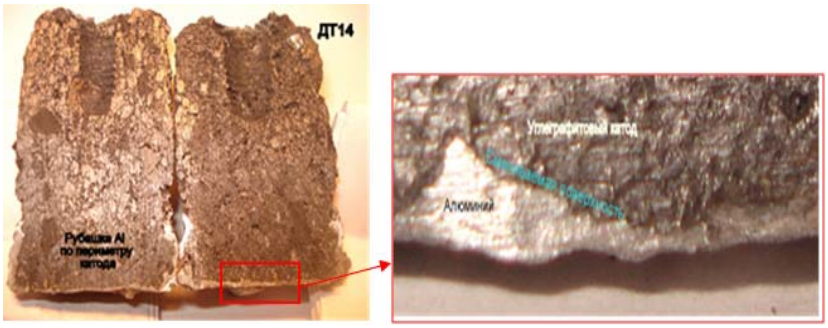

Figure 4. Exterior of cathode DT14 after the experiment.

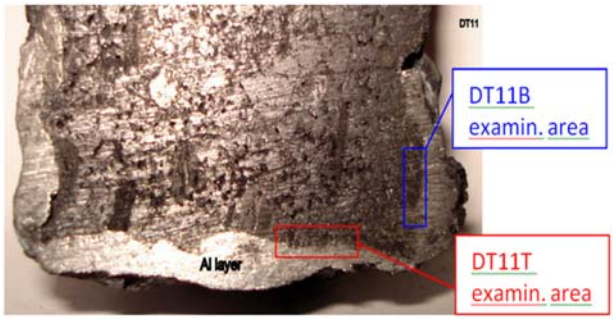

Figure 5. Cross-section of the DT11 specimen.

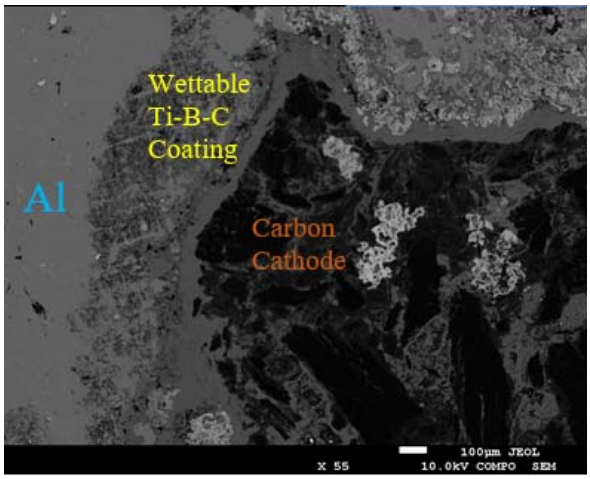

Figure 6. Microstructure of the DT11B specimen (x55).

For SEM-EDS investigations the samples were taken and specimens of side (DT11B) and end (DT11T) surfaces were prepared (Figure 5). Several segments of each specimen (section) were examined at the interface aluminium/carbon. Here we'll show some of them only.

The presence of wettable coating on the segment of specimen DT11B is clearly seen. Due to this fact for the full comprehension let's see the results of energy-dispersion analysis and photo pictures of microstructure segment in back reflected electrons (Figure 6). Visually we can distinguish areas of different contrast. And the results of EDS analysis fix the joint presence of titanium, boron and carbon between points 5 and 9 of scanning line (Figure 7).

Thus, the SEM-EDS analysis founds the surface 500 µm layer of titanium carbo-boride with rather good wetting properties in respect with aluminium. In expectation of analysis the end part section of the cathode DT11T collapsed; therefore this was not the interface of aluminium and carbon in the cross-section that was subjected to the SEM-EDS analysis but the segments of completely intact surface of this border from the reverse, earlier inaccessible side were. Figure 8 shows the segment with indication of some points where the analysis was carried out. On closer examination in compositional contrast, the field of dark color represents a textured mixture of carbon particles, adjacent to the light field that is located below (between the layer of aluminium and carbon surface). As EDS-analysis shown, this light field represents the layer of borides, generated during the 42-hour experiment. Points 2 and 4 represent boride-titanium compositions of $TiB_{2.8}$ and $TiB_{3.2}$ accordingly.

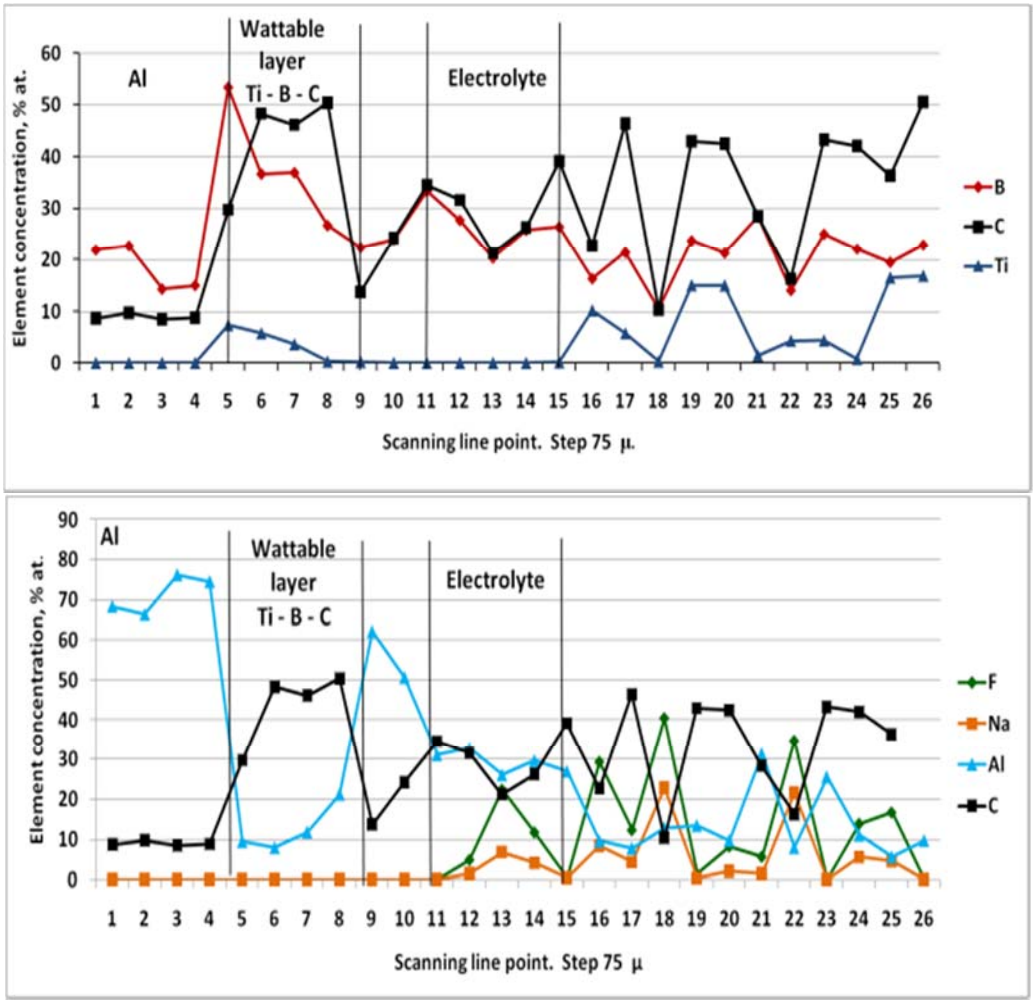

Figure 7. Results of EDS-analysis in the line of point spectra.

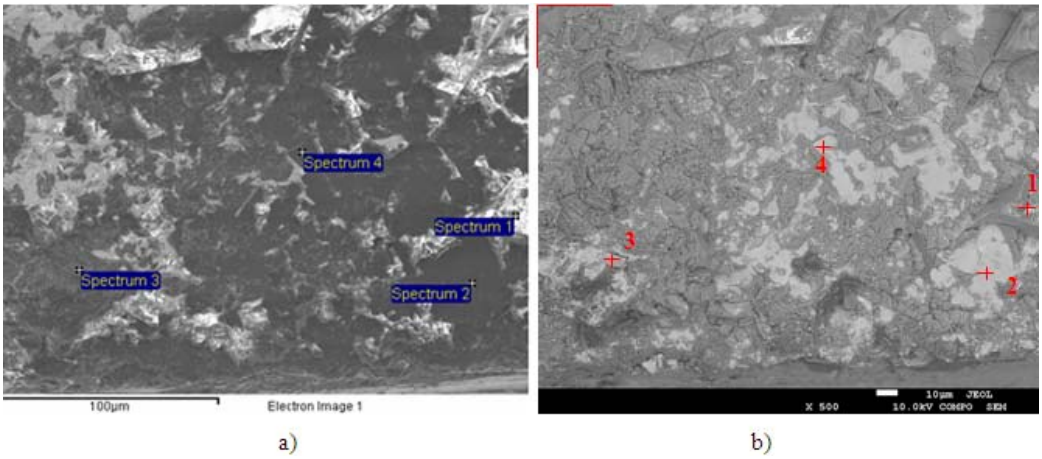

Figure 8. View of microstructure DT11T from reverse side (x500): a) in secondary electrons; b) in back-scattered electrons.

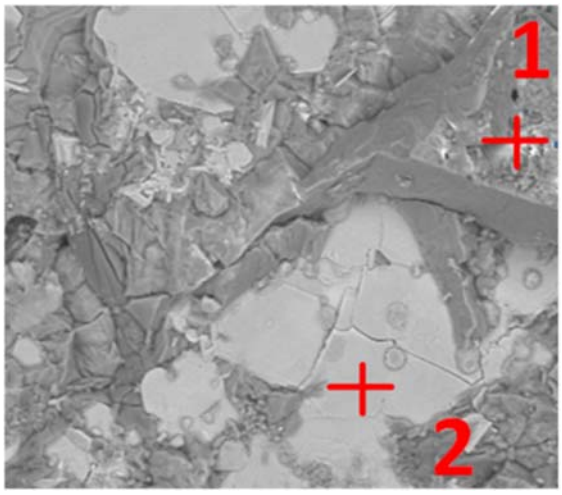

Figure 9. Enlarged field at the area of points 1 and 2.

In order to illustrate the mentioned above, we enlarged one of the field of the segment under examination (Figure 9). In fact, this is the first time when we visually observe the boride-titanium buildup – fragment of wettable coating (field with point 2) not in profile, but fullface.

According to the results of EDS-mapping (Figure 10) can be clearly and easy observe the complete coincidence of the fields Ti and B, as well as full coincidence of the fields Na and F in antiphase to the fields Ti and B. This indicates the presence of titanium borides and traces of electrolyte on the surface of carbon particles.

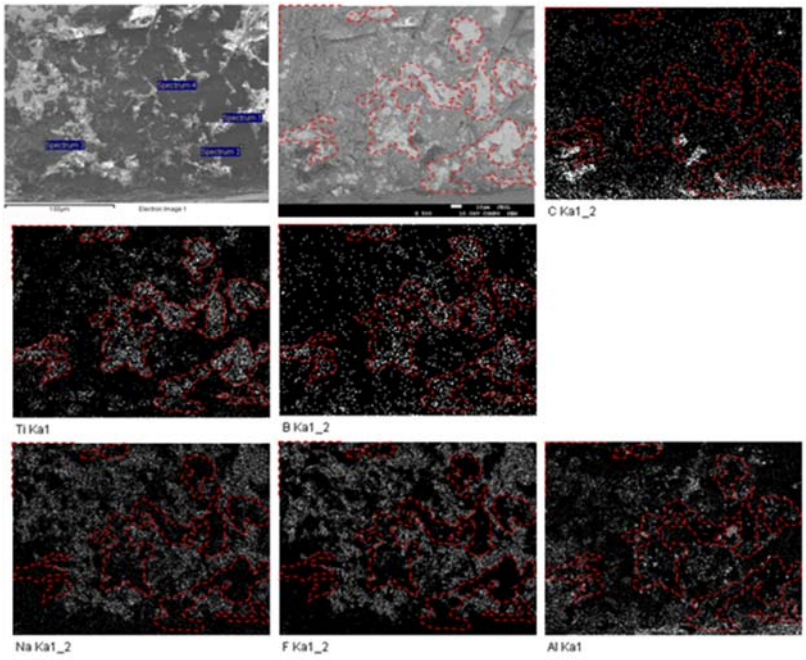

Figure 10. EDS-mapping of the DT11T specimen.

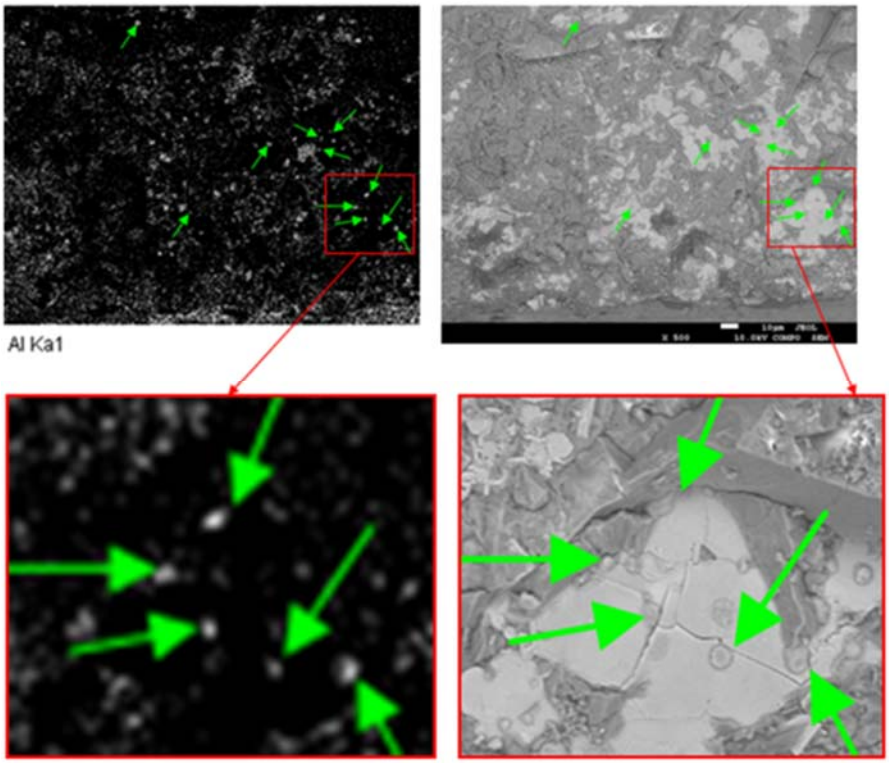

Figure 11. Microstructure of the segment DT11T. Highlighted fields.

What stands out on the aluminium map is bright nodal points; they being concentrated in the field of titanium diborides. On photo 11 is clearly visible that nodal points on the aluminium map correspond to the 2 μm circular buildups. We suppose that these nodular buildups belong to the aluminium layer, situated below, that has penetrated into 2 μm pores of boride-titanium coating and was stopped by carbon surface of the cathode.

The good adhesion of aluminium to the surface of carbon specimen DT14 could be confirmed by observations of successive destruction of the specimen, cut out from the central part of cathode (Figure 12). The visible destruction, caused by atmospheric moisture started on 10-11th day. The notable in the phenomenon under consideration consists in the place and direction of crack propagation – following the body of specimen, on the front of impregnation with electrolyte melt. There was no any separation of aluminium from carbon surface at all there; which could be explained only by its ideal adhesion to the carbon and by absence of electrolyte layer between Al and C.

As in expectation of analysis the carbon specimen collapsed this was not the interface of aluminium and carbon in the cross-section that was subjected to the SEM-EDS analysis but the segments of completely intact surface of this interface from the reverse, earlier inaccessible side were.

On closer examination of the picture in compositional contrast (Figure 13), the field of dark color represents a textured mixture of residual carbon particles that are over the adjacent to the light field that is located below (between the layer of aluminium and carbon surface). As EDS-analysis shown, this light field represents the layer of borides, generated during the 42-hour experiment.

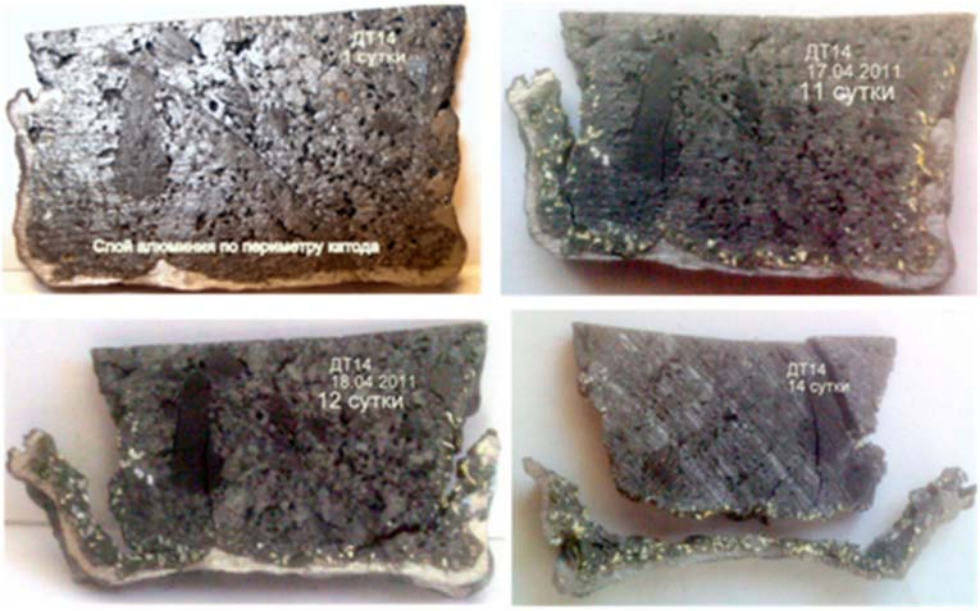

Figure 12. Successive destruction of the DT14 specimen.

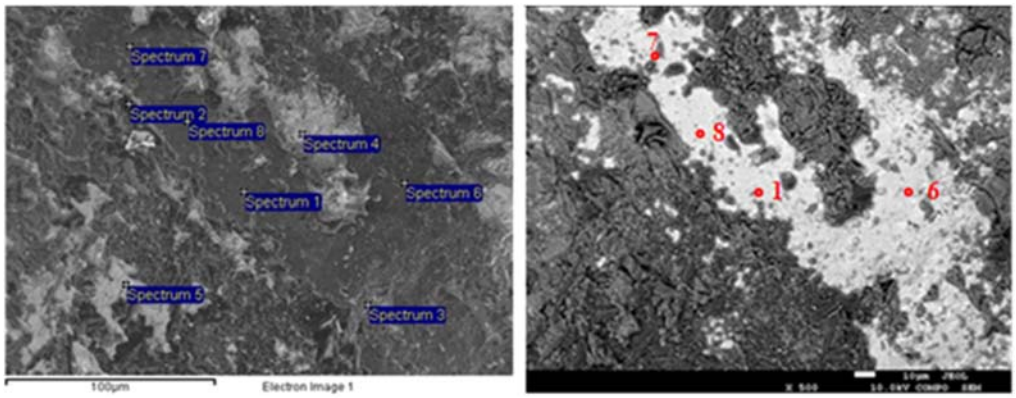

a) b)

Figure 13. Microstructure of the DT14 specimen (x500): a) in secondary electrons; b) in back-scattered electrons.

In points 1, 6, 7 and 8 the ratio of boron to titanium gives ground to represent compounds $TiB_{1.94}$, $TiB_{3.2}$, $TiB_{1.9}$ and $TiB_{2.3}$ accordingly. Visually in Figure 14 is easy to note the complete and concentrated coincidence of boron and titanium fields. Thus, it seems clear that the well observed wetting of cathode surface with aluminium is substantiated by wettable coating TiB_2 formed.

As well as in previous case (segment of specimen DT11T) the bright nodal points pay attention to themselves in the field of aluminium, but they are mostly concentrated in the field of titanium borides. In Figure 15 is clearly seen that nodular points on the aluminium map correspond to 2 µm buildups of different shape. These nodular points are missing on the map of oxygen; therefore, they belong exclusively to the aluminium layer that penetrated into 2 µm pores of boride-titanium coating and is now at the bottom.

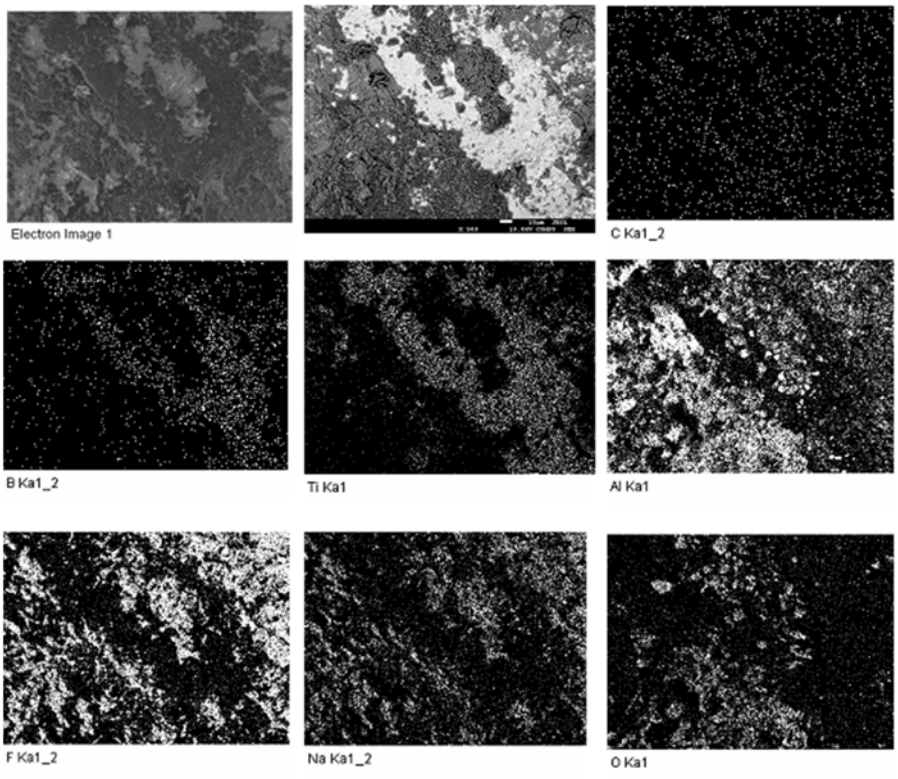

Figure 14. EDS-mapping of the DT14 specimen.

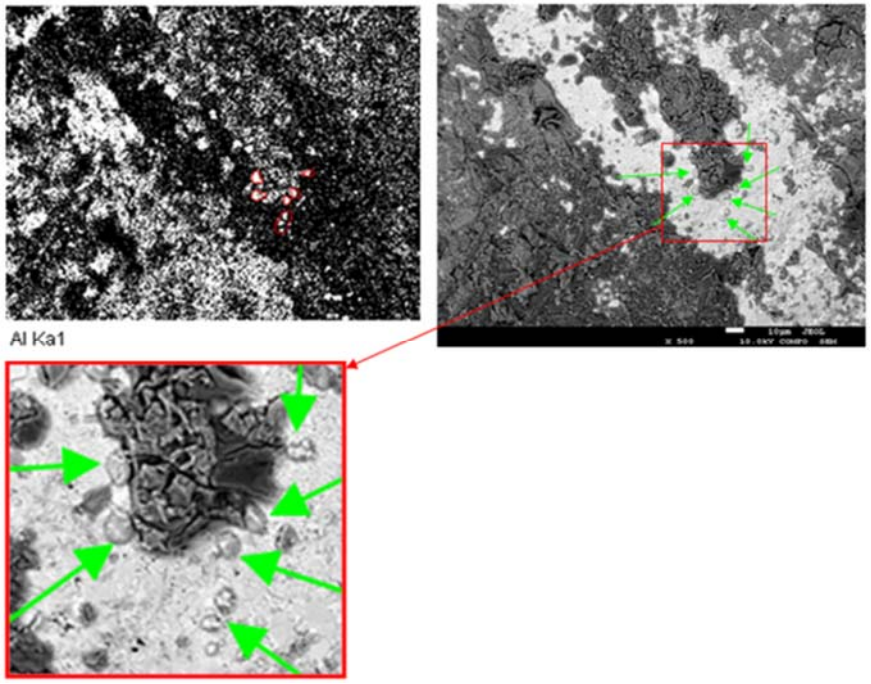

Figure 15. Microstructure of the DT14 specimen. Highlighted field.

MECHANISM OF WETTABLE COATING FORMATION

Data obtained allow assuming that the transfer of titanium in liquid phase takes place in parallel with the solid-phase diffusion. During the electrolysis the titanium-bearing buildups of Ti, Ti_xO_y and $Ti_xO_yC_z$ in the cathode body are subjected to the impregnation and dissolution with filtrate of electrolyte. As a result the conditions appear for the quick and efficient distribution of titanium in its atomic and ionic states, in elementary form and in form of oxides. Thus, titanium would be evenly distributed in any form within the carbon body to the depth of cathode impregnation with electrolyte if the exposure time would be rather sufficient.

When arranging the opposite flow of boron and aluminium solutions in their elementary form or in form of compounds the conditions would be created for direct interaction of main components of the wettable coating and preliminary stage of boron and titanium reduction from oxides by dissolved aluminum. These active forms would finally interact to the generation of titanium borides $Ti+2B = TiB_2$.

Graphically, discussing the mechanism can be represented by the scheme 16.

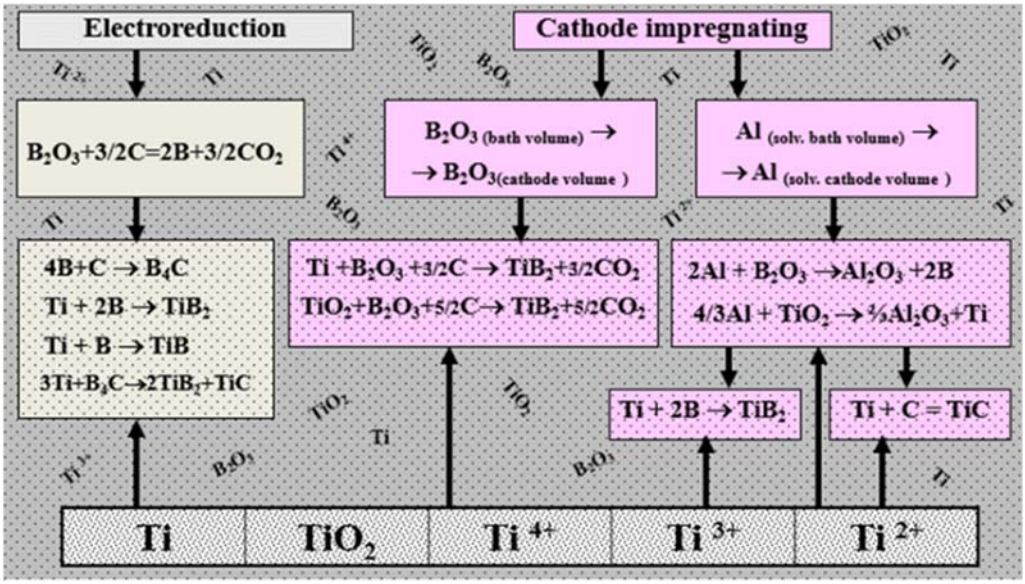

Figure 16. Formation mechanism of the Aluminium-Wettable Coating.

The reactions under discussion go with high heat emission. Therefore, it is quite possible that the temperature within the reaction zone would drastically increase to the initialization of endoergic reactions:

$$TiO_2 + 2C \leftrightarrows TiC + CO_2$$
$$TiO_2 + 2C \leftrightarrows TiC + 2CO$$

The further development of solid phase processes could create conditions for the formation of complex compounds in the system Ti–B–C, e.g., $xTiB_2 + yTiC \rightarrow xTiB_2{\cdot}yTiC$.

So, at the electrochemical borating of the cathode to the depth of electrolyte penetration into the carbon-titanium array the aluminium-wettable layer of titanium borides Ti_xB_y and carbo-borides $Ti_xB_yC_z$ would be generated. Conditionally, the formation of wetted surface through the stage of growth of non-stoichiometric compounds in the system titanium-boron-carbon, then TiB and eventually TiB_2 is shown in the Figure 17.

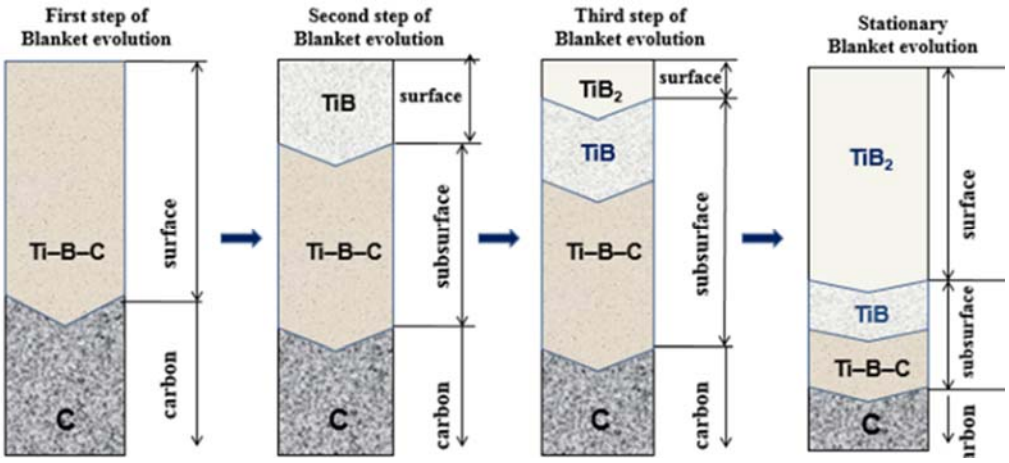

Figure 17. Boronizing of a carbon-titanium surface.

As the opposite flows of boron and titanium are determined by their transfer in liquid phase, i.e., these transfers have a relatively high rate, the generation of these compounds occurs within the subsurface impregnated volume of the cathode without forming any laminar structure and composition.

CONCLUSION

1. In laboratory conditions the process of producing Al-wettable subsurface layer was developed and carried out by method of electrochemical borating of carbon-titanium cathode in cryolite melts.

Visual inspections of the specimen after electrolytic experiments show obvious wetting of the carbon surface with aluminium, having a good adhesion of the metal to the cathode.

2. The cause of carbon cathode wetting with aluminium was found – the presence of 100-500 μm subsurface layer of carbide-boride compounds that were synthesized during the 20-42-hour electrolytic cycle. The results of XRD and SEM-EDS analyses of cathode specimens obviously discover the presence of compounds of the system Ti-B-C, including TiB_2 and TiC.
3. The mechanism of Al-wettable Ti–B–C cathode coating formation is implemented through the successive parallel stages of opposite solid- and liquid phase flows of boron and titanium (in elementary form and in form of compounds) with their subsequent interaction in the transition and contact zone.

REFERENCES

[1] Devyatkin S. V., Kaptay G., Boutellion J., Poignet J.-C. Electrochemical synthesis of titanium diboride coatings from cryolite melts//*Molten Salts Forum. Trans Tech Publications.*- 1998.- Vols. 5-6.- P. 331-334.

[2] Kaptay G. and Devyatkin S. V., Titanium diboride coating preparation in situ in the cell by electrochemical synthesis, X Al symposium, Slovakia, 1999, 80-84.

[3] Makyta M., Danek V., Haarberg G. M., Thonstad J. Electrodeposition of titanium diboride from fused salts//*Journal of Applied Electrochemistry*.- 1996.- Vol. 26.- P. 319-324.

[4] James B. J., Welch B. J., et al. Interfacial Processes and the Performance of Cathode Linings in Aluminum Smelters.//*JOM*, №47, №2, 1995, pp. 22-25.

[5] Simakov D., Vassiliev S. et al. Electrodepozition of TiB_2 from Cryolite-Alumina Melts.//*Light Metals*, 2008, pp. 1019-1022.

[6] McClung M. et al. Plant Experience with an Experimental Titanium Diborid Cell.//*Light Metals*, 2004, pp. 399-404.

[7] Keller R. Cells Incorporating Carbon Blocks Impregnated With Boron Oxide.//*Light Metals,* 2005, pp. 793-794.

[8] Gorlanov E. S., Nikiforov S. A., Alternative technology to create wettable protective coating on the surface of the carbon bottom aluminum cell. In proc. reports of the International Conference "Aluminum of Siberia," Krasnoyarsk, 2006.

[9] Ricardo J. A. G. Optimization of TiB_2 coatings electrodeposited from halide melts.//*Master dissertation in chemistry*. – 2008, 70 p.

[10] Gorlanov E.S. and others. Development of Technology for Producing an Al-Wettable Coating on a Carbon Cathode of Aluminium Pot. Part 1 and 2. Successive Electrtrodeposition of Ti and B from Cryolite Melts//Proceedings contain the materials of the 31st International Conference ICSOBA and the 19th International Conference Aluminum of Siberia./Edited by: Peter V. Polyakov and Andrey V. Panov. - Krasnoyarsk, Russia, 4th– 6 th September 2013 – p. 634-658.

SHORT COMMUNICATIONS

Smart Nanocomposites
Volume 7, Number 1
ISSN: 1949-4823

IMPACT OF SURFACE NANO-MODIFIER ON SORPTION PROPERTIES OF ORDINARY PORTLAND CEMENT

E. A. Tutov[1,*], D. L. Goloshchapov[1], H. I. Al-Khafaji[2], A. E. Tutov[1], and O. V. Artamonova[1]

[1]Voronezh State University of Architecture and Civil Engineering, Voronezh, Russia
[2]College of Engineering, Al-Nahrain University, Baghdad, Iraq

ABSTRACT

The electro-physical parameters of cement-containing capacitive structures are studied using dielectric spectroscopy under water vapor sorption conditions. For surface treatment of ordinary Portland cement from vapor phase, we used triamon as a substance-modifier. The composition of triamon corresponds to the chemical formula $[(HOC_2H_4)_3N^+CH_3][CH_3SO_3^-]$. The frequency dependence of electro-physical parameters of the structures were studied in the frequency range 12 Hz – 100 kHz using the Goodwill *LCR*-meter (model 819). For this technique the samples was pressed with tin foil under high pressure (300 bar). The end thickness of such parallel-plate capacitor was ~1 mm. The electro-physical parameters of ordinary Portland cement weakly depend on the relative humidity of air up to ~ 75%. For p/ps > 85%, sorption of water vapor may lead to the capillary condensation in non-modified Portland cement. Increase of hydrophobic properties of an ordinary Portland cement as a result of processing in vapors of quaternary compounds of ammonium is revealed. The found effect may be useful for industrial production of dry cement mixes.

Keywords: ordinary Portland cement, quaternary ammonium compound, adsorption modification, water repellency

INTRODUCTION

Moisture content in various construction materials can undergo considerable changes, and determination of their parameters demands carrying out researches of humidity influence on their characteristics. During the hardening and formation of structure of a cement stone there is a chemical interaction of free water with cement, also water evaporation. Electro-physical methods, including various variants of impedance spectroscopy [1-3], take an

* E-mail: tutov_ea@mail.ru.

important place among experimental studying methods of water interaction with a dispersed matrix.

Control of structure on a nano-level is the key issue in elaboration of hi-tech construction composites of new generation. Application of the organic surface-active substances (surfactants) is the effective way of modifying of cement mixes influencing hydrophilic and hydrophobic characteristics of components and interphase interactions.

Despite a significant amount of investigations of a surfactant role in formation of structure and properties of cement systems of hardening, searching of effective, technological, economic and ecologically safe plasticizers is actual.

A prospective solution of this fundamental problem is use of dry cement processing in vapors of quaternary compound of ammonium (triamon) which efficiency in formation of surface properties of metals nano-powders is proved in practice [4]. Use of this nano-modifier for control of surface properties of cement systems is new.

EXPERIMENTAL

For surface treatment of ordinary Portland cement from aqueous solution and vapor phase we used triamon as a substance-modifier, which is used to impart antistatic properties to the textile and polymer materials. The composition of triamon corresponds to the chemical formula $[(HOC_2H_4)_3N^+CH_3][CH_3SO_3^-]$.

The frequency dependence of electro-physical parameters of the structures were studied in the frequency range 12–100 kHz using the Goodwill *LCR*-meter (model 819). For this technique the samples was pressed with tin foil under high pressure (300 bar). The end thickness of such parallel-plate capacitor was ~1 mm. The sample under investigation was placed into a hermetically sealed cell, in which a dryer with silica gel was used for removing water vapor. The required values of relative humidity p/p_s were set by the standard method using saturated solutions of various salts. The time of stabilization of stationary states in the sorption – desorption processes for structures was about 24h. The temperature of all measurements was 295 K.

RESULTS AND DISCUSSION

The frequency dependence of the structure capacitance is monotonic, and it increases systematically with the relative humidity of ambient air and upon a decrease in the measuring signal frequency. As it was shown for wide group of materials [5-9] earlier, dependence of electric capacitance of structures with hydrophilic dielectrics on relative humidity is determined by amount of adsorbed water and its distribution in insulator.

At low frequencies of a measuring signal, the recharge of interphase boundaries gives the significant contribution to the value of electric capacitance (Maxwell–Wagner effect). Capacitance at a high frequency is defined generally by amount of free water in insulator. Therefore, the dependence of the capacitance C of this structure on the relative humidity (p/p_s) in this case reflects qualitatively the form of the isotherm of water vapor sorption by insulator (cement).

Figures 1 and 2 represents such dependence for an ordinary Portland cement measured before and after its processing in triamon vapors. The initial parts of curves is similar the adsorption isotherm corresponding to the mono-molecular and poly-molecular layering. Cement slightly adsorbs water vapors at relative humidity up to 75% then on curve C (p/p_s) essential growth with a tendency to saturation at $p/p_s \geq 85\%$ is observed. It can reflects the capillary mechanism of condensation of water vapor in mesopores with a characteristic diameter ~ 10 nm.

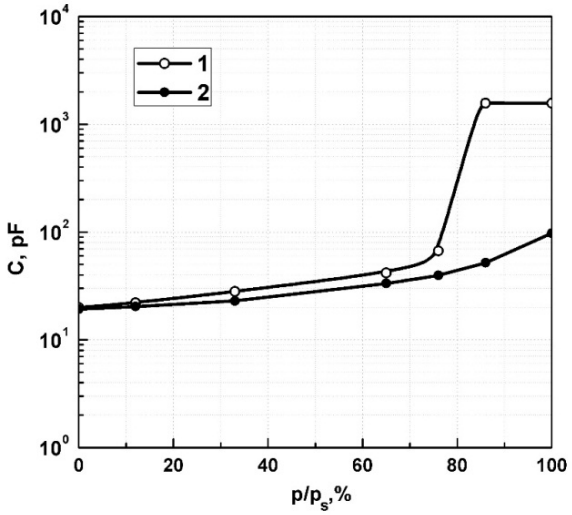

Figure 1. Dependence of the capacitance of the cement-containing structure on the relative humidity for virgin (1) and modified (2) Portland cement. Frequency of measuring is 10 kHz.

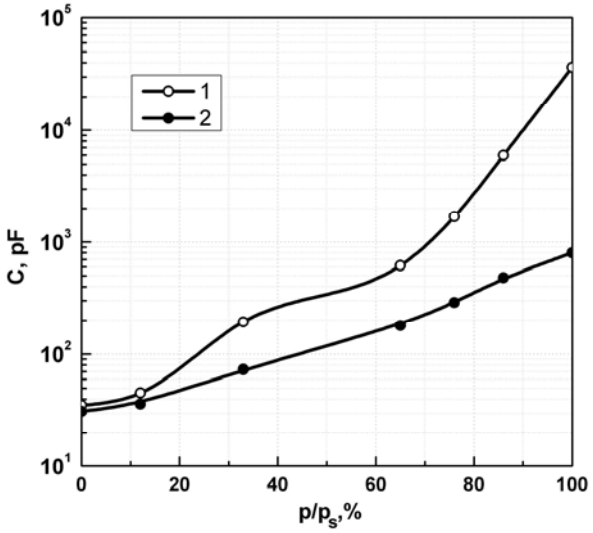

Figure 2. Dependence of the capacitance of the cement-containing structure on the relative humidity for virgin (1) and modified (2) Portland cement. Frequency of measuring is 200 Hz.

Processing of cement in triamon vapors leads to essential increase of its water repellency. Electric capacitance slightly increases to p/p_s = 85%, remaining at absolute humidity ten times less its value for non-modified cement.

CONCLUSION

Thus, the electro-physical parameters of ordinary Portland cement weakly depend on the relative humidity of air up to ~ 75%. For $p/p_s > 85\%$, sorption of water vapor may lead to the capillary condensation in non-modified Portland cement. Increase of hydrophobic properties of an ordinary Portland cement as a result of processing in vapors of quaternary compounds of ammonium is revealed. The found effect may be useful for industrial production of dry cement mixes.

REFERENCES

[1] Cabeza M., Merino P., Miranda A., Novoa X. R., Sanchez I. Impedance spectroscopy study of hardened Portland cement paste. - *Cement and Concrete Research* 32 (2002) 881–891.

[2] Cruz J. M., Fita I. C., Soriano L., Paya J., Borrachero M. V. The use of electrical impedance spectroscopy for monitoring the hydration products of Portland cement mortars with high percentage of pozzolans. - *Cement and Concrete Research* 50 (2013) 51–61.

[3] Goloshchapov D. L., Lenshin A. S., Tutov E. A., Ponomarev Yu. A., Maraeva E. V. Sorption properties of composite materials based on calcium hydroxyapatite. - *Smart Nanocomposites* 4 (2013) 101-104.

[4] Syrkov A. G. Synergetic improvement of aluminum reactivity in the presence on the surface of quaternary ammonium compounds. - *Russian Journal of General Chemistry* 83 (2013) 1621-1622.

[5] Tutov E. A., Andryukov A. Yu., Bormontov E. N. Adsorption-based porosimetry using capacitance measurements. - *Semiconductors* 35 (2001) 816–820.

[6] Tutov E. A., Bormontov E. N., Kashkarov V. M., Pavlenko M. N., Domashevskaya E. P. Influence of water vapor adsorption on the C–V characteristics of heterostructures containing porous silicon. - *Technical Physics* 48 (2003) 1442–1448.

[7] Tutov E. A., Bormontov E. N., Pavlenko M. N., Netesova G. A., Tutov E. E. MIS structure with polyamide insulator under the conditions of water vapor sorption. - *Technical Physics* 50 (2005) 1048–1052.

[8] Tutov E. A. MOS structures with amorphous tungsten trioxide for capacitive humidity sensors. – *Semiconductors* 42 (2008) 1561–1563.

[9] Tutov E. A. Solid structures with bioorganic films on silicon. - *Technical Physics* 57 (2012) 765–769.

Smart Nanocomposites
Volume 7, Number 1
ISSN: 1949-4823

PROSPECTS OF CHROMOGENIC COMPOSITE COATINGS FOR SMART WINDOWS

E. A. Tutov[1,*], H. I. Al-Khafaji[2], A. V. Manannikov , and V. Yu. Kvasova[1]

[1]Voronezh State University of Architecture and Civil Engineering, Voronezh, Russia
[2]College of Engineering, Al-Nahrain University, Baghdad, Iraq

ABSTRACT

In the brief review, the state and prospects of application in an architectural glazing of energy efficient "smart" windows with chromogenic coatings are analyzed. Comparison of electro-, thermo- and photochromic effects is carried out.

Keywords: smart windows, electrocromism, photochromism, thermocromism, composite films

INTRODUCTION

The modern architectural glazing differs in increased requirements to functional and operational properties of the used materials, to their technological, economic, energy saving, optical and esthetic characteristics [1, 2]. The technologies of a glazing based on use the chromogenic materials received the name of "smart" technologies [3, 4]. More than a half of the market of smart windows makes architectural sector, automobile – on the second place. Now the technology of a dynamic daylight and solar energy control for application in architectural glazing is at an initial stage of industrial use.

RESULTS AND DISCUSSION

Chromogenic material changes the optical properties due to influence of electric current, light irradiation, variations of temperature and other factors [5, 6]. Respectively known electrochromic, photochromic and thermochromic materials [7, 8] (Table).

* E-mail: tutov_ea@mail.ru.

Table. Classification of chromogenic devices by optical properties change

Chromogenic devices	
Activated with electricity (active)	Activated without electricity (passive)
EC or electrochromic	Thermochromic
LC or liquid crystal	Photochromic
SPD or suspended particle device	Chemichromic

The electrochromic effect in organic and inorganic materials is the most studied and technologically advanced [9], however, in our opinion, has basic restrictions for use in a glazing. The electrochromic window represents in fact the display of large area. It is the multilayered structure including transparent electrodes one of which has to be an injector of electrons in a film of electrochromic material (for example, WO_3), and the second electrode has to be an injector of cations. Requirements to all film layers of structure rather high. Besides, the external source of power supply and control is necessary. All this does an electrochromic window rather expensive and reduces its competitiveness.

The UV-component of a daylight can induce emergence of the color centers in a chromogenic material (for example, the same WO_3) [10] (Figure 1).

In vanadium dioxide (VO_2) heating to 68 °C causes phase transition the semiconductor – metal at which its optical characteristics considerably change [11 - 13].

Use of composite coatings on the basis of any transparent film matrix filled with (thermo-) photochromic material will allow to make, in our opinion, technology of smart windows even more flexible and available [14-20]. Deposition a chromogenic layer on an internal surface of the glass integrated into a traditional double-glazed window gives additional opportunity to a chemical sensitization of thermo- or photochromic material by addition of gases – donors of electrons (for example, alcohol vapors) in an air between glasses. It is known, that a photochromic effect in WO_3, and phase transition in VO_2 [21, 22] are sensitive to such influences (Figure 2).

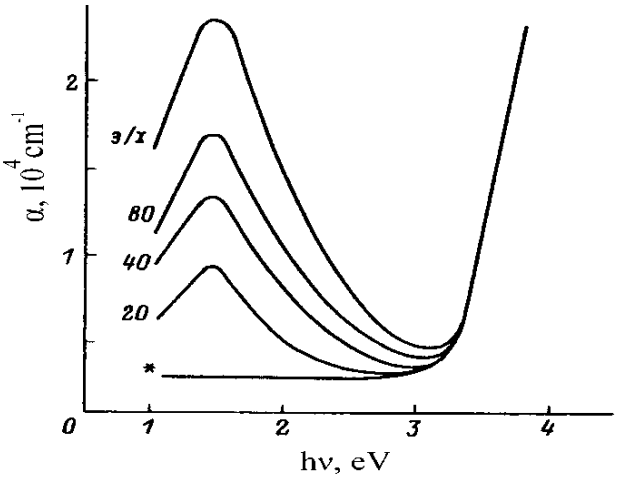

Figure 1. Optical absorption for electro - and photochromic a-WO_3 films (according to work [10]). Figures at curves – time of UF-irradiation, min. The asterisk noted a curve for an initial film, the top curve for an electrochromic film.

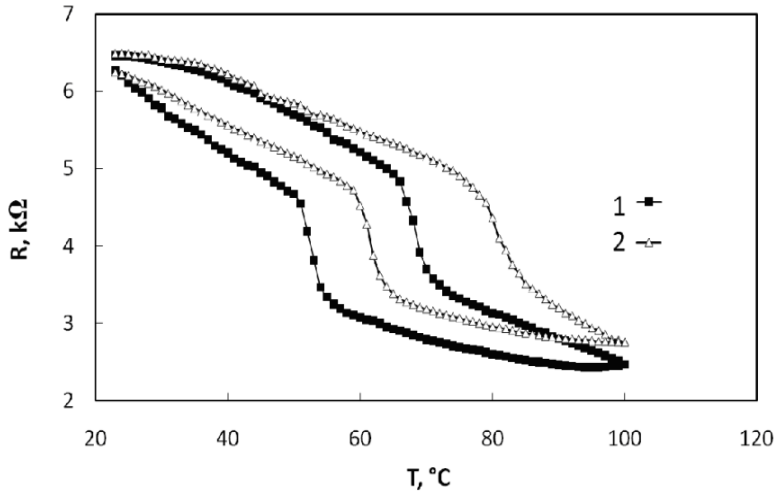

Figure 2. Dependence of the resistance of the Ag/VO_x/Si structure on the temperature (1) in the air flow and (2) in the flow of air saturated with ethanol vapor during heating (right-hand branch of the loop) and cooling (left-hand branch of the loop).

CONCLUSION

Realization of thermo- and photochromic effects in inorganic and organic (including polymeric) materials does not need a source of electrical power and fabrication of a high-uniform films. Use of these effects for creation of glasses with an adaptive light transmittance seems to be economically and technologically attractive to wide application in architectural glazing.

REFERENCES

[1] Baetens R., Jelle B. P., Gustavsen A. Properties, requirements and possibilities of smart windows for dynamic daylight and solar energy control in buildings: A state-of-the-art review. - *Solar Energy Materials & Solar Cells* 94 (2010) 87–105.

[2] Kima J. T., Todorovic M.S. Tuning control of buildings glazing's transmittance dependence on the solar radiation wavelength to optimize daylighting and building's energy efficiency. - *Energy and Buildings* 63 (2013) 108–118.

[3] Kamalisarvestani M., Saidur R., Mekhilef S., Javadi F.S. Performance, materials and coating technologies of the thermochromic thin films on smart windows. - *Renewable and Sustainable Energy Reviews*, 26 (2013) 353–364.

[4] Niklasson G. A., Granqvist C. G. Electrochromics for smart windows: thin films of tungsten oxide and nickel oxide, and devices based on these. - *J. Mater. Chem*., 17 (2007) 127–156.

[5] Lampert C. M. Chromogenic smart materials. – *Materials today* (2004)28-35.

[6] Granqvist C.G., Green S., Niklasson G. A., Mlyuka N. R., von Kraemer S., Georen P. Advances in chromogenic materials and devices. - *Thin Solid Films* 518 (2010) 3046–3053.

[7] Granqvist C. G., Lansaker P. C., Mlyuka N. R., Niklasson G. A., Avendano E. Progress in chromogenics: New results for electrochromic and thermochromic materials and devices. - *Solar Energy Materials & Solar Cells* 93 (2009) 2032–2039.

[8] Wilkinson M., Kafizas A., Bawaked S. M., Obaid A. Y., Al-Thabaiti S. A., Basahel S. N., Carmalt C. J., Parkin I. P. Combinatorial atmospheric pressure chemical vapor deposition of graded TiO_2 - VO_2 mixed-phase composites and their dual functional property as self-cleaning and photochromic window coatings. - *ACS Comb. Sci*. 15 (2013) 309-319.

[9] Mortimer R. J. Electrochromic materials. *Annu. Rev. Mater. Res*. 41 (2011) 241-268.

[10] Tutov E. A., Kukuev V. I., Baev A.A., Bormontov E.N., Domashevskaya E. P. Electronic processes related to electrochromism and photochromism in a-WO_3/Si heterostructures. - Technical Physics. *The Russian Journal of Applied Physics* 40 (1995) 697-700.

[11] Blackman C. S., Piccirillo C., Binions R., Parkin I. P. Atmospheric pressure chemical vapour deposition of thermochromic tungsten doped vanadium dioxide thin films for use in architectural glazing. - *Thin Solid Films* 517 (2009) 4565.

[12] Zhou M., Bao J., Tao M., Zhu R., Lin Y., Zhang X., Xie Y. Periodic porous thermochromic VO_2(M) films with enhanced visible transmittance. - *Chem. Commun*. 49 (2013) 6021-6023.

[13] Warwick M., Binions R. Advances in thermochromic vanadium dioxide films. – *J. of Materials Chemistry A*. 2 (2014) 3275-3292.

[14] Seeboth A, Krivanek J., Lotzsch D., Patzak A. Chromogenic polymer gels for reversible transparency and color control with temperature at a constant volume. – *Polymers for Advanced Technologies* 13 (2002) 507-512.

[15] Seeboth A., Ruhmann R., Muhling O. Thermotropic and thermochromic polymer based materials for adaptive solar control. – *Materials* 3 (2010) 5143-5168.

[16] Lee E. S., Pang X., Hoffmann S., Goudey H., Thanachareonkit A. An empirical study of a full-scale polymer thermochromic window and it simplications on material science development objectives. - *Solar Energy Materials & Solar Cells* 16 (2013) 14–26.

[17] He T., Yao J. Photochromism in composite and hybrid materials based on transition-metal oxides and polyoxometalates. - *Progress in Materials Science* 51 (2006) 810–879.

[18] Pardo R., Zayat M., Levy D. Photochromic organic–inorganic hybrid materials. - *Chem. Soc. Rev*. 40 (2011) 672–687.

[19] Gao Y., Luo H., Zhang Z., Kang L., Chen Z., Du J., Kanehira M., Cao C. Nanoceramic VO_2 thermochromic smart glass: A review on progress in solution processing. - *Nano Energy* 1 (2012) 221–246.

[20] Zhang J., Zou Q., Tian H. Photochromic materials: more than meets the eye. - *Adv. Mater.* (2012) 1-22.

[21] Tutov E. A., Zlomanov V. P. Effect of chemisorption of donor and acceptor gases on the semiconductor–metal phase transition in vanadium dioxide films. - *Physics of the Solid State* 55 (2013) 2351–2354.

[22] Tutov E. A., Kryukov P. I., Zlomanov V. P. Chemisorptions field effect in nanocrystalline films of vanadium oxide. - *Smart Nanocomposites* 4 (2013) 75-77.